Revised manuscript with changes marked
Click here to view linked References

# 2D bio-based nanomaterial as a green route to amplify the formation of hydrate phases of cement composites: Atomistic simulations and analytical characterization

*Yin Chi,*[a,b*] *Bo Huang,*[b] *Mohamed Saafi,*[b*], *Nigel Fullwood*[c], *Colin Lambert,*[d] *Eric Whale,*[e] *David Hepworth,*[e] *Jianqiao Ye* [b]

[a] School of Civil Engineering, Wuhan University, Wuhan 430072, China
[b] Department of Engineering, Lancaster University, Lancashire, LA1 4YW, UK
[c] Biomedical and Life Sciences, Lancaster University, Lancashire, LA1 4YW, UK
[d] Department of Physics, Lancaster University, Lancashire, LA1 4YB, UK
[e] CelluComp Ltd, Fife, KY3 9DW, UK

**Abstract**

Ordinary Portland cement (OPC) is the binding element in concrete materials and, $CO_2$ emissions associated with its manufacturing and use is about 8% of the world's $CO_2$ emissions. The engineering properties of hardened concrete depend on the amount of the hydrate phases in OPC. If the growth of the hydrate phases could be increased, the performance of concrete would be significantly improved, and the consumption of OPC will be decreased, and its environmental footprint will be reduced. In this paper, we present a new green approach for controlling the growth of the hydrate phases in OPC using bio flakes composed of staked carrot-based two-dimensional (2D) nanosheets (CNSs) synthesized from carrot waste. Density-functional theory and reactive molecular dynamics (DFT-MD) simulations were carried out in conjunction with analytical characterization to examine the interfacial interaction between CNS with tricalcium silicate $Ca_3SiO_5$ ($C_3S$), the main constituent of OPC and understand how they influence the growth of the hydrate phases in OPC. The DFT-MD simulations results show the 2D CNS dissolves due to its interfacial interaction with the highly reactive $C_3S$, leading to a series of fast proton exchange in $C_3S$. This in return accelerates the dissolution rate of $C_3S$ thereby amplifying the growth of the hydrate phases. The DFT-MD simulations also show that the dissolution of the 2D CNS creates new several organic compounds that enhance the mobility and dynamics of protons that further amplify the dissolution rate of $C_3S$. The analytical results from scanning electron microscope (SEM), X-ray diffraction (XRD), transmission electron microscopy (TEM), and thermography analysis (TGA) and differential scanning calorimetry (DSC) show a significant growth of the hydrate products in OPC due to interfacial dissolution of $C_3S$ and some CNS thus, confirming the DFT-MD results. This work demonstrates that the growth of the hydrate products in OPC can be amplified by the addition of green and renewable 2D bio-based nanomaterials. This green approach provides a base for the design and development of low-carbon cementitious materials.

**Keywords:** Density Function Theory (DFT); Reactive Molecular Dynamics Simulation; Cement Hydration; Tricalcium Silicate; Carrot Nanosheet.

*Corresponding authors.
Email addresses: yin.chi@whu.edu.cn (Y. Chi), m.saafi@lancaster.ac.uk (M. Saafi)

## 1. Introduction

Concrete is the most consumed man-made material on the planet. It is used to construct and repair the built environment including buildings, transportation systems and energy infrastructure. Concrete is a heterogeneous composite material, consisting of a mixture of mineral aggregates, water and ordinary Portland cement (OPC), and its performance strongly depends on the amount the products of OPC particles[1]. The amount of the hydrate products of OPC is generally expressed as the amount of cement particles that have hydrated compared to the initial amount of unhydrated cement particles[2], this is usually called the degree of hydration (DOH). The more hydrated cement particles, the higher the amount of the hydrate phases, thus better engineering properties and durability of concrete due to the increased amount of calcium silicate hydration phases (C-S-H), which are the main binding material of concrete.

However, current concrete manufacturing techniques can only achieve the production of concretes with small quantities of hydrate products due to lack of control of the hydration mechanism of OPC which takes place at the nanoscale[3]. As a result, large amounts of OPC are routinely used to produce high performance structural concretes in order to offset the deficiency in the hydration of the cement particles. If the amount of the hydrate products of OPC could be improved, the volume of OPC needed for a given structure would be reduced and the release of $CO_2$ resulting from its production into the atmosphere would be decreased. Cement production accounts for about 8% of global $CO_2$ emissions, a main cause of climate change [4].

One popular approach to improve the engineering properties of concrete is the use of a wide range of nanoparticles including nano silica[5], nano alumina[6], nano titanium oxide[7], nano kaolin[8], nano clay[9] and nano calcium carbonate[10] to increase the amount of the hydrate phases through interfacial chemical reactions in the cement environment[11]. An alternative solution to the production of low carbon-foot print cement is to replace the Portland clinker with supplementary

cementitious materials (SCMs) [12]. Studies have shown that replacement of Portland clinker with SCM can reduce $CO_2$ emissions of up to 40% without significant changes in mechanical properties and durability [13]. Another way to enhance the engineering properties of concrete of is strengthening the hydrate products of OPC with non-reactive carbonaceous nano particles such as carbon nanotubes[14], carbon nanofibers[15], graphene[16,17] and graphene oxide[18–20]. Unfortunately, the large-scale applications of these nanoparticles in building materials have been hampered by the intrinsic difficulty to disperse them in concrete, costs, and potential health and safety effects[21]. As such, there is a need to develop a new generation of high-performance, renewable and sustainable nanomaterials as an alternative to the environmentally harmful existing nanoparticles for creating high performance cementitious composites with lower carbon-foot print.

Recently, we successfully synthesized highly hydrophilic flakes composed of stacked carrot-based two-dimensional (2D) nanosheets (CNSs) produced from carrot waste streams for the development of low-carbon footprint high-performance cementitious composites. Through our preliminary study of the effect of CNS on the performance of cementitious composites, we discovered that: 1) the growth of the hydrate phases of OPC was significantly increased, 2) the CNS layers of bio-flakes in the vicinity of the OPC particles were dissolved and 3) the CNS layers of the bio-flakes distant from the OPC particles were remained intact and were embedded in the highly defective C-S-H gel, forming C-S-H/CNS hybrid composites. Our atomistic simulations showed that one single CNS layer effectively healed this highly defective C-S-H, resulting in high strength and stiffness cementitious composites[22]. The one single layer CNS showed high affinity to C-S-H due to the interfacial Ca-O coordination and H-bond interaction. The functional groups on the surface of the CNS layer cross-linked the neighboring silicate calcium layers and inhibited the water dynamics at the silicate nanochannel, thereby significantly improved the interfacial properties of the C-S-H/CNS hybrid structure[22].

However, the origin of the enhanced growth of the hydrate phases and the dissolution of the CNS layers in the vicinity of the OPC particles during hydration are still not clear. We hypothesize that these two phenomena are the result of the interaction of the CNSs with the OPC particles during hydration. Understanding how the molecular interactions between the CNS and the main calcium silicate phase (tricalcium silicate, $C_3S$) of OPC affect the growth hydration mechanisms of hydrate phases is critical to the design and the development of these novel low-carbon and high-performance

cementitious composites.

Therefore, the aim of this paper is to study the interfacial interaction between CNS and $C_3S$ during hydration using density functional-theory calculations and reactive force field molecular dynamics simulations to gain fundamental understanding of their effects on the growth of the hydrate phases of OPC and uncover the origin of the CNS dissolution. Analytical characterization was also carried out to further ascertain the mechanisms underpinning the growth of the crystal hydrates of OPC and support the key findings of the simulations.

## 2. Material and methods

### 2.1 Preparation of carrot-based cellulose nanosheets (CNSs)

Figure 1 shows the step-by step process employed to produce the CNS material. The CNS material was fabricated by our industrial partner Cellucomp Ltd. The CNS suspension was derived from carrot pulp waste stream according to the USA Patent[23]. In this manufacturing process (see Fig.1), the carrot pulp waste was first diluted with water to form a mixture with 0.1% to 10% solid content by weight. A sodium hydroxide solution (0.5M) was then added into the mixture to raise its pH to 14. This is to extract a considerable portion of hemicellulose and pectin. Subsequently, the mixture was heated to 90°C for 5 hours followed by 1 hour stirring with a speed of 11 m/s. After heating, the mixture went through a homogenization process for 5 minutes with an agitator blade rotating at a speed of 30 m/s to separate the cells from the mixture along the line of the middle lamella. The separated cells were then broken into nano platelets with dimensions of 50 $\mu m$ in width, 50 $\mu m$ in length and 25 *nm* in thickness. A commercially available dispersant Span 20 (Croda International PLC, UK) was then added into the solution to reduce the aggregation of CNS particles. The final product is a stable suspension contains 4% CNS solids and 96% water with a chemical stoichiometry of $C_{12}H_{24}O_{10}$ for a disaccharide unit. As shown, the CNS exhibits morphology somewhat similar to graphene in terms wrinkles and folding[24]. The CNSs are highly hydrophilic making them dispersible in cement pastes and have a crystallinity index of 70%[23]. Based the centrifugation method for the cellulose nanocrystals with cement paste introduced by Cao et al.(2016)[25], the CNS cementitious composites showed that less than 5% of the CNSs used in the centrifugation experiments are present in the centrifuge solution. And over 95% of the CNSs are adsorbed onto the cement particles surface, indicating that great electrostatic interaction exists between the CNSs and the cement particles.

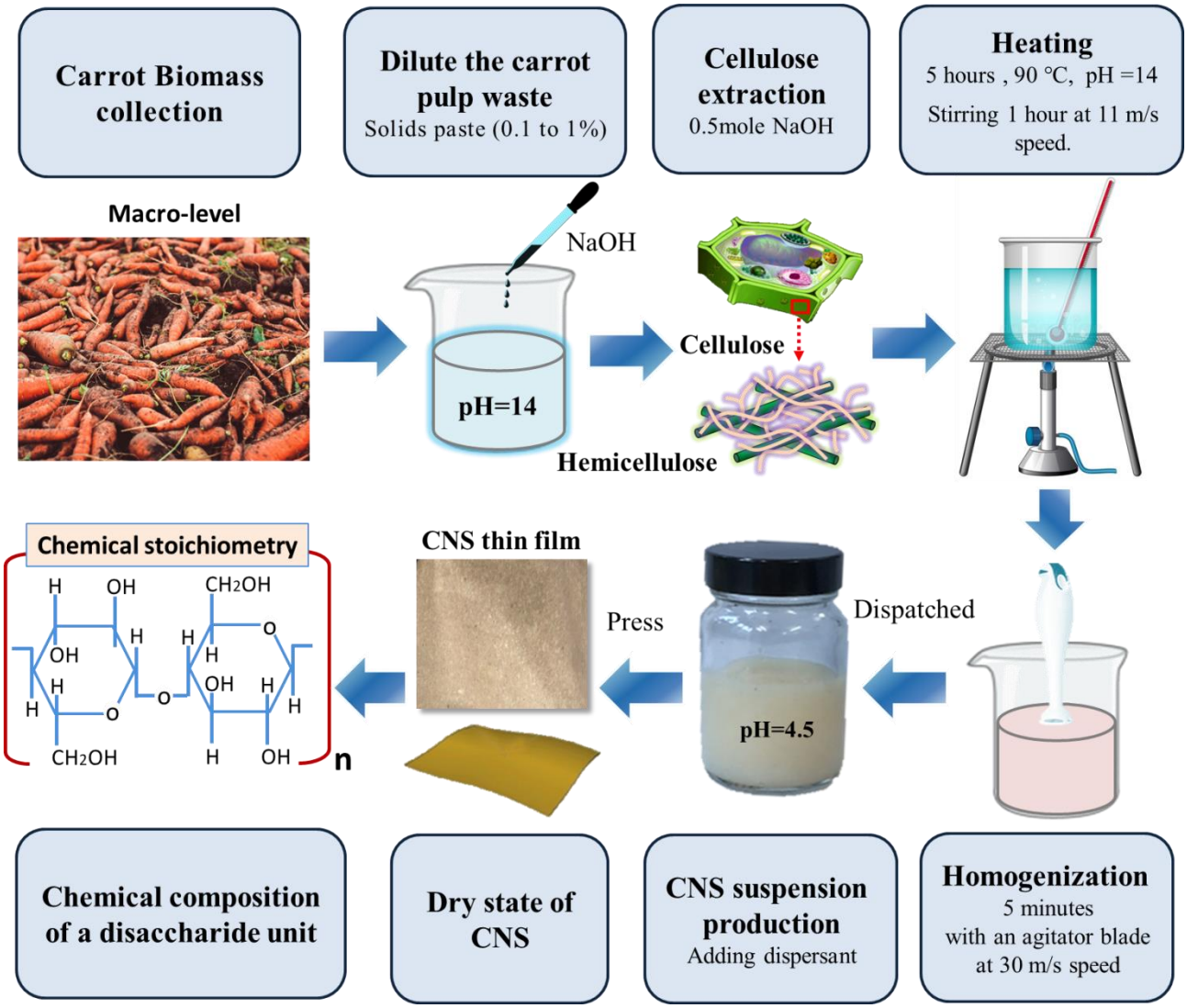


**Fig.1** Fabrication process and microstructure images of CNS

## 2.2. Computational details

*2.2.1 Tricalcium silicate ($C_3S$) and CNS crystal structures*

Alite, the impure form of tricalcium silicate Ca3SiO5 ($C_3S$), is the main phase in OPC and is responsible for setting and strength development of cementitious composites[26,27]. Thus, we examine the chemical interfacial interaction between $C_3S$ and CNS. A monoclinic superstructure of M3 polymorph (MIII-$Ca_3SiO_5$) or (MIII-$C_3S$) is used in this study, which is considered to be the most abundant form in industrial clinkers [28]. The unit cell of MIII-$C_3S$ proposed by Mumme [29] was used as the starting input for the geometry optimization using DFT. As shown in Fig. 2a, the lattice parameters of the $C_3S$ unite cell are: $a$ = 12.235 Å, $b$ = 7.073 Å, $c$ = 9.298 Å, and $\beta$ = 116.931° (space group *Cm*).

The crystalline structure of CNS is composed of four basic allomorphs, including cellulose I, II, III

and IV, where the native cellulose I is the mostly observed allomorph[30]. In addition, two polymorphic cellulose Iα and Iβ structures coexist in the cellulose I with various proportions derived from different sources. The Iα phase is metastable and can be converted into Iβ by hydrothermal treatment or high-temperature treatment in organic solvents[31]. In this paper, the initial structures of Iα and Iβ crystals of CNS are taken from X-ray and neutron diffraction experiments (XRD)[32,33]. The cellulose Iα phase has a triclinic crystallographic structure containing 1 repeatable disaccharide unit that is composed of two anhydroglucose rings. Each saccharide monomer has a stoichiometry of $C_6H_{10}O_5$ and is connected with each other by a so-called 1-4-glucosidic linkage (C1-O4-C4).

Figure 2b shows the measured unit-cell parameters of the Iα polymorph. The unit-cell parameters of Iα polymorph are $a$=6.717 Å, $b$=5.962 Å, $c$=10.400 Å, $\alpha$=118.08º, $\beta$=114.80 º, and $\gamma$=80.375 º (space group $P_1$). The cellulose Iβ phase has a monoclinic crystallographic structure containing two parallel disaccharide units its measured unit-cell parameters are $a$=7.784 Å, $b$=8.201 Å, $c$=10.38 Å, and $\gamma$=96.55 º (space group $P2_1$) (see Fig.2c). The above crystal structures are used to perform the DFT calculations.

It is worth mentioning that the CNSs could contact the cement particles on multiple sides. However, this multi-surface interaction between the CNSs and the cement particles is generally observed at a larger scale (micro/meso scale). The MD simulation for multi-surface interaction could be very challenging and can be achieved by using a coarse-grain based method. In the present study, the CNS was placed on one side of the nanopore in the silicate tetrahedral model with the objective of revealing the hydration mechanism in the cementitious composites.

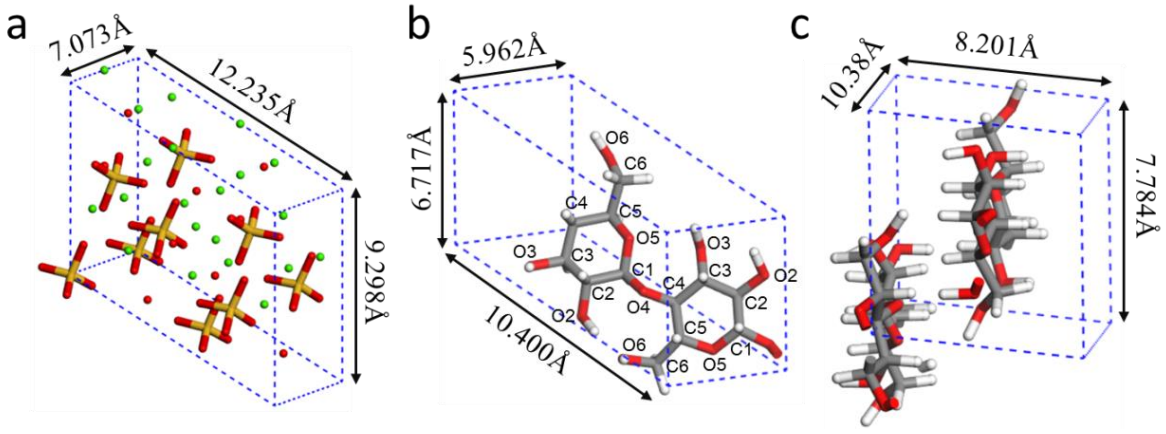


**Fig.2** Crystal primitive cell: (a) MIII-$Ca_3SiO_5$. (b) CNS Iα phase. (c) CNS Iβ phase.

*2.2.2 $C_3S$/CNS molecular model for interfacial interaction analysis during hydration*

In order to understand the effect of CNS chains on the surface hydration of $C_3S$ and probe the molecular interaction at the $C_3S$/CNS interface through molecular dynamics simulations (MD), the original monoclinic crystal structure of $C_3S$ is converted to an orthorhombic structure, developed by Heinz[34] (see Fig. 3a). As shown in Fig.3b, a $C_3S$ supercell containing 2×4×1 crystallographic unit cell is created with lattice dimensions $a$ =24.369 Å, $b$ =28.139 Å, $c$ =25.275 Å, $\alpha=\beta=\gamma=90^o$. The cleavage of the supercell structure is then made in the [0 4 0] direction to generate the $C_3S$ substrate surface. In addition, a vacuum space with a thickness of 5*nm* is built along the *b* direction to host the water molecules needed for hydration (see Fig.3b). The water molecules are packed and randomly distributed within the vacuum space (see Fig.3c). The number of water molecules satisfies the density of bulk aqueous solution of ≈1g/cm$^3$ under ambient conditions. Since simulating multiple layered CNS needs to build a much larger MD system to achieve computational convergence, which can be very time-consuming. Therefore, we use a single layered CNS in the model. A monolayer CNS containing two chains with a degree of polymerization (DOP) of 4 is placed 5Å above the cleaved $C_3S$ slab surface. The constructed $C_3S$/CNS nanocomposite molecular model is shown in Fig.3d. The final lattice dimensions are $a$ =24.369 Å, $b$ =71.00 Å, $c$ =25.275 Å, $\alpha=\beta=\gamma=90^o$, containing 1030 water molecules and 4320 atoms in total.

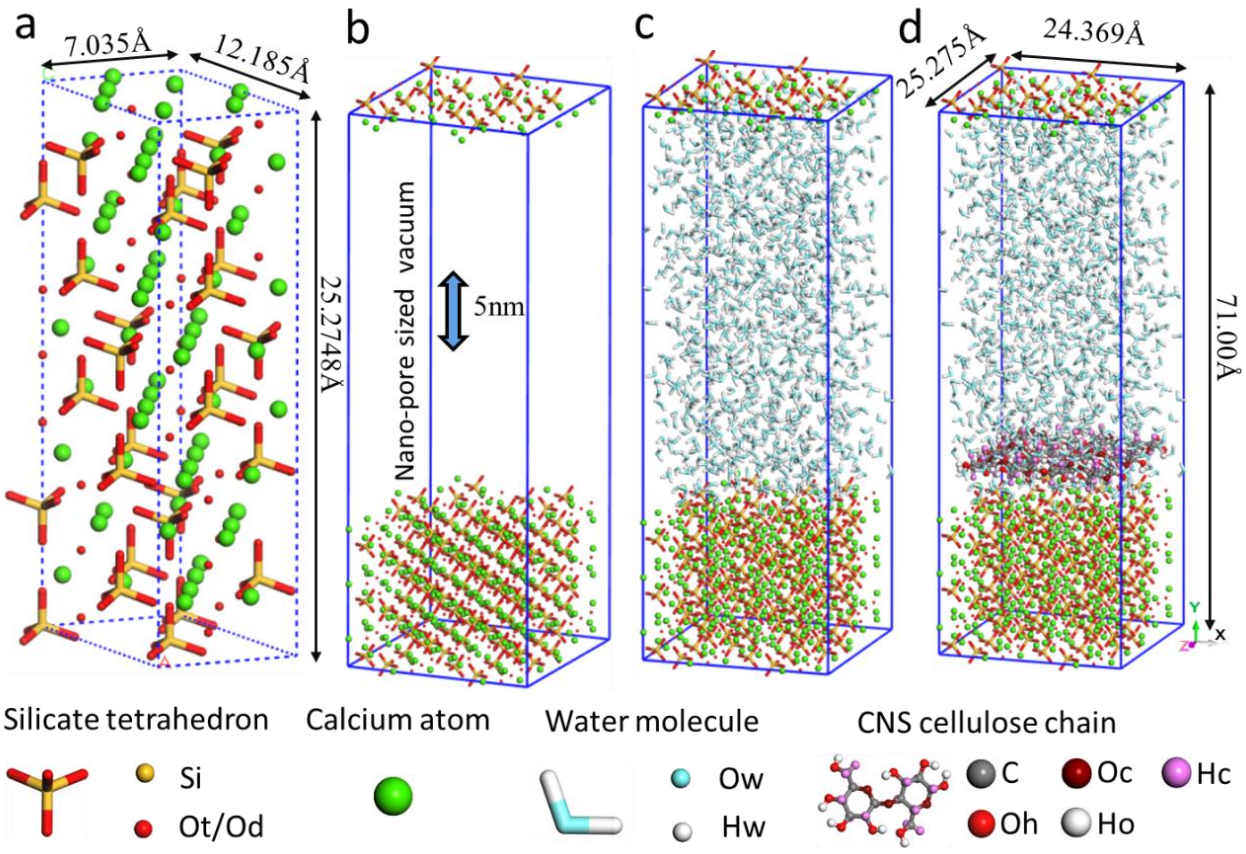

**Fig.3** Construction of interfacial hydration molecular system： (a) transformed orthorhombic $C_3S$ crystal. (b) $C_3S$ supercell with cleaved vacuum space. (c) $C_3S$ water system with randomly packed water molecules. (d) $C_3S$/CNS nanocomposite system with CNS chains.

*2.2.3 DFT calculations*

The density functional theory (DFT) calculations are performed to obtain the geometry-optimized crystal structure and the electronic properties of both the CNS and the $C_3S$ unit cells using the DMol$^3$ package[35]. The exchange and the correlation potential is treated by the generalized gradient approximation (GGA) with the Perdew-Burke-Ernzerhof (PBE) functional[36]. The Van del Waals force for the CNS cellulose hydrogen bonded system is described by the Grimme's DFT dispersion correction approach. The all-electrons method is used for the core electrons treatment. The Brillouin zone of the primitive cell models are sampled with Monkhorst-Pack *k*-point grids of 6×7×4 for the cellulose Iα phase, 6×5×4 for the cellulose Iβ phase and 3×5×4 for the $C_3S$. A double numerical plus polarization (DNP) basis with a global orbital of 5.5 Å is set as a cut-off. This orbital cut-off is found to be enough to achieve convergence with low total energy. The threshold for the self-consistent field (SCF) density tolerance is specified as $10^{-6}$ eV, and direct inversion in an iterative subspace (DIIS) is adopted to speed up the convergence. According to the Aufbau principle, the valence electron configurations include Ca $3s^2 3p^6 4s^2$, Si $3s^2 3p^2$, O $2s^2 2p^4$, C $2s^2 2p^2$, H $1s^1$. Geometric optimization convergence threshold for energy change, maximum force and maximum displacement between optimization cycles are set as $10^{-5}$ Hartree, $10^{-3}$ Hartree Å$^{-1}$ and $10^{-3}$ Å respectively.

*2.2.4 Reactive force field MD simulations*

The DFT quantum chemical computational approach is extremely expensive and is not practical to study phenomena in large and complex systems such as the chemical reactivity at the cleaved $C_3S$/CNS interface with bulk water solution. Therefore, the semi-classical potential based MD simulation is adopted as a less intensive computational alternative to cope with these complex nanocomposite systems. This allows better understanding of the long-term chemical reactivity of the silicate phases while remaining far more computationally efficient than the ab initio simulation. The MD simulations were carried out using the reactive force field (ReaxFF)[37,38] which is implemented in the LAMMPS simulation package[39]. The ReaxFF employs a bond-order formalism in conjunction with the polarizable charge descriptions to describe the interaction between different atoms. The potential energy function is summed by the following partial energy contributions:

$$E_{system} = E_{bond} + E_{over} + E_{under} + E_{angle} + E_{torsion} + E_{Vdw} + E_{Coul} \quad (1)$$

where $E_{bond}$ is the energy associated with forming bonds between atoms, $E_{over}$ and $E_{under}$ are the energies preventing the over coordination and under coordination of atoms, respectively based on the atomic valence rules, $E_{angle}$ and $E_{torsion}$ are the three-body valence angle energy and the four-body torsional angle energy. $E_{Vdw}$ and $E_{Coul}$ are the Van der Waals and Coulomb interaction, respectively, associated with the dispersive and the electrostatic contributions between all atoms.

The ReaxFF has been extensively employed to study the structural and mechanical properties of C-S-H of OPC[40–43] as well as the interfacial strengthening mechanism in C-S-H/polymer nanocomposites[44–47]. It has also been used successfully to examine dissociation of water molecules in C-S-H crystals[48–50]. In addition, the ReaxFF has the ability to capture the bond breakage/formation during the hydration process of OPC by updating bond orders, and elucidate phenomena that take place during chemical reaction of $C_3S$ with water such as dissociation of water, formation of hydroxyl groups ($OH^-$) and the diffusion of hydrogen atoms ($H^+$).

In this study, ReaxFF parameters consisting of a combination of Ca/Si-O-H and C-O-H sets from literature[17,51] were employed to examine the reactivity of $C_3S$ with the CNS chain in the presence of bulk water using the relatively large molecular system shown in Fig.3d. The simulation process is implemented in the following sequence: first, the $C_3S$ substrate and the CNS chain are frozen with fixed zero forces, the bulk water solution is then relaxed with NVT ensemble for 25 picoseconds at an ambient temperature of 300 Kelvin to allow a random diffusion of the water molecules in the nano-pore. Second, after the aqueous solution equilibrium is reached, the rigid $C_3S$ substrate and the CNS chain are unfixed and all atoms in the simulation system are then relaxed to allow the molecular structure to evolve. During relaxation, the energy minimizations are performed using a conjugate gradient method for the $C_3S$/CNS composite molecular system. This is to achieve an overall stable configuration with an energy convergence threshold of $10^{-6}$ Kcal/mole and a force tolerance cutoff of $10^{-6}$ Kcal/mole-Angstrom. The MD simulations are performed within the isothermal-isobaric (NPT) ensemble for 3 nanoseconds at 300 Kelvin temperature. The length of each time step is fixed at 0.25 femtosecond, and a built-in Noose-Hoover style themo/barostatting with a Verlet time-integration scheme is applied throughout the MD simulations. The pressure, temperature, energy and other thermodynamic information are monitored during simulation to ensure stability of the system.

The structural and dynamics information such as the atomic intensity, radial distribution function (RDF), mean squared displacement (MSD) and $OH^-$ number are analyzed to characterize the effect of CNS on the hydration of $C_3S$ resulting from the chemical interaction at the $C_3S$/CNS interface during the hydration over a timescale of a few nano seconds. The MD simulation of the hydration over much longer time scales to study the oligomerization of silicate "Dreierketten" chain and the deposition of C-S-H nanoscale colloidal cluster is time consuming and thus is omitted from this study.

By combining density functional theory and molecular dynamics simulation using a reactive potential, we aim to ambiguously elucidate the influences of CNSs on the reactivity and hydration mechanism of $C_3S$, the most reactive phase in anhydrous ordinary Portland cement. First, a detailed electronic analysis can reveal the reactivities of both CNS and $C_3S$ phases and detect the dominating active sites for potential reactions. The bond formation mechanism among different atom species based on the PDOS analysis from DFT can set up a base for analysis of reaction kinetics and hydration product nucleation process in MD simulation. Such DFT calculations can consolidate our understanding and shed light on the fundamentals of chemical interactions between the CNS and $C_3S$ surfaces. This enables us to uncover kinetics responsible for the increase in the hydration of cement.

The outcomes of DFT (including the geometry-optimized crystal structure, and the subsequent cleaved $C_3S$ surface) were used as inputs to directly observe the hydration of $C_3S$ surfaces in contact with the bulk water containing CNS via reactive MD simulations. The reactivity and hydration mechanism employed in our DFT can be further confirmed by examining the sol-gel interaction process using MD simulations. This combined DFT and MD approach allows us to study both the initial and the longer-term hydration behaviors, and establish correlations between the electronic property and the chemical reactivity of both CNS and $C_3S$ phases, which is critical to understanding the relevant physiochemical processes during hydration and dissolution of the $C_3S$/CNS hybrid composite.

### 2.3. Experimental characterization of the hydrate phases growth

Experimental tests were conducted to quantify the change in the hydrate phases of OPC as a result of CNS and support the findings of the MD simulations. Cement matrices were prepared by mixing OPC CEM I 52.5N (Table 1) and water with a water-to-cement ratio of 0.35. To realistically quantify the effect of CNS on the DOH of cement for practical applications, the CEM I 52.5N was used in this experiment. The CEM I consists of tricalcium silicate, dicalcium silicate, tricalcium aluminate and

calcium alumino-ferrite. Its mix proportion was determined as $C_3S$: $C_2S$: $C_3A$: $C_4AF$=57.1:17.4:6.2:6.9. The cement used in the present study was not a pure form of Alite, and because of this the authors are fully aware that deviations between the experimental test results and the MD predictions are expected. In order to eliminate and minimize the test errors, we have repeated the experiments for one mix proportion with a fixed CNS dosage and the results were then averaged to probe the effect of CNS on the DOH from a statistic approach.

The commercially available high-efficiency water reducer (Glenium 51) of 1.0 wt% was used to enhance the workability of the cement pastes. The cement pastes were prepared at CNS concentrations of 0, 0.1, 0.2 and 0.4 wt%. The water-to-cement ratio was adjusted to account for the water in the CNS suspension. During the paste preparation process, the CNS suspensions were first mixed with the required amount of superplasticizer and water. Then the resulting aqueous solutions were treated with mild sonication in an ice bath environment for 30 minutes. Subsequently, the obtained solutions were blended with the cement powder and mixed for 8 minutes. The obtained pastes were then poured into (50 mm×50 mm×50 mm) molds and shaken for 1 minute with a vibrator in order to remove air bubbles. After casting, the molds surface was sealed with a plastic film to minimize water evaporation during hydration. The samples were demolded after curing 24 hours and cured in water at a temperature of 21ºC for 28 days. Three samples per CNS concentration were prepared and used to quantify the effect of CNS on the hydration of OPC matrices after 28 days of curing.

Table 1 Chemical composition of CEM I 52.5N cement

| $SiO_2$(%) | $Al_2O_3$(%) | $Fe_2O_3$(%) | CaO(%) | MgO(%) | $SO_3$(%) | $K_2O$(%) | $Na_2O$(%) | Cl(%) |
|---|---|---|---|---|---|---|---|---|
| 21.46 | 4.79 | 2.29 | 64.98 | 2.25 | 3.33 | 0.56 | 0.29 | 0.05 |

A combined Thermography Analysis (TGA) and Differential Scanning Calorimetry (DSC) tests were carried out on the 28-d cured cementitious nanocomposite samples to quantify the effect of CNS on the growth of their hydrate products based on their thermal behavior. The TGA was used to evaluate the mass change of the heated samples under controlled conditions whereas the DSC was used to measure the amount of heat difference during elevation of temperature. The previously prepared cubic samples were ground into powder using a planetary ball mill (Planetary Ball Mill PM 100). Sieved powder samples (fineness less than 1 mm) of weight of 30 mg were then transferred to the TGA-DSC (STA 449 F3 Jupiter) crucibles for thermal analysis and the temperature of the samples was raised

from 20 °C to a critical temperature of 140 °C at a rate of 10 °C /min. The heating temperature of 140 °C was maintained for 30 minutes to remove the free water and the residual mass of the sample under this temperature was set as the benchmark. Subsequently, the samples were heated from 140 °C to 1100 °C at a rate of 10 °C/min. The entire TGA/DSC experiment was performed in a nitrogen environment with an inert atmosphere nitrogen flow rate of 25.00ml/min. The change in the mass of the samples along with the samples heat capacity difference were analyzed to study the influence of CNS on the thermal and kinetic reactions of OPC hydration and quantify the change in the degree of hydration due to the synergistic effects between the $C_3S$ and the CNS.

Scanning Electron Microscope (SEM, JEOL, JSM-7800F) was used to examine the effect of CNS on the morphology of the microstructure of the cementitious nanocomposites at a working voltage between 5 and 15 kV. Cementitious fragments were first dried in a vacuum oven at 80 ° C for 24 hours then their surface was coated with gold in order to provide a homogeneous surface for analysis and imaging. Transmission electron microscope (TEM) (JEM -1010) was employed to characterize the CNS on the growth of the hydrate phases. The cementitious composites in the form of powder samples were mixed with acetone solution and were then sonicated for 15 minutes using an ultrasonic oscillator. The solutions were dropped on carbon-coated copper grids (300 mesh) and left to dry at room temperature. Upon drying, TEM images were generated at 80 kV accelerating voltage. X-ray diffraction (XRD) (Agilent SuperNova) was also employed to further examine the degree of hydration and determine the crystallinity of the hydrate phases. The cementitious composites in the form of powder samples were dried in a vacuum oven for 24 hours at 80° C and coated with gold before analysis. The working voltage of the XRD ranged from 5kV to 15kV. XRD patterns were recorded at a scanning rate of 2°/min from $2\theta = 5°$ to 90° with Cu Kα radiation ($\lambda = 1.5418$ Å).

## 3. Results and discussions

### 3.1 Morphology of CNS

The molecular structure and SEM/TEM micrographs showing the morphology of the CNS are depicted in Fig.4. The CNS crystalline molecules are formed from repeating saccharide units that are covalently linked by a β-1-4 glycosidic(C-O-C) bond. Different functional groups including the hydroxymethyl group(-$CH_2OH$), hydroxyl group(-OH) and hydrocarbon methine group(-H) are grafted on the backbone tetrahydropyran ring (Fig. 4a). The saccharide units are then polymerized to form a single chain. As can be seen from the SEM images of the dry state CNS (Figs.4b-c), the CNS

microfibrils are stacked tightly during the biosynthesis process, resulting in the formation of semi-crystalline CNS sheets. As shown in the TEM images in Fig. 4(d-e), the CNS microfibrils are further composed of randomly oriented nanofibrils, as result of the stacking of CNS molecular chains. These CNS nanofibrils and cellulose chains in dry state still relatively uniformly dispersed throughout the cement matrix and interact with the cement particles during hydration.

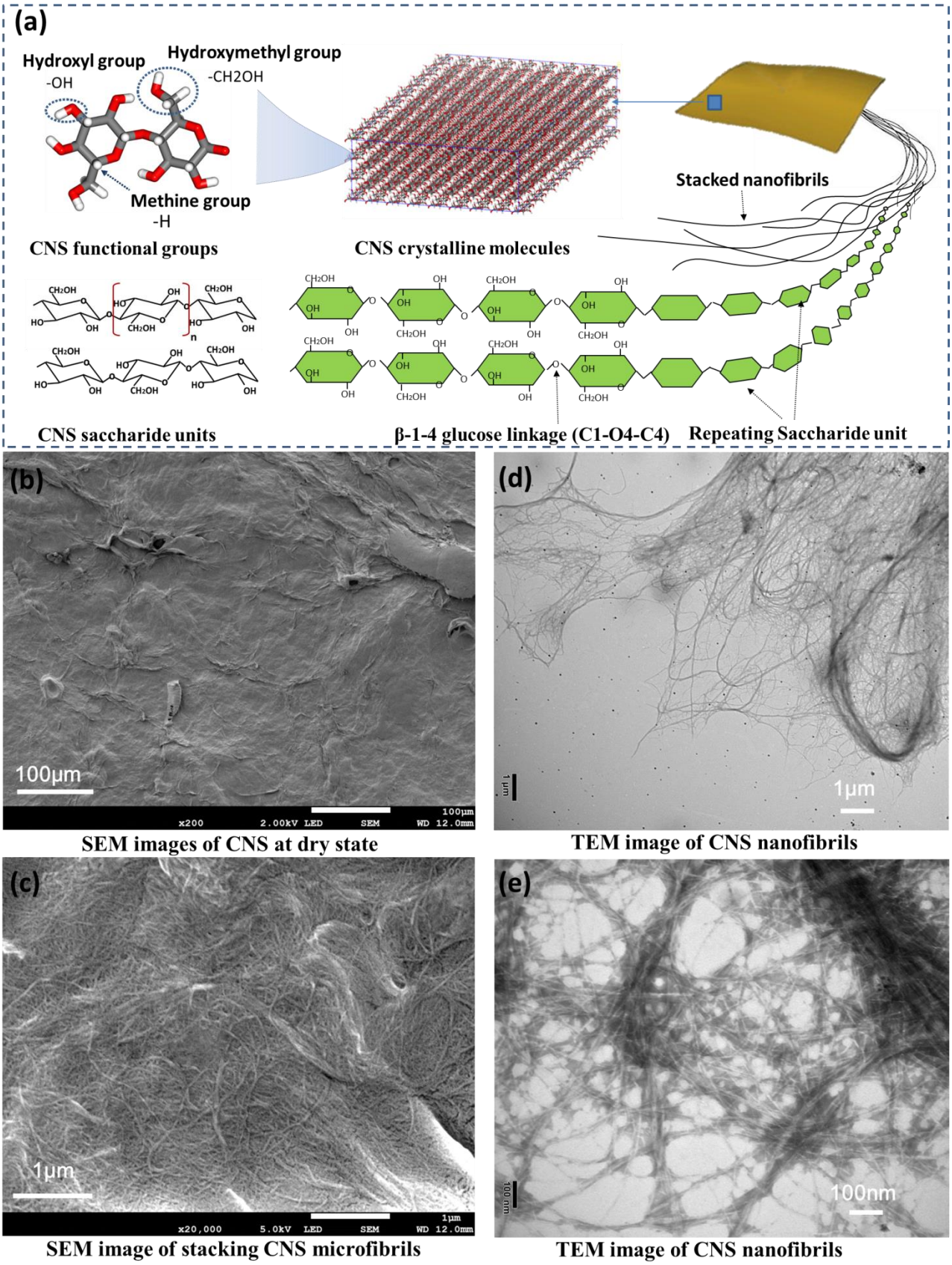


Fig.4 Chemical structure and morphology of CNS

### 3.2 DFT simulation results

DFT simulations are performed to calculate the electronic properties and uncover the atomic mechanism of interactions at $C_3S$/CNS interface. First, the relaxed lattice parameters of CNS Iα and Iβ crystals, and the $C_3S$ crystalline primitive cell are calculated and validated using previous experimental data [29,32,33]. Table 2 indicates that the DFT predicted lattice parameters are in a good agreement with the reported experimental lattice parameters with an estimated error less than 1.5 % for all the 3D cell parameters of $C_3S$ and CNS crystals.

Table 2 Lattice parameters obtained from DFT calculations

| | $C_3S$ | | | Cellulose Iα | | | Cellulose Iβ | | |
|---|---|---|---|---|---|---|---|---|---|
| | DFT | Expt | Error(%) | DFT | Expt | Error(%) | DFT | Expt | Error(%) |
| *a*(Å) | 12.142 | 12.235 | 0.76 | 6.671 | 6.717 | 0.69 | 7.776 | 7.784 | 0.10 |
| *b*(Å) | 7.107 | 7.073 | 0.48 | 6.027 | 5.962 | 1.08 | 8.196 | 8.201 | 0.06 |
| *c*(Å) | 9.349 | 9.298 | 0.55 | 10.371 | 10.400 | 0.28 | 10.385 | 10.380 | 0.47 |
| *α*(°) | 89.963 | 90.000 | 0.04 | 119.733 | 118.080 | 1.38 | 90.003 | 90.000 | 0.00 |
| *β*(°) | 115.844 | 116.310 | 0.40 | 111.423 | 114.800 | 3.03 | 90.012 | 90.000 | 0.01 |
| *γ*(°) | 89.997 | 90.000 | 0.00 | 82.439 | 80.370 | 2.51 | 96.526 | 96.550 | 0.02 |

As shown in Table 3, the key structural inter-chain parameters of CNS crystalline obtained from DFT are also validated using experimental results [52,53] in terms of glycosidic dihedral angles Φ (O5-C1-O4-C4) and Ψ(C1-O4-C4-C5), glycosidic bond angle $\tau$ (C1-O4-C4) and hydroxymethyl dihedral angles including $\chi$ (O5-C5-C6-O6) and $\chi'$ (C4-C5-C6-O6).

Table 3 Comparisons of structural intra-chain parameters for crystalline cellulose Iα and I β

| | Iα | | | | I β | | | |
|---|---|---|---|---|---|---|---|---|
| | DFT | | EXPT | | DFT | | EXPT | |
| | Residue1 | Residue2 | Residue1 | Residue2 | Chain1 | Chain2 | Chain1 | Chain2 |
| Φ (°) | 90.4 | 96.7 | 98 | 99 | 94.8 | 88.6 | 99 | 89 |
| Ψ (°) | 146.3 | 148.3 | 138 | 140 | 142.7 | 147.9 | 142 | 147 |
| $\tau$ (°) | 117.2 | 116.5 | 116 | 116 | 116.9 | 116.9 | 115 | 116 |
| $\chi$ (°) | 165.7 | 150.0 | 167 | 166 | 165.7 | 161.6 | 170 | 158 |
| $\chi'$ (°) | 77.7 | 75.8 | 75 | 74 | 76.9 | 78.4 | 70 | 83 |

These angles are pertaining to the independent glycosylic residues for cellulose Iα unit cell, and to the two nonequivalent chains for the cellulose Iβ unit cell [54]. For the Iα phase, the two glucopyranosyl residues are nonequivalent within one repeating cellobiose, whereas for the Iβ phase, the glucopyranose units within one cellobiose are equivalent but slightly different between the two D-glucose chains[55]. This phenomenon is successfully reproduced by our DFT simulations.

As shown in Table 3, the agreement between the DFT results and the experimental results for the dihedral and the bond angles are within 10%. The DFT results for both $C_3S$ and CNS are within the range observed from the available experimental data [29,52,53,56,57]. Based on the above comparisons, the validity of the DFT calculations is thus confirmed, which sets a clear benchmark for the following electronic description of the $C_3S$ and the CNS crystals.

The Fukui function[58]is employed to study the interaction of the $C_3S$ with the CNS during hydration. This function is widely utilized to determine the chemical reactivity of molecules towards other molecules for bulk systems or specific surfaces. The Fukui function f(r) is defined as the differential change in the electron density ($\rho(r)$) of a molecular system with respect to the differential change in the total number of electrons (N): $f(r) = (\partial\rho(r)/\partial N)$[59,60]. Its field distribution provides useful information on the reactivity localization in bulk systems, where the regions that are marked by electronic clouds are likely to undergo higher chemical reactivity. Like the Frontier Orbital Theory (FOT), the Fukui function is particularly useful for understanding how nucleophiles attack the highest occupied molecular orbital (HOMO) while at the same time placing their surplus of electrons into the lowest unoccupied molecular orbital (LUMO). The electrophilic attack (defined as: $f^{-}(r) \sim \rho_{HOMO}(r)$) is associated with the charge donation that induces an electron decrease in the system. The nucleophilic attack (governed by $f^{+}(r) \sim \rho_{LUMO}(r)$) indicates that the system accepts an electron charge thus causing an electron increase. For bulk systems, the HOMO and LUMO are described by the valence band maximum (VBM) and conduction band minimum (CBM), respectively[56,57].

*3.2.1 Electronic properties of $C_3S$*

Figs.5a-c show the optimized geometry of the MIII-$C_3S$ crystal structure together with the obtained HOMO, total electron density and LUMO orbital distributions. There are two types of oxygen in the $C_3S$ primitive cell: the first type is the tetrahedral oxygen (Ot) covalently bonded to silicon atoms forming silicate tetrahedron groups with Si-O bond lengths between 1.61−1.68 Å. The second type is the dangling oxygen (Od) having an ionic character and coordinated with 5 or 6 calcium atoms with a Ca-O ionic bonding distance within 2.38−2.46 Å. As expected, the HOMO orbital density for the $C_3S$ unit is mainly concentrated around the dangling ionic oxygen Od atoms, implying that the Od atoms serve as nucleophiles and are more susceptible to react with the environmental electrophiles (e.g $H^{+}$) to form oxides or hydroxyls. The tetrahedral oxygen Ot atoms also show potential to react with the proximate $H^{+}$ protons leading to the hydration of orthosilicate $[SiO_4]^{4-}$ and the formation of

silicic acid such as dihydrogen orthosilicate ions $H_2SiO_4$ and trihydrogen orthosilicate ions $H_3SiO_4$. Figures 5a-c show that the LUMO orbital density of $C_3S$ has a more delocalized electron distribution with its partial charge density exists at interstitial sites among the silicon tetrahedra and accumulates in the vicinity to the calcium atoms. This suggests that these particular sites are more prone to experience nucleophilic attack by $OH^-$ groups from water dissolution and hydroxyl functional groups from the CNS. These findings are consistent with the reported feature of $C_3S$ obtained from DFT calculations[56,57,61].

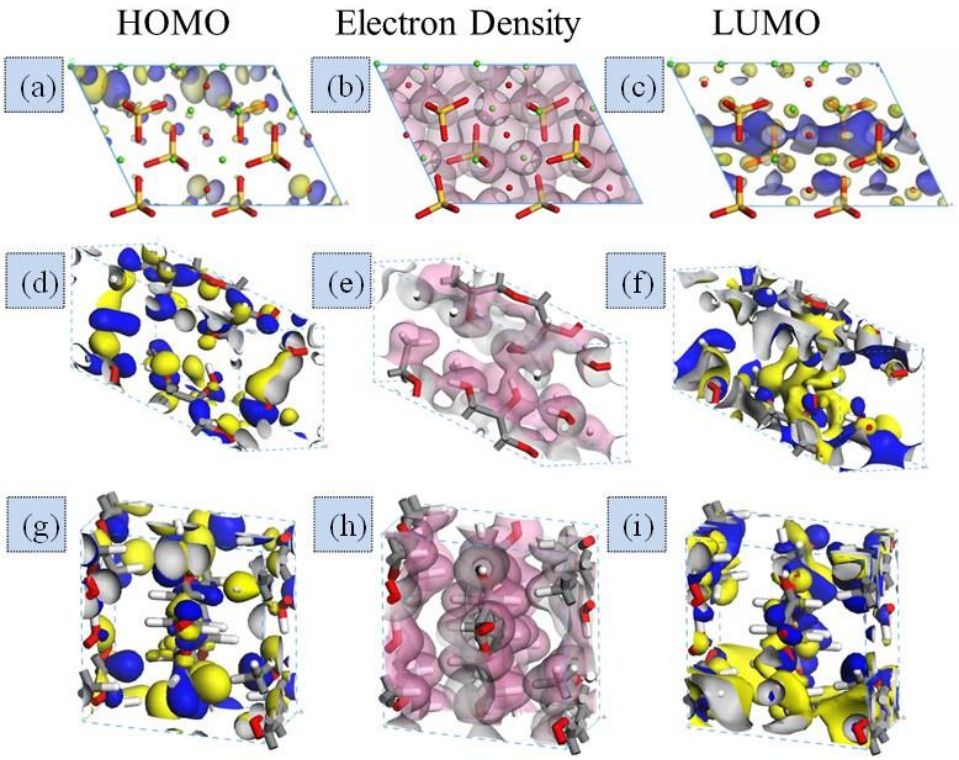


**Fig.5** HOMO, Electron density and LUMO density of crystals with field isosurface level of ±0.02e $Å^{-3}$. (a-c) $C_3S$ primitive cell. (d-f) CNS Iα phase primitive cell. (g-i) CNS Iβ phase primitive cell.

*3.2.2 Electronic properties of CNS crystals*

Figure 5d-f and 5g-i show the HOMO, electron density and LUMO density of CNS Iα and Iβ crystals, respectively. As shown, the HOMO orbital distributions of the CNS Iα and Iβ units are mainly localized around the oxygen atoms of the functional groups and the glycosidic linkage. According to the FOT, these oxygen atoms are likely to lose electrons compared to the rest of the system. Therefore, the oxygen atoms are the reaction sites that will undergo electrophilic attack and interact with the environmental cations, such as $Ca^{2+}$ from the $C_3S$, or $H^+$ proton from the bulk water. The LUMO orbitals of the CNS units show much denser electronic clouds capping over the whole backbone

carbon and hydrogen atoms from the functional groups of CNS. This implies that the electrophilic sites (C and H) on the surface of CNS react with the surrounding anions such as the dissociated water groups $OH^-$.

*3.2.3 Partial density of states of $C_3S$*

In addition to examining the electron localization in the $C_3S$ structures and the CNS unit cells, the spin-unrestricted partial density of states (PDOS) are also calculated to 1) understand the origin of the electronic structure, 2) unravel the nature of orbital hybridization and bonding mechanism in the bulk system, and 3) clarify both the contribution of respective orbitals to the total density of states (DOS) near band edges and the trend to donate or withdraw electrons. The location of Fermi energy level ($E_F$) is assigned as zero energy scale[62] and is marked by a dashed line. All energies are relative to the Fermi level.

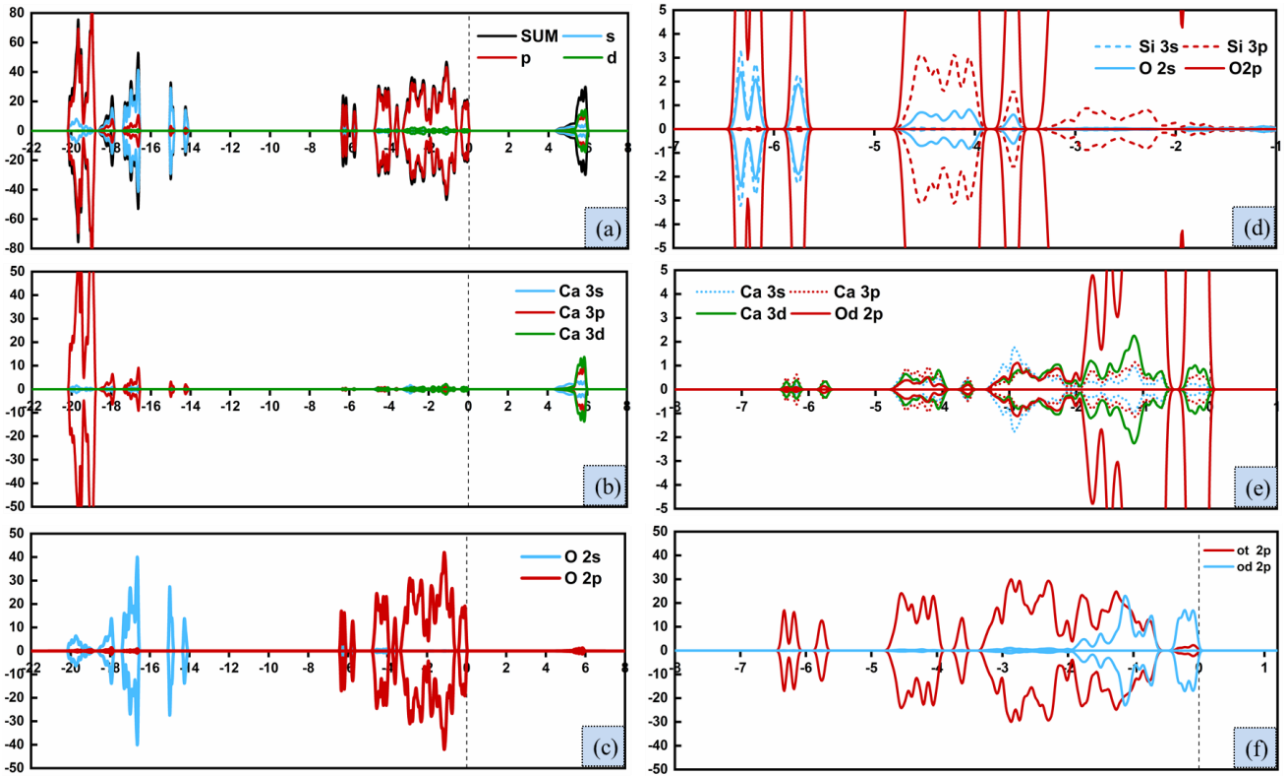


**Fig.6** Spin polarized PDOS of $C_3S$ crystal. a) total density state of s, p, d orbitals. b) PDOS of Ca-3s, Ca-3p, Ca-3d orbitals. c)PDOS of O-2s, O-2p orbitals. d)hybridization of Si-3s, Si-3p orbitals with O-2s and O-2p orbitals at medium energy level. e) resonance of Ca-3d and O-2p orbitals. f) LDOS of Od and Ot atoms

Fig.6 shows the total and orbital projected PDOS of $C_3S$. The smearing method with a level broadening of 0.03eV is used to integrate the PDOS. Three main quantum chemical parameters of

$C_3S$ are obtained as $E_{HOMO}$=-7.518eV, $E_{LUMO}$=-2.917eV, and band gap energy $\Delta E = E_{LUMO} - E_{HOMO}$= 4.241eV, which are very close to the previous ab initio calculated values for pure $C_3S$[57]. As can be seen from Figs.6a-c, the valence band (VB) PDOS near the $E_F$ is the result of the O-2p orbitals. The Si-3s and the Si-3p orbitals have slight contributions to the VB at medium range i.e., -2eV to -6.47 eV) but have remarkable orbital $sp^3$ hybridization with O-sp orbitals (see Fig.6d). This indicates the relative stability of the covalent Si-O bonding characteristics. At short range of VB near the $E_F$ (from Fermi level to -2eV), the Ca-3d orbital has the strongest resonance with the Od-2p orbital, implying ionic Ca-O bond connection (see Fig.6e). As depicted in Figs.6b-c, the PDOS valence bands congregate at very low energy levels between -14 eV to -20 eV which corresponds to O-2s and Ca-3p orbitals. These two states are far away from $E_F$ and are known to be relatively stable with energetically unfavorable to electron exchange with the surrounding environment in comparison to the O-2p states. On the other hand, the conduction band (CB) PDOS above the $E_F$ is dominated by all s, p, d states from calcium cations. This further confirms that the chemical reactivity of $C_3S$ is primarily attributed to the O and Ca atoms, which is in line with the observations obtained from the HOMO and LUMO orbital electron clouds.

Figure 6f compares the local density of states (LDOS) for different oxygen species in the $C_3S$ cell. As can be seen, the density of Od atom in the VB is significantly higher than the Ot near the Fermi energy. This is partially attributed to their different charge transfer properties. According to the reported Bader charge analysis of the pure MIII-$C_3S$ structure[56], the net charge of each dangling ionic oxygen Od is -1.54 e and the net charge of each tetrahedral oxygen Ot is -1.45e. This means the Od withdraws an additional 0.09e charge from the system, indicating that when more charge is localized in the HOMO, the Od-2p orbitals around the maximum valence band is enhanced. This indicates that the Od site is more chemically reactive and is more susceptible to adsorption of electrophilic species than the Ot site.

*3.2.4 Partial density of states of CNS crystals*

For the CNS unit cell, the spin polarized PDOS of Iα and Iβ crystals are plotted in Fig.7. As shown, the Iα and Iβ cellulose primitive cells exhibit similar PDOSs, and the predicted band energy gaps is 5.349eV for the Iα crystal and 5.653 eV for the Iβ crystal (see Figs.7a,b). The relatively large band gaps with almost matching spin-up and spin down orbital states indicate that the native cellulose is a nonmagnetic semiconductor. The slightly lower value of the band gap energy of Iα polymorph with

more DOS in the higher energy level of conduction band further confirms its meta-stable state in comparison to Iβ polymorph.

As clearly indicated in Fig.7, the top of the valence bands (TVB) near the $E_F$ for both Iα and Iβ cellulose crystals are mainly provided by the 2p orbitals of oxygen atoms (see Figs.7c, d). As expected, the oxygen atoms exhibit a clear electron donating trend. Slight contributions of the 2p orbitals of carbon atoms are also observed in Figs.7e, f. The bottom of the conduction bands (BCB) are mainly the contribution of the C-2p and H-1s orbitals in both Iα and Iβ crystals as shown in Figs.7e-h.

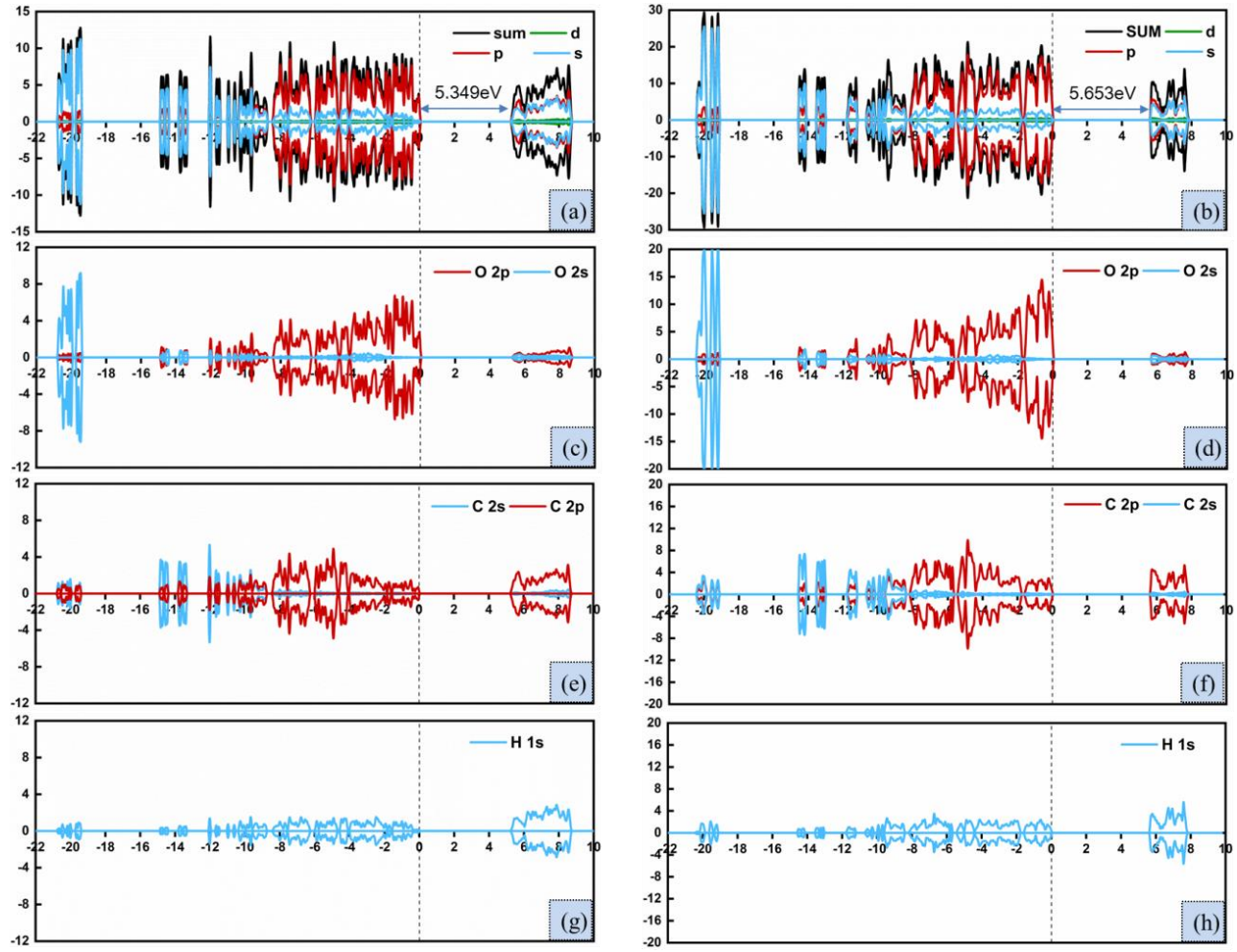


**Fig.7** Spin polarized PDOS of Iα and Iβ crystal. a) total density state of s,p,d orbitals for Iα phase. b) total density state of s,p,d orbitals for Iβ phase. c) PDOS of O-2s, O-2p orbitals for Iα phase. d) PDOS of O-2s, O-2p orbitals for Iβ phase. e) PDOS of C-2s, C-2p orbitals for Iα phase. f) PDOS of C-2s, C-2p orbitals for Iβ phase. g) PDOS of H-1s orbitals for Iα phase. h) PDOS of H-1s orbitals for Iβ phase.

Figure 8a presents the VB LDOS of 2p orbitals for different oxygen atom species for the Iα structure This figure indicates that the largest contribution to the TVB around the $E_F$ is attributed to the O6

sites resulting from the hydroxymethyl conformation of Iα phase (the atom numbering is given in Fig.2). Figure 8b shows that for the Iβ phase, the most occupied energy level for the O6 site in the hydroxymethyl group is distinct from the other oxygen sites. The peak position of VB PDOS near the Fermi level for O6 site lies at higher energy by about 0.114 eV than those for the other oxygen sites (marked as dash arrow in Fig.8b). This implies that the O6 atoms with smaller energy gap between the highest occupied energy level and the Fermi level is expected to exhibit higher chemical reactivity during hydration. The methyl oxygen atoms pointing out from the glucopyranose ring are more vulnerable to electrophilic attack. The other oxygen sites (O2, O3, O4 and O5) are showing similar reactivity as they possess the same peak position in the VB PDOS.

With respect to the bottom of the conduction bands (BCB), the carbon atoms C4, C5 and C1 that are directly connected to the backbone oxygen (O5, O4) dominate the contributions to the BCB, followed by the C6, C2 and C3 sites as shown in Figs.8c,d for Iα and Iβ phases, respectively. These carbon sites possess nearly identical peak positions at the BCB nearest to the $E_F$, implying a similar energy barrier for electrons gain. This suggests that all carbon sites play almost an equal role in the chemical reaction with the environmental nucleophiles such as Ow from water.

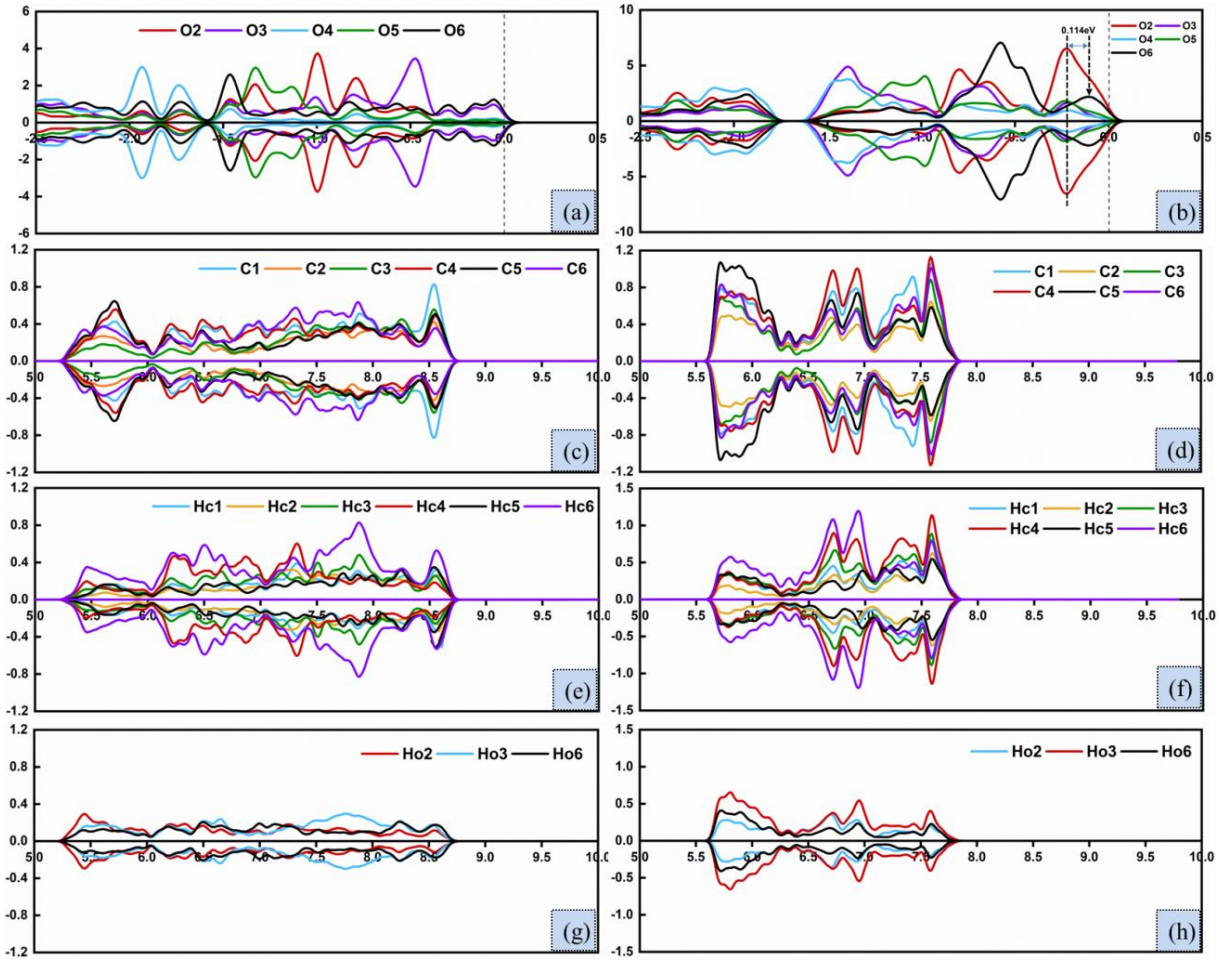


**Fig.8** Spin polarized LDOS of for different atom species in CNS Iα and Iβ crystals. a) LDOS of oxygen atoms for Iα phase. b) LDOS of oxygen atoms for Iβ phase. c) LDOS of carbon atoms for Iα phase. d) LDOS of carbon atoms for Iβ phase. e) LDOS of hydrogen atoms from methine group for Iα phase. f) LDOS of hydrogen atoms from methine group for Iβ phase. g) LDOS of hydrogen atoms from hydroxyl/hydroxymethyl group for Iα phase. h) LDOS of hydrogen atoms from hydroxyl/hydroxymethyl group for Iβ phase.

The hydrogen atoms on the surface of the CNS, are categorized herein as: hydrophobic methine hydrogens (Hc1-Hc6) atoms associated with the carbon atoms from the hydrocarbon moieties (C-H), hydroxyl hydrogens (Ho2 and Ho3) atoms linked to the oxygen in the hydroxyl radical (-OH) and methylene hydrogen (Ho6) atoms connected to the oxygen in the hydroxymethyl functional group (-$CH_2OH$). Among the methine hydrogens atoms illustrated in Figs.8e-f, the contribution of CB PDOS is mainly attributed to the Hc6 site from the hydroxymethyl group. The others Hc1-Hc5 sites also contribute to the formation of the conduction band. It is interesting to note that the LDOS of hydrogen atoms from the functional groups only offer moderate contributions to the whole conduction band (see Figs.8g-h). These contributions, however, are slightly less than those of the methine hydrogens

atoms.

The hydrogen atoms from the functional groups in CNS provide relatively higher charge from the Hirshfeld-based population analysis (see Table 4). This could be attributed to intra-chain hydrogen bonds between the neighboring oxygen such as O2-Ho2…O6, O3-Ho3…O5 and O6-Ho6…O3 bonds as observed in reported experiments[63,64]. As a result, their capacity to attract environmental electron is weakened. However, the reactivity sequence for these different atom sites is generally a correlated trend of the atomic Hirshfeld charge obtained from the population analysis. This confirms the reactivity of different atom species on the surface of CNS. In this case, the atoms carrying higher positive charge are more likely to attract electrons from their neighbors whereas the atoms with lower electronegativity are prone to donate electrons to their neighbors. Because of this, the CB PDOS results show that the C and H atoms are the main active atoms of CNS that are susceptible to nucleophilic attack such as Ow anion from water hydrolysis and Od anion and $[SiO_4]^{4-}$ group as a result of $C_3S$ dissolution. Moreover, the O atoms on the surface of CNS are prone to electrophilic attack by the electrophiles such as $Ca^2$ cations in the $C_3S$ surface.

Table 4 Hirshfeld population for different atom species in CNS

| Atoms species | Hirshfeld charge of Iα phase | | | Hirshfeld charge of Iβ phase | | |
|---|---|---|---|---|---|---|
| | Residue 1 | Residue 2 | SUM | Chain 1 | Chain 2 | SUM |
| O2 | -0.186 | -0.170 | -0.356 | -0.196 | -0.192 | -0.388 |
| O3 | -0.200 | -0.196 | -0.396 | -0.157 | -0.169 | -0.326 |
| O4 | -0.096 | -0.086 | -0.182 | -0.093 | -0.095 | -0.188 |
| O5 | -0.096 | -0.100 | -0.196 | -0.099 | -0.095 | -0.194 |
| O6 | -0.196 | -0.150 | -0.346 | -0.168 | -0.163 | -0.331 |
| C1 | 0.093 | 0.096 | 0.189 | 0.094 | 0.093 | 0.187 |
| C2 | 0.017 | 0.018 | 0.035 | 0.017 | 0.015 | 0.032 |
| C3 | 0.018 | 0.018 | 0.036 | 0.021 | 0.024 | 0.045 |
| C4 | 0.030 | 0.026 | 0.056 | 0.027 | 0.027 | 0.054 |
| C5 | 0.027 | 0.028 | 0.055 | 0.033 | 0.032 | 0.065 |
| C6 | 0.011 | 0.001 | 0.012 | -0.008 | -0.013 | -0.021 |
| Hc1 | 0.038 | 0.040 | 0.078 | 0.034 | 0.036 | 0.070 |
| Hc2 | 0.025 | 0.024 | 0.049 | 0.029 | 0.023 | 0.052 |
| Hc3 | 0.028 | 0.031 | 0.059 | 0.030 | 0.034 | 0.064 |
| Hc4 | 0.044 | 0.042 | 0.086 | 0.039 | 0.039 | 0.078 |
| Hc5 | 0.030 | 0.030 | 0.060 | 0.033 | 0.031 | 0.064 |
| Hc6 | 0.025,0.031 | 0.034,0.041 | 0.131 | 0.03,0.023 | 0.025,0.019 | 0.097 |
| Ho2 | 0.122 | 0.107 | 0.229 | 0.100 | 0.097 | 0.197 |
| Ho3 | 0.105 | 0.103 | 0.208 | 0.110 | 0.108 | 0.218 |
| Ho6 | 0.101 | 0.115 | 0.216 | 0.107 | 0.110 | 0.217 |

Based on the above analysis, it can be postulated that the HOMO and the LUMO in $C_3S$ and CNS unit cells are very likely to overlap and form $C_3S$/CNS complex hydration products, where formation of new Ca-O and O-H chemical bonds between different atom species can be induced by the molecule dissociation and the atom diffusion. The $C_3S$ suffers simultaneously nucleophilic and electrophilic attacks from CNS and water molecules during the hydration process. This is because the Ca atom is an electron acceptor for the water oxygen (Ow), CNS backbone oxygen (Oc) and the functional group oxygen (Oh). In addition, the Ot and Od atoms act as electron donors that accept H+ proton from water (Hw), as well as hydrogen from CNS methine groups (Hc) and hydroxyl/hydroxymethyl functional groups (Ho). This also leads to the formation of complex hydration products.

### 3.3 Molecular dynamics simulation

Determining the solute and solvent-mediated reaction kinetics at the $C_3S$/CNS interface from the first principles DFT calculations at quantum mechanics levels is difficult[65,66]. Therefore, we perform larger scale reactive MD simulations to understand the effect of CNS on the chemical reactivity of $C_3S$ and unravel the molecular interaction at the interface between $C_3S$ and CNS during hydration[67]. Figures 9a-g shows the molecular structure evolution processes for the $C_3S$/water system (shown in Fig.3c) and Figs. 9h-n shows the molecular structure evolution processes for the $C_3S$/water/CNS chains system (shown in Fig.3d). The snapshots of the microstructure configurations are illustrated at simulation time of 0ps, 1ps, 10ps, 100ps, 1ns, 2ns and 3ns, respectively. The hydration progress of $C_3S$ in the presence of CNS/water solution can be described by the following four processes taking place at the $C_3S$/CNS interface: water dissociation → CNS chain dissolution → proton hopping → silicate oligomerization. These interfacial chemical reactions may occur in sequence, in parallel, or in complex combination during the early hydration period. These processes are discussed in detail in the following sections.

***Interaction of $C_3S$ with water.*** For the $C_3S$/water system without the CNS chains, the water hydrolysis is observed at the solid-liquid interface immediately after the onset of the nanocomposite system relaxation. Some water molecules are dissociated into hydroxyl group ($OH^-$) and hydrogen proton ($H^+$) without the formation of hydronium ion($H_3O^+$). This leads to instant surface hydration due to the high reactivity of the dry state of the $C_3S$ crystal (Figs.9o-p). This rapid water dissociation further demonstrates the strong hydrophilic nature of the $C_3S$ surface and its susceptibility to attacks by the protons and OH groups to form hydration products. There is a large amount of ionic oxygen anions

and under-coordinated calcium cations congregated at the bare surface of $C_3S$, which can interact with the OH group and $H^+$ proton resulting from water dissociation. This results in $C_3S$ surface hydroxylation[68]. However, after the occurrence of initial rapid hydration of the exposed surface, the further hydration of the $C_3S$ crystal seemingly enters a dormant period (or induction period) at a medium time scale, in which the reaction drastically decelerates and reaches a steady state regime. The reactive surface transformed into a stable ice-like monolayer and further hydration is retarded with barely nucleated calcium hydroxides at the $C_3S$/water interface, shown as the green layer in Figs.9a-g. No silicate oligomerization can be observed within the current simulation time. This is in good agreement with previous findings, which pinpoint a water tessellation/patterning effect for the well-organized surface configuration[49].

***Interaction of $C_3S$/CNS chains with water.*** The initial rapid $C_3S$ surface hydroxylation also happens for the nanocomposite systems at the $C_3S$/CNS interface. However, different from the phenomenon observed during the reaction of $C_3S$ with water, the initial regular steric arrangement of $C_3S$ is highly disturbed at the $C_3S$/CNS interface. The basal structure of $C_3S$ gradually loses its crystalline order with nucleation of a disordered intermediate calcium hydro silicates at the surface. The calcium hydro silicate is an intermediate phase (termed as product B defined by Taylor in literature[69]). It includes a combination of the calcium hydroxide and hydrated silicate monomers (Q0 species) that are the main component for nucleation of C-S-H. The Formation of the final C-S-H product requires the condensation of silicate tetrahedra forming dimers or longer chains at later hydration stage. The calcium atoms are desorbing from the bulk crystal and diffusing toward the aqueous solution due to the affinity of the CNS chains, which yields a larger amount of calcium hydro silicates at the $C_3S$/CNS interface, shown as the green layer in Figs.9h-n. In the meantime, the hydroxylated silicate tetrahedra are subjected to position rearrangement leading to a more amorphous surface. During the continuous interaction, it is intriguingly found that the highly reactive $C_3S$ surface can disrupt the original stability of the proximate CNS chain when is lying closely to the $C_3S$ substrate surface (<5Å), which results in the bond-breakage and dissolution of the CNS material. Furthermore, the surficial alkaline $Ca^{2+}$ ions with divalent charge diffusing away from the $C_3S$ bulk can strongly attract the Oc, Oh atoms from CNS, which facilitates the formation of Ca-O pairs with a final coordination shell at 2.45Å as shown in the RDF pattern in Fig.10a. This strong Ca attraction also causes the CNS ring opening and the C-O-C glycosidic bond stretching until breakage. Together with the Ow from water, a spatial 3-D

Ca-O coordination network is gradually produced at the solid-liquid interface. Subsequently, the bonds in the CNS chain are frequently broken and the carbon atoms from the broken CNS backbone are concurrently reacting, and reassembling with the surrounding oxygen and hydrogen atoms. This results in generation of many C-OH, C-H fragments and creates suspension of mixed organic chemical compounds spreading over the aqueous solution such as Methanol $CH_3OH$, ethanol $CH_2CHOH$ as well as their derivatives Methanediol $CH_2(OH)_2$, ethynediol $C_2H_2O_2$, etc. (See Figs.9q-t). Furthermore, the CNS functional group deprotonation is prevailing during the CNS chain dissolution.

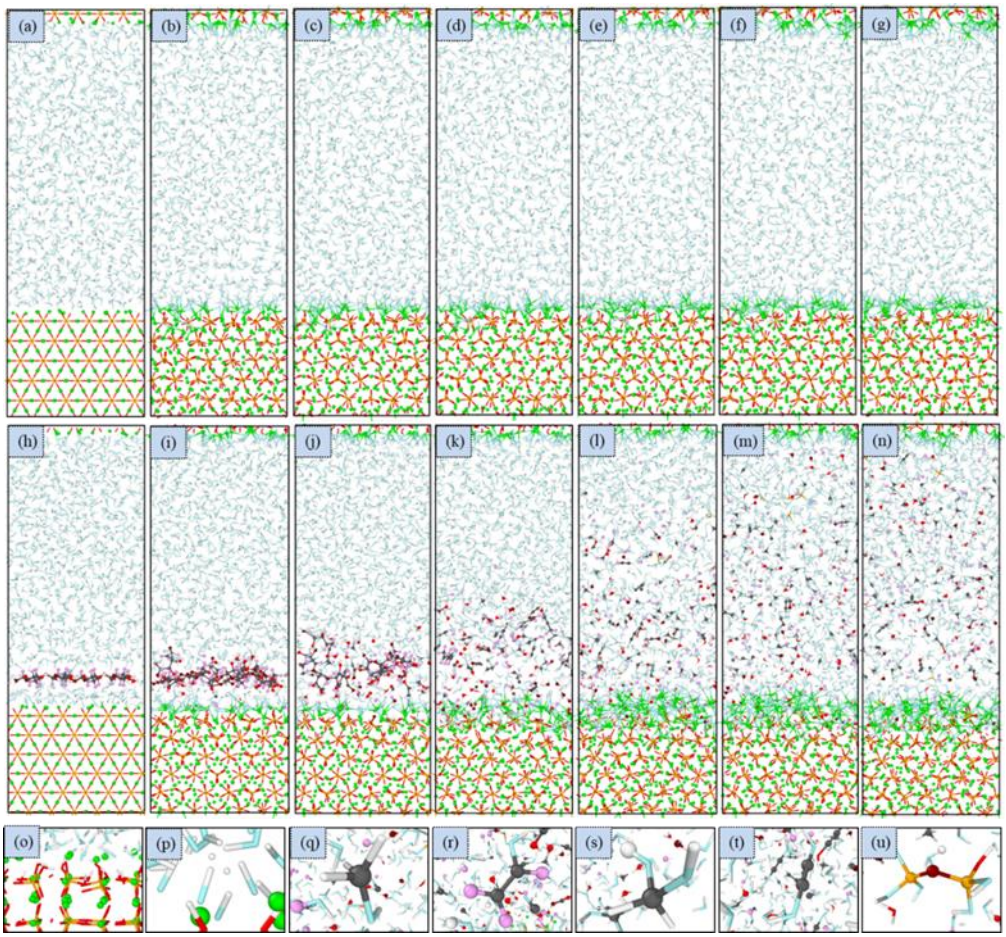


Figure 9 Comparison of microstructure evolution of the composite (a-g) $C_3S$/water system and (h-n) $C_3S$/water/CNS chains system. (o-p) Snapshots representing the water dissociation and fast surface hydroxilation. (q-t) CNS dissolution and functional group deprotonation accompanied by production of organic chemical compounds. (u) Oligomerization of orthosilicate originated from the diffused silicon atoms in the aqueous solution.

The H protons from CNS can be transferred to the dissociated water hydroxyl group ($OH^-$) leading to the composition of new water molecules or connected to the Ot or Od oxygen atoms to further hydroxylate the $C_3S$ substrate surface. The corresponding RDF patterns between the $H_{CNS}$ - $O_{C3S}$ as

well as $H_{CNS}$ - $O_{water}$ are given in Figs.10b-c. As shown, distinct RDF peaks of O-H around 1Å demonstrate the protonation of $C_3S$ oxygen and the formation of recombined water molecules seeded from the CNS. Figures 10b-c indicate that the $H_{CNS}$ protons are mostly connecting to the $O_d$ atoms in the $C_3S$. This is in line with the DFT observation that the $O_d$ atoms having higher HOMO orbital intensity are more susceptible to react with the environmental electrophiles. In addition, some silicate tetrahedra start to dissolve with the silicon and oxygen atoms escaping from the $C_3S$ substrate surface and diffuse into the solution. The diffused silicon atoms covalently rebond with the environmental oxygen atoms that produce silicate monomer or dimer (Fig.9u).

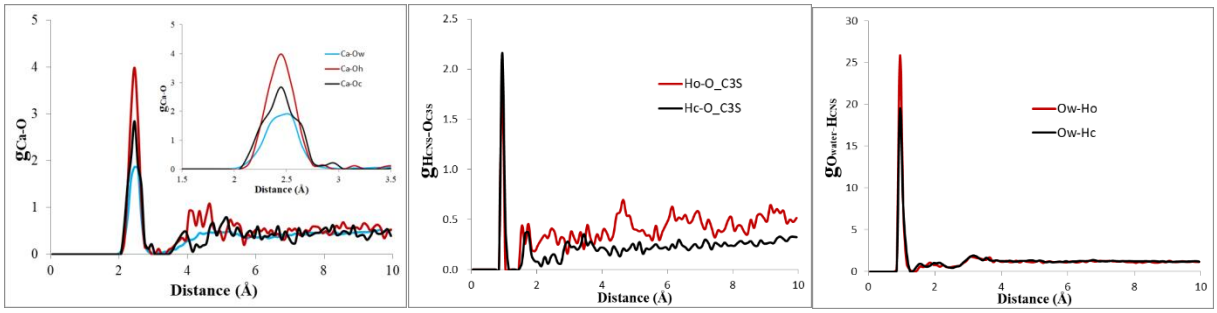


(a) Ca-O (b) $O_{C3S}$- $H_{CNS}$ (c) $O_{water}$-$H_{CNS}$

Fig.10 RDF patterns within $C_3S$/water/CNS chains molecular systems

As discussed above, the $C_3S$ will be hydroxylated and dissolved upon contacting with water, the intermediate calcium hydro silicate phase containing hydrated silicate monomers is forming following the reaction formulation below, which is consistent with the available experimental evidences probed by the $^{29}Si$ NMR test[70,71]:

$$Ca_3SiO_5 + 3H_2O \rightarrow 3Ca^{2+} + H_2SiO_4^{2-} + 4OH^- \quad (2)$$

The oxygen of $C_3S$ can simultaneously connect with the H atoms from the CNS functional groups' deprotonation (H can be Hw, Ho and Hc) and the resulting hydrolysis and hydration equilibriums with respect to the silicic acid species are coexisting during the reaction process described by the following equations[72,73]:

$$O^{2-} + H^+ \Leftrightarrow OH^- \quad (3)$$

$$H_2SiO_4^{2-} + H_2O \Leftrightarrow H_3SiO_4^- + OH^- \quad (4)$$

After initial reaction, the solution is then quickly becoming supersaturated with calcium hydro silicate that has less solubility than $C_3S$. The C-S-H will then precipitate when the supersaturation degree reaches the threshold, which usually occur at longer time scale (from few seconds to hours) [69,74]:

$$nCa^{2+} + 2(n\text{-}1)OH^- + H_2SiO_4^{2-} \rightarrow CaO_n \cdot SiO_2 \cdot H_2O \quad (5)$$

Since not all the calcium ions are consumed during the precipitation of C-S-H, increasing concentration of calcium and hydroxide ions in solution would lead to the maximum supersaturation

of the liquid phase which precipitates portlandite, according to the reaction equation：

$$Ca^{2+} + 2OH^- \rightarrow Ca(OH)_2 \quad (6)$$

where the OH group can be sourced from water dissociation or CNS hydroxyl functional group. As the above reactions proceed, substantial H protons continuously penetrate into the crystal further beneath the surface, protonating free oxygen atoms inside the $C_3S$ structure and break the calcium bonds within the crystal framework. The steady-state reactions of CNS/$C_3S$ system is primarily governed by the Grotthuss-type proton hopping mechanism. The H proton jumps from the CNS hydroxyl groups in the hydrated surface towards the inner oxygen atoms, leaving the deprotonated oxygen atoms free for posterior proton transportation, as shown in Fig.11. Another possible penetration pathway is the H proton exchange between the upper layer orthosilicate t the and deeper layer silicate tetrahedra.

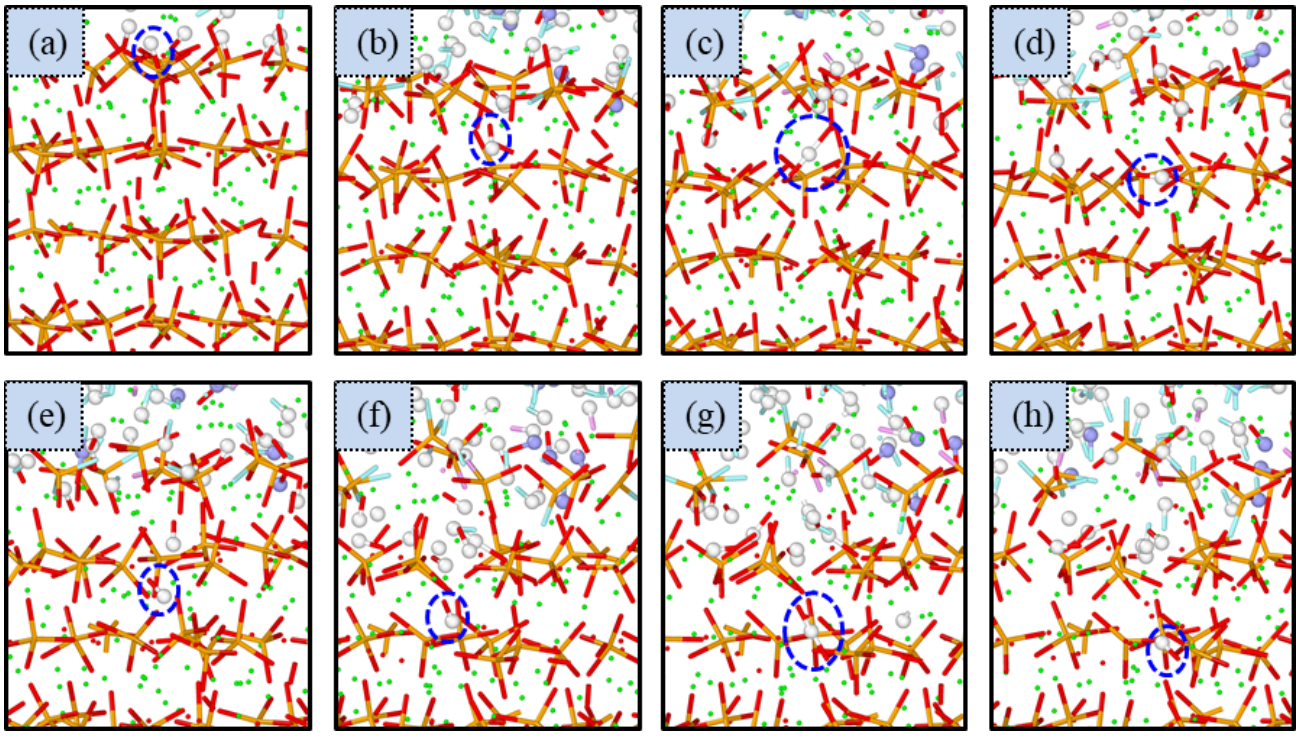


**Fig.11** Snapshots of the proton hopping process. (a) Hydroxylation of $C_3S$ surface after water dissociation. (b) Rotation of hydroxyl group that is pointing towards the second layer silicate tetrahedron. (c) Hydrogen bond formed between the $OH^-$ group and neighboring ionic oxygen. (d) Grotthuss-type proton hopping from the $OH^-$ group towards the inner oxygen with formation of new hydroxyl pair. (e) Rotation of the new hydroxyl pair. (f) Vibration of the new hydroxyl pair pointing towards the third silicate tetrahedral layer with saturation of $OH^-$ groups at the second layer. (g) Dissociation of the $OH^-$ group and protonation of deeper oxygen atom. (h) Proton jumping once again leading to third layer hydroxylation. The proton from water dissociation is depicted using a white ball for clear illustration.

Due to the presence CNS in the aqueous environment, the H protons from the deprotonated functional

groups (Hc,Ho) also contribute to the hydroxylation of the $C_3S$. As a result, a noticeable increase in the hydration depth is noticed as compared to the $C_3S$/water system. One reason for the improved hydration rate is the enhanced water dynamics after the inclusion of CNS. As shown in Fig.12a, the mean squared displacement (MSD) of Hw atoms from water is remarkably increased due to both the "water repelling effect" from the chemical solvent byproducts and the released fracture energy from the CNS chains breaking. The high increase in water dynamics implies that the CNS material can accelerate the diffusion capacity of the water molecules and their deep penetration into the interior core structure of $C_3S$. This further contributes to the hydration degree of $C_3S$. Another reason for the enhanced hydration rate is the enriched H protons and hydroxide ions decomposed from CNS. These protons enable the ionic exchange to take place during hydration. As a result, substantial increase in the calcium hydro silicate precipitates can be observed at the end of the simulation (Fig.9n).

Figure 12b shows the amount of penetrated H protons associated with Od and Ot species in the $C_3S$ crystal for the $C_3S$/water system. The OH density evolution is mainly due to the hydroxylation associated with the dangling Od atoms. The OH density is steadily increased over time reaching about 7 $OH^-/nm^2$ when initial instant hydroxylation occurred at the first couple of picoseconds. However, a plateau is observed for the OH density evolution associated with the tetrahedral Ot atoms that contribute a hydroxyl density of ≈2 $OH^-/nm^2$.

For the $C_3S$/water/CNS chains system, the effect of CNS on the hydration kinetics is evident as shown in Fig.12c. Here, we see that the inclusion of CNS chains can significantly improve the Od-Hw density within the same simulation time. In addition, the H atoms from the CNS also make discernable contribution to the hydroxylation, where the OH density increases at the beginning, followed by a notable curve oscillation, particularly in the case of Od-Hc density evolution. This implies that significant proton exchange phenomenon takes place during the hydration process. Figure12d compares the total OH density for $C_3S$/water and $C_3S$/water/CNS chains molecular systems. The total OH density of the $C_3S$/water/CNS chains system reaches ≈12 $OH^-/nm^2$ at the end of simulation which is significantly larger than that of $C_3S$/water (≈9 $OH^-/nm^2$), confirming that the inclusion of CNS chains can urge the proton exchange reaction.

The $C_3S$ hydration depth evolution is computed by the time-resolved atomic density profiles (TRDP) with the ultimate atom density distribution along the direction perpendicular to [0 1 0] surface for

given Ca, O, H species shown in Fig.13. The evolution of H density is much more evident for the $C_3S$/water/CNS chains system where the hydration depth reaches up to ≈15 Å which higher that than of the $C_3S$/water (≈12 Å). It is also noteworthy that some oxygen atoms from the CNS dissolution can migrate into the interstitial site beneath the $C_3S$ surface, evidenced by the black dash line in Fig.13b. As discussed above, the VB PDOS in pure $C_3S$ is mostly from the O-2p orbitals with the HOMO density mainly accumulated around the dangling ionic oxygen atoms. Those "oxygen migrants" are ionic in nature can contribute to the TVB which could enhance the hydration reactivity of $C_3S$ and therefore facilitate the proton hopping.

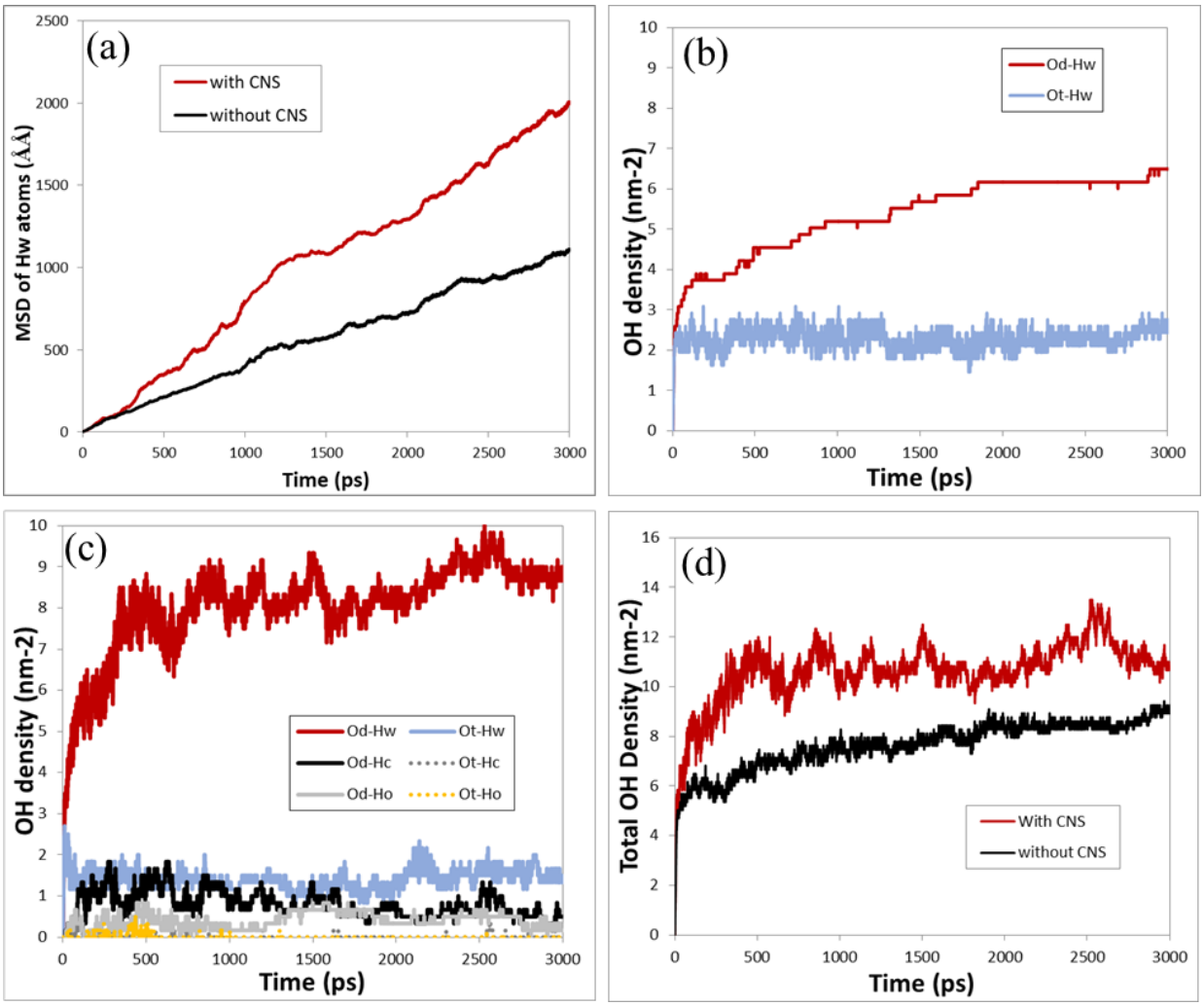


**Fig.12** Features of H proton during microstructural evolution. (a) Comparison of MSD evolutions of water hydrogen atoms between systems with and without CNS. (b) Number evolution of hydroxyl groups per unit of exposed surface with respect to time for $C_3S$ contacting with bulk water. (c) Contribution of different H proton types associated with different oxygen species for nanocomposite system. (d) Comparison of OH density for systems with and without CNS

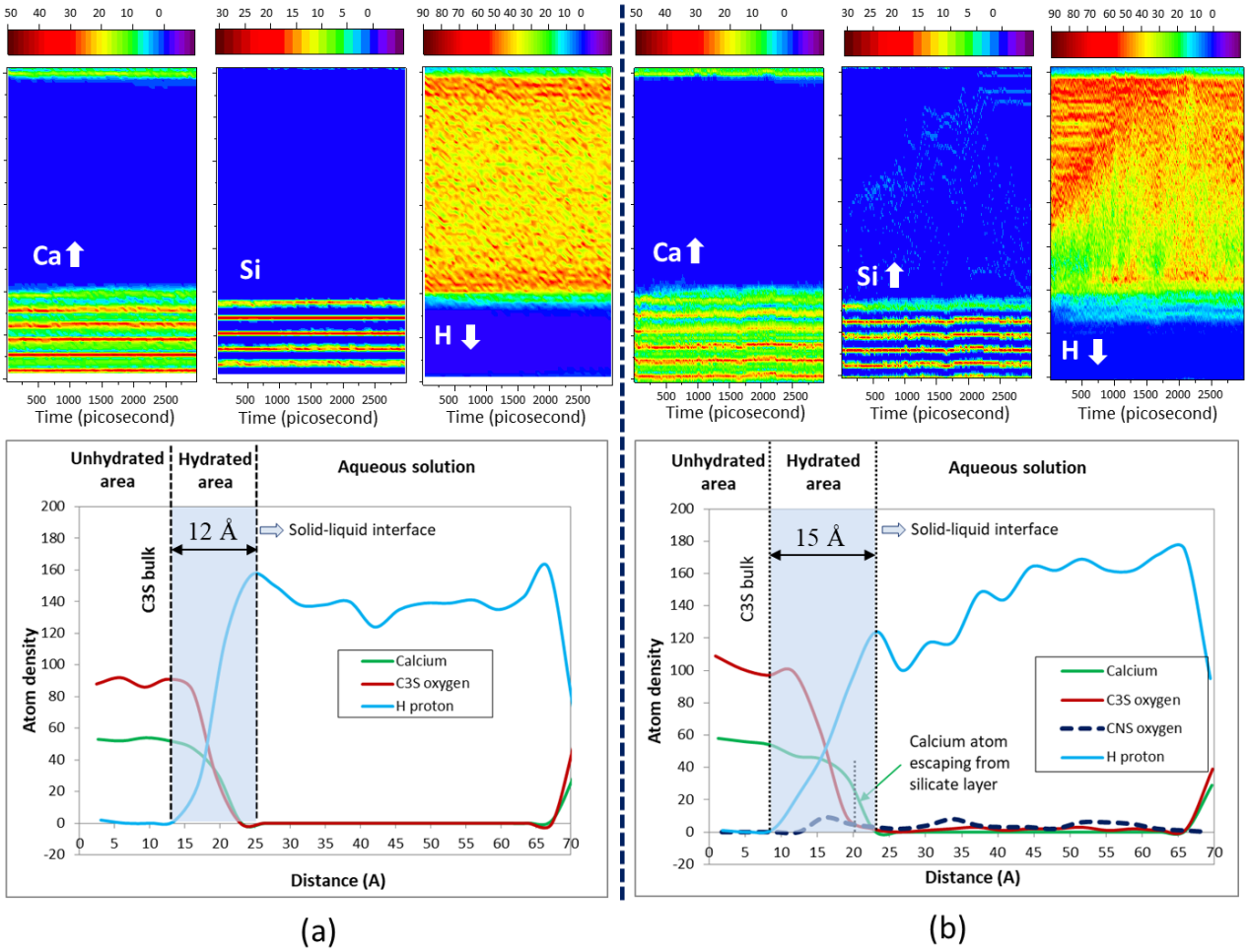


**Fig.13** TRDP and eventual atom intensity profile by the end of simulation for given Ca, O, H species for molecular systems (a) without CNS, and (b) with CNS inclusion.

With further reaction, the evolved molecular structure of the $C_3S$/water/CNS chains system shows that some silicon and oxygen atoms are released from the $C_3S$ bulk matrix and diffused into the solution, causing a more defective surface with an etch pit activation mechanism[27]. The silicate monomers start to polymerize in the $C_3S$/water/CNS chains system, resulting in formation of paired silicate tetrahedral (dimer) (see Fig.9u) or silicate trimer anions around the etch pit area near the surface, following the reaction below[75]:

$$SiO_4^{4-} + HSiO_4^{3-} \Leftrightarrow [\equiv O_3Si\text{-}O\text{-}SiO_3 \equiv]^{6-} + HO^- \tag{7}$$

$$[\equiv O_3Si\text{-}O\text{-}SiO_3 \equiv]^{6-} + HSiO_4^{3-} + H_2O + 2H^+ \Leftrightarrow \left[\equiv O_3Si\text{-}O\text{-}\underset{\displaystyle O}{\overset{\displaystyle O}{\overset{|}{\underset{|}{Si}}}}\text{-}O\text{-}Si(OH)_3\right]^{5-} + 2OH^- \tag{8}$$

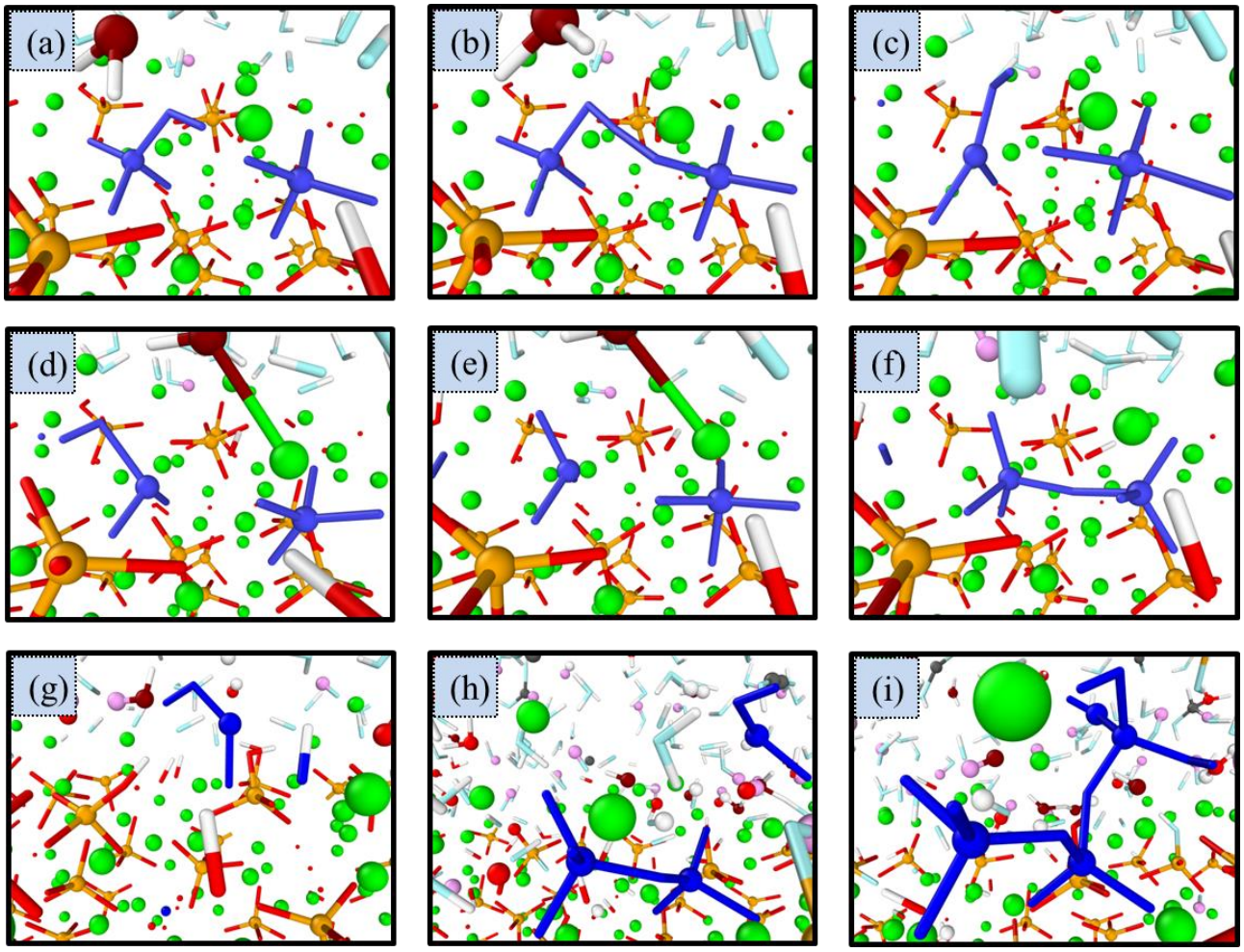


**Fig.14** Snapshot of silicate oligomerization pathway: It starts with two independent silicate tetrahedral monomers(a), the hydrogen atom may be connected by the neighboring oxygen atoms during relaxation(b), the electronegativity is reduced for the hydrogen orthosilicate ion ($HO_4Si^{3-}$), leading to the dissolution of this unstable silicic acid to metasilicate ion($HO_3Si^{-}$), where the tetrahedral oxygen atoms are strongly attracted by the adjacent calcium cation and migrated into the interstitial site at the defective region(c), the hydrogen is then pointing towards the diffused dangling oxygen due to the higher reactivity nature of Od site(d), followed by proton jumping in formation of hydroxyl group (e), with eventual oligomerization into paired silicate tetrahedra(f). Dissolution of hydrogen orthosilicate ion ($HO_4Si^{3-}$) again with the tetrahedral oxygen diffused into the interstitial site and form hydroxyl group with penetrated proton (g). Diffusion of the Si(OH)O cation to the adjacent silicate dimer(h). Oligomerization of silicate trimer (i). The silicate tetrahedral is marked as blue.

Figure14 shows one possible mechanism for the silicate oligomerization during hydration as obtained from the MD simulations. The atoms and bonds are highlighted in blue for better illustration. As previously mentioned, some silicate tetrahedra at the $C_3S$ substrate surface will dissolve and diffuse into the aqueous solution due to the attraction from the CNS material. The diffused silicate atoms in the aqueous solution are also linked to the hydroxide ions to form orthosilicate $Si(OH)_4$. It is noticed that the reaction is reversible for the oligomerization of silicate monomers, i.e.

$$Si(OH)_4 + Si(OH)_4 \Leftrightarrow (HO)_3SiOSi(OH)_3 + H_2O \quad (9)$$

The condensed water molecules can be dissociated once again for further proton hopping and hydration. The polymerization of $Q^1$ and $Q^2$ species ($Q^n$ refers to silicon atoms that are covalently bonded via bridging oxygen atoms to other n silicon atoms with $0<n<4$) of silicates with formation of short chains is an explicit signal of C-S-H precipitation in the vicinity of surface. However, we have to omit the simulation of the growth of C-S-H that is usually occurring at a much longer time scales, as it can be very challenging to simulate the growth of C-S-H using the reactive force field due to high computational cost. It is worth noting that silicic polymerization and nucleation of C-S-H ellipsoid particle has been successfully achieved by a sol-gel MD simulation via an empirical Feuston–Garofalini (FG) potential[76,77]. Based on the current study, we believe that further hydration events (such as deposition of oligomeric C-S-H nanoscale colloidal cluster) for $C_3S$ interacting with CNS at longer time scales can be described by using a more efficient empirical force field or a coarse-grained model.

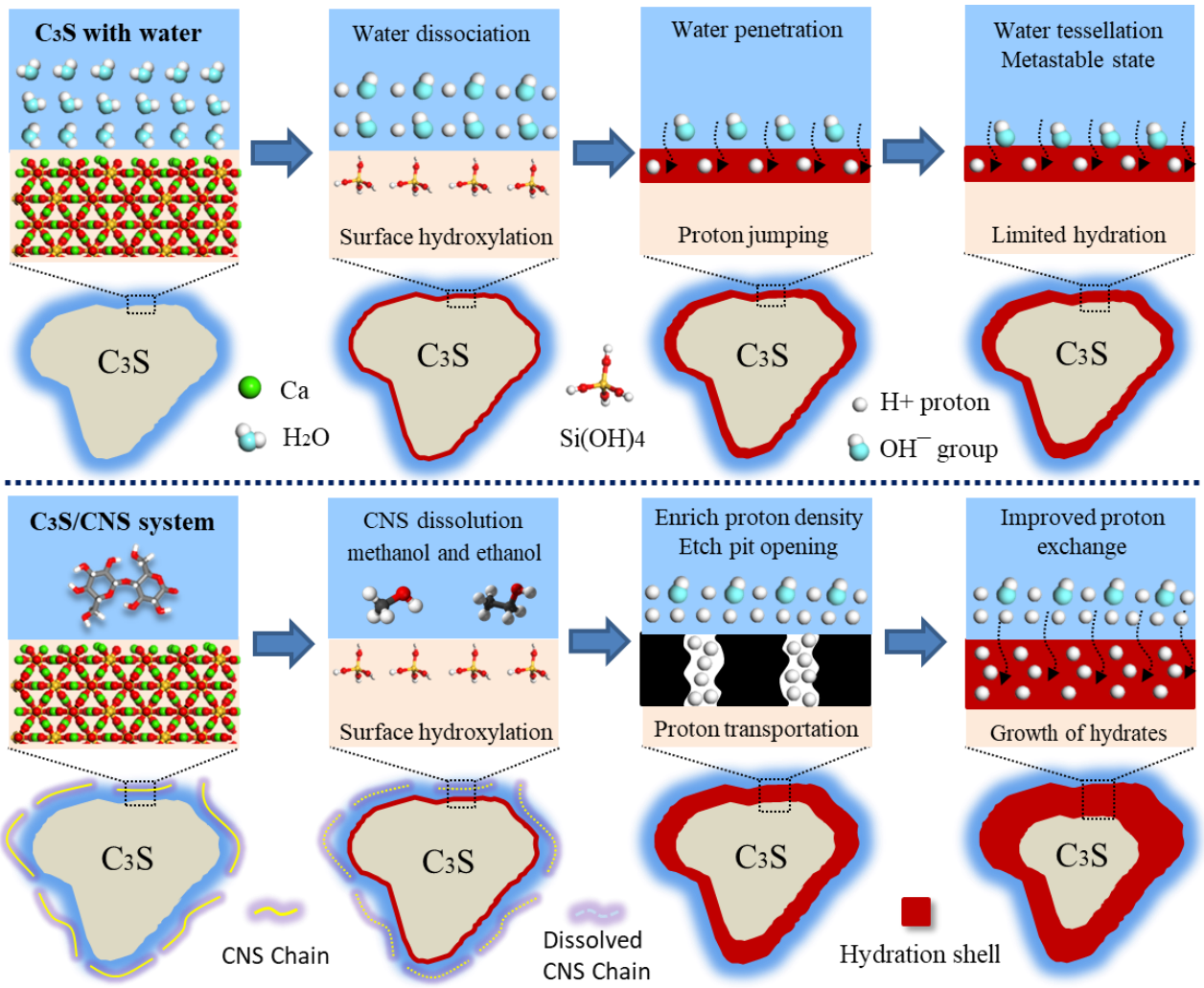

Fig.15 Schematic diagram the improved hydration after inclusion of CNS chain

The MD-DFT simulations conducted in this study uncovered new mechanisms underpinning the improved hydration of $C_3S$, the main phase of OPC. In summary that the presence of CNS chains in the vicinity of the cement particle tend to dissolve and promote the water dynamics. This bursts the energetic barrier for further $C_3S$ hydration, as schematically shown in Fig.15. As such, the CNS is acting like a reservoir transporting the water molecules from the aqueous solution to the inside of substrate species, which increases the thickness of the hydration shell of cement particles.

### 3.4 Experimental results

*3.4.1 TGA/DTG/DSC results*

The following experimental characterizations were carried out to further understand the effect of various CNS concentrations on the hydration of cement pastes. Fig.16a shows the TGA results for the cementitious composites containing different CNSs with weight percentage ranging from 0.1 wt% to 0.4 wt%. The results indicate that the C-S-H and aluminate phase (e.g. ettringite) gradually lose bound water in the temperature range between 140 and 300 °C. The dehydroxylation of $Ca(OH)_2$ happens between 420 and 480 °C and the calcium carbonate ($CaCO_3$) decarbonation process occurs between 600 and 780 °C. The amount of mass loss increases with an increase in the concentration of CNSs. The final weight of the controlled specimen is fixed at 85.85%, while the cementitious nanocomposites with 0.1, 0.2 and 0.4 wt% CNSs are burned 0.16, 0.44 and 0.76% more, respectively in comparison to the controlled specimen.

The abovementioned thermogravimetric mass loss is directly related to the degree of hydration (DOH). According to the hydration empirical formula of T.C Powers[2], the content of bound water can be calculated from the weight difference before and after the cement thermogravimetric experiment. DOH is then calculated by dividing the mass of chemically bound water (CBW) to the remaining weight of the experiment and 0.23, given as[78]:

$$\mathrm{DOH(TGA)} = \frac{m(\mathrm{CBW})}{m(\mathrm{remain})} / 0.23 \tag{10}$$

Fig.16b shows the 28-d DOH and the percentage of portlandite for the cementitious nanocomposite with increasing CNS concentrations. It can be seen from the blue line that the DOH increases as the amount of CNS concentration increases. In comparison to the plain specimen, the DOH for the nanocomposite containing 0.1, 0.2 and 0.4wt% CNS is increased by 1.35%, 3.71% and 6.30%,

respectively. The phenomenon of the improved DOH is consisting with the finding from the MD simulations that the CNS enables the water molecules to penetrate deeper into the interior microstructure of the clinker.

Fig.16c illustrates the Derivative Thermogravimetry (DTG) curves after 28 days of curing. The curves show that the nanocomposites with or without CNSs decompose and degrade in the same temperature range. The peaks in the DTG chart shows that the specific C-S-H, $Ca(OH)_2$ and $CaCO_3$ phases decompose quickly in the temperature ranges 140-300℃, 420-480℃ and 600-780℃. In comparison to the controlled specimen, the addition of CNSs increases the peaks, implying that there are more hydration products decomposed at the same temperature.

Figures16d-e show the DSC thermogram of CNS reinforced cementitious nanocomposite along with the enthalpy of fusion of portlandite crystals in the temperature range 20 - 900 °C. By calculating the relationship between heat flow and time, the heat absorbed/released by the crystal decomposition of the cementitious composite can be obtained within a temperature range (see Fig.16d). As shown in Fig.16d, the first endothermic progress occurs between 140 and 400 °C. This process occurs due to the loss of chemically bound water in the C-S-H crystal and aluminate phase (e.g. ettringite) during their heat absorption. The second endothermic peak occurs between 420 to 480 °C, corresponding to the phenomenon of the microcrystalline $Ca(OH)_2$ containing the embedded CNSs decomposition [79]. As a result, $Ca(OH)_2$ is thermally decomposed together with the pyrolysis of the attached CNS cellulose body. The following endothermic peak is located between 600 and 800 °C, where the decomposition of $CaCO_3$ is dominant.

The DSC endothermic peak position in Fig.16d matches the DTG degradation position in Fig.16c. Taking the pyrolysis process of Portlandite as an example, the thermogravimetric loss in the temperature range 420-480°C is considered as the dihydroxylation of $Ca(OH)_2$. Once again, it is noted from the black line in Fig.16b that the content of Portlandite is increased by 4.16%， 9.49% and 19.73% at CNS concentrations between 0 and 0.4wt%. These results are similar to the enthalpy of fusion for the cementitious composite with CNSs which are increased by 3.73%， 8.52% and 16.54% respectively as shown in Fig.16e. The experiment result again confirm that CNS accelerates the DOH, thus generating denser hydration products.

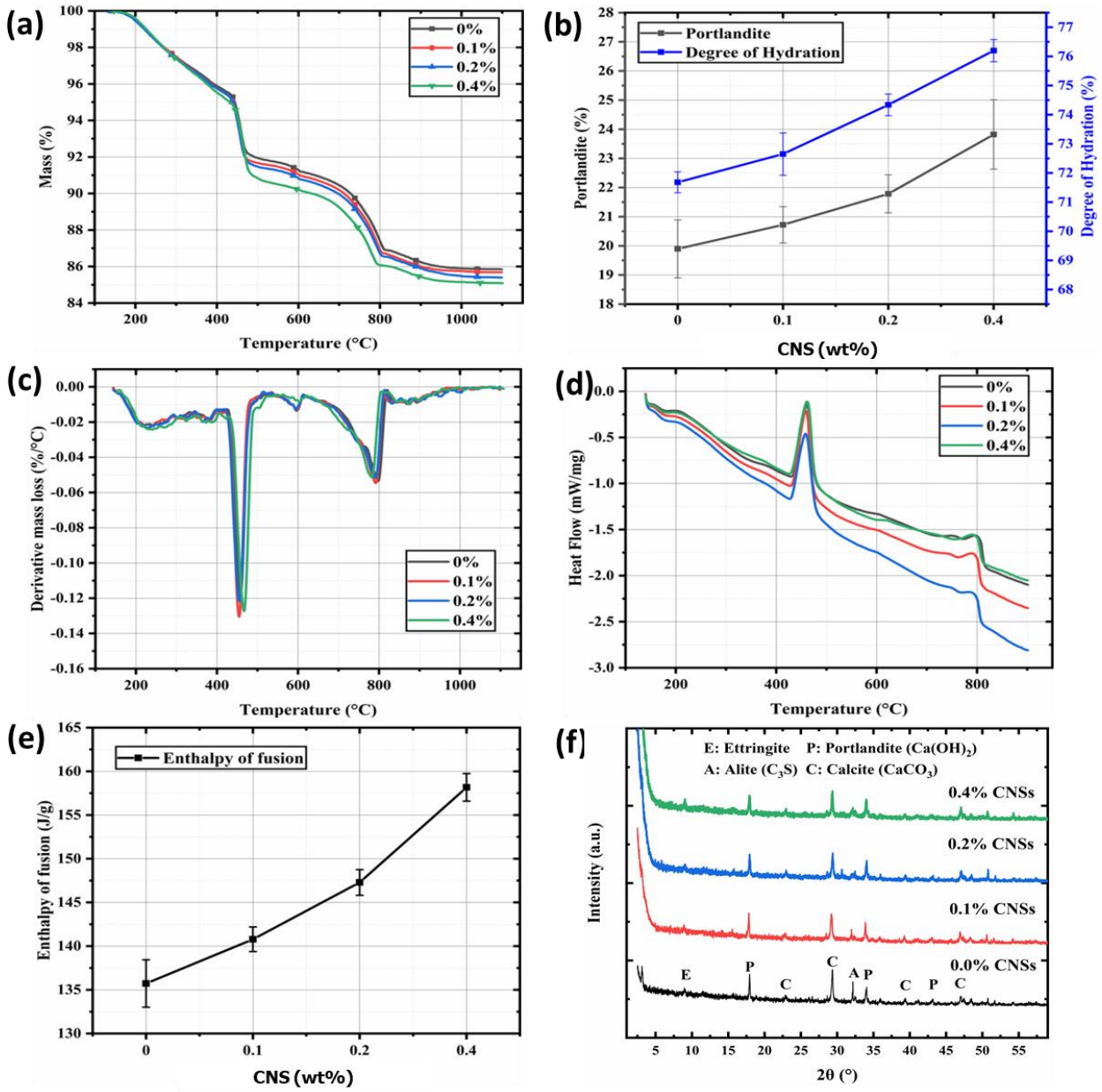


**Fig.16** experimental results of hydration reactivity of the cementitious nanocomposite with CNS concentrations from 0 to 0.4wt%.(a) 28-d TGA results of the cementitious nanocomposite.(b) 28-d DOH and percentage of portlandite.(c) 28-d DTG results.(d) 28-days DSC results.(e) 28-d Portlandite enthalpy of fusion. (f) XRD patterns.

*3.4.2 XRD/SEM/TEM results*

Fig.16f shows the 28-d XRD patterns of the cementitious composites with CNSs concentrations of 0.00, 0.10, 0.20 and 0.40wt%. Through the analysis of CrysAlisPro software phase fitting and Rietveld refinement techniques, all the samples show similar hydration phases including ettringite (AFt), calcium hydroxide ($Ca(OH)_2$), unhydrated tricalcium silicate ($C_3S$) and calcium carbonate ($CaCO_3$). The results clearly indicate that the incorporation of CNS does not change the type and structure of the hydration product. From fig.16f we can see that the Ettringite intensity peaks at 9°

and 15° are stronger in the CNS cement composite than those in the plain cement composite. Furthermore, intensity of $Ca(OH)_2$ at 17.5° in the CSN cement composite is similar to that in the plain cement composite. However, the CNS cement specimen shows a significant increase in $Ca(OH)_2$ at 34°. We quantitatively identified that as the CNS concentration increases, ettringite, $Ca(OH)_2$ and other crystals intensity continue to increase, whereas the intensity of unhydrated phases tricalcium silicate and calcium carbonate decrease (e.g. the intensity peak of $C_3S$ phase decreases). However, due to the nature of C-S-H gel semi-crystalline, it is difficult to analyze its crystallization by XRD. But from the combined XRD, TGA, DTG and DSC results, it is reasonable to state that the addition of CNSs amplify the growth of C-S-H. The characteristic peaks of CNS are not detected by XRD, because some of CNSs are dissolved during their interaction with the cement particles and some are embedded in the hydrate phases. This support the findings of the MD simulations. The MD simulations show that the acidic hydroxyl (-OH) / hydroxymethyl ($-CH_2$-OH) functional groups on the surface of CNS are partially weakened/dissolved in the cement alkaline environment (pH = 11.7) at the CNS/cement interface and react with the surface calcium and oxygen atoms. This series of interaction facilitate the Ca $(OH)_2$ precipitation and the C-S-H formation.

Figures 17a-b shows typical 28-day SEM images of the cementitious composites. Figure 17b indicates that the addition of 0.40 wt% NCS can tolerate the crystallization and the morphology of hydration products of the cement paste at 28 days. The microstructure of the cement paste without CNS (Fig.17a) mainly contains partially unhydrated cement particles, $Ca(OH)_2$, a small amount of C-S-H and microcracks. This could be attributed to lower DOH. In contrast, the microstructure of the nanocomposite containing 0.40-wt% CNS (Fig.17b) mainly includes CNSs that are embedded into the C-S-H gel and the calcium hydroxide needles. The microstructure of the nanocomposite containing CNS showed a compact microstructure with condensed hydration products and without micro-cracks. This can be attributed to the fact that the CNS sheets are encapsulated by the dense C-S-H gels during the hydration, resulting in intercalated nanocomposites.

Figures 17c-d show the 28-day microstructure TEM micrographs of the cementitious composites. Figure.17c shows that the microstructure of the plain paste is composed of lower contents of C-S-H and Ca $(OH)_2$ crystals. Fig.17d shows the microstructure of the cement paste with 0.40% wt CNS where fabric-like CNSs crystals are highly transparent. The combination of CNSs and hydration products enhances the aggregation of matrix C-S-H and $Ca(OH)_2$ crystals to form a denser

microstructure. The Fig.17e-f show the 28-day EDS of plain and CSNs reinforced cement pastes. The EDS results indicate that the oxygen spectroscopy of CNS reinforced cementitious composite is denser than that of the plain cement paste. A small amount of partial agglomeration can be observed based on the oxygen spectrum for the CNS specimen, which further confirms the generation of hydration products. The incorporation of CNS contributed to the formation and agglomeration of cementitious composites C-S-H and $Ca(OH)_2$ hydration products. The TEM and EDS images confirm the findings from TGA, XRD and SEM results that the CNSs facilitate the hydration of the cement thereby increasing the content of C-S-H and $Ca(OH)_2$ in the cementitious composite. It is north noting that the CNS cannot be seen in the SEM and TEM images. Again, the stacked CNSs can be partially dissolved as a result of interaction with $C_3S$. This again supports the dissolution mechanism of CNS uncovered by the MD simulations. Furthermore, the remaining stacked CNSs are fully embedded in the hydrate phases thus cannot be detected by SEM and TEM.

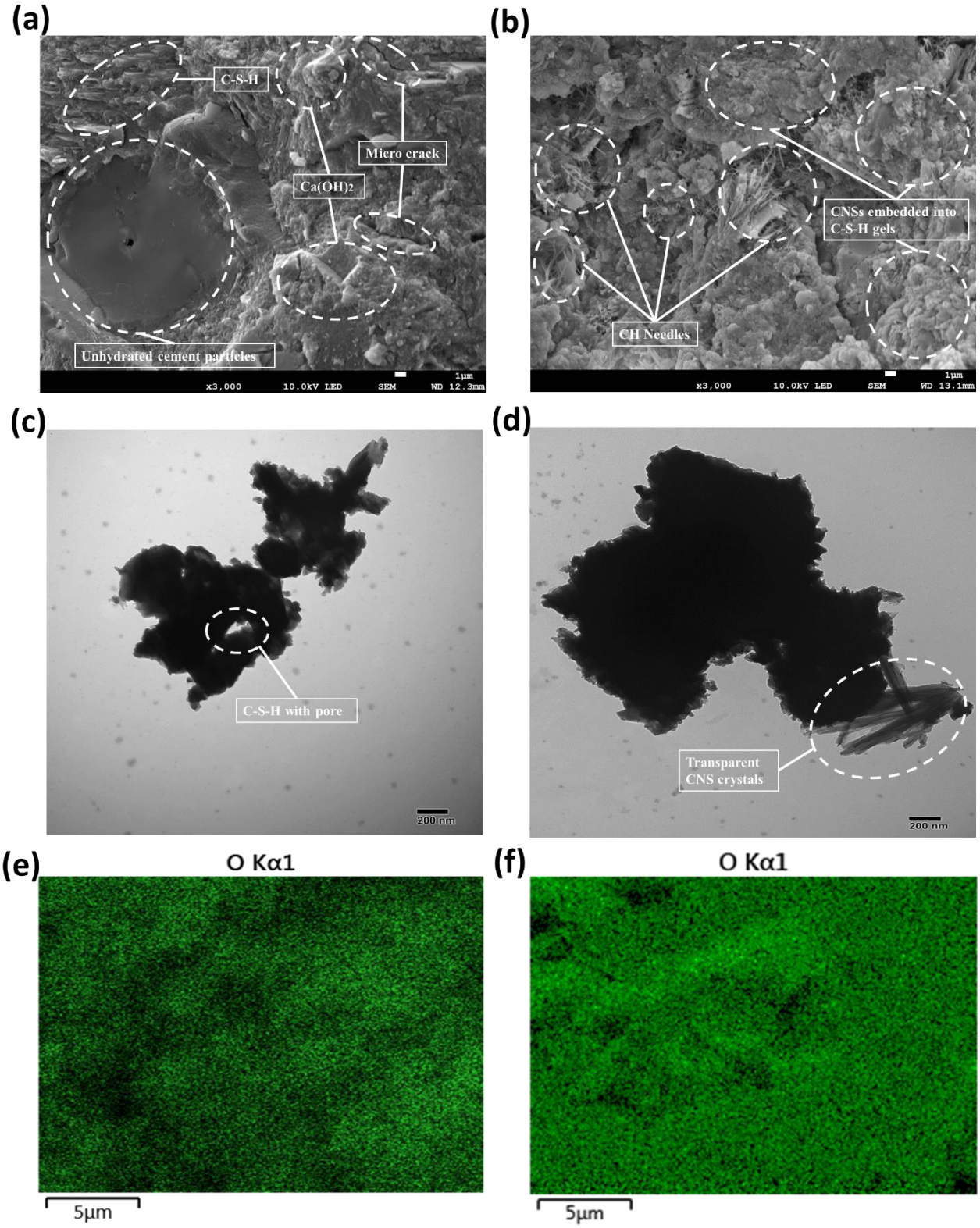


**Fig.17** SEM and (TEM) images of CNSs cementitious composite: (a) SEM of cement paste without CNS, (b) SEM of nanocomposite with 0.4wt% CNS (c) TEM of cement paste without CNS, (d) TEM of nanocomposite with 0.4wt% CNS, (e) EDS of cement paste without CNS, (f) EDS of nanocomposite with 0.4wt% CNS.

## 4 Conclusions and Future Work

Using a combination of DFT-MD simulations and experimental characterization, we have demonstrated that the addition of 2D CNS material can remarkably improve the growth of the hydrate products of OPC. The following conclusions can be drawn from this study:

- The DFT-MD simulations show that during the hydration process, the CNS chains in contact with the $C_3S$ surface dissolve, leading to the formation of many organic chemical compounds. These chemical compounds mitigate the water tessellation effect at the CNS/$C_3S$ interface. This increases the dynamics of water molecules in the aqueous solution and promote higher OPC hydration depth, thus more hydrate products are developed. The increased hydration depth is also due to the enriched H protons and hydroxide ions decomposed from CNS that is seeding for the proton exchange during hydration.
- During hydration, the $C_3S$ suffers simultaneously nucleophilic and electrophilic attacks from both the CNS and the water molecules. Since the $C_3S$ calcium atom is an electron acceptor, the anions from the water oxygen, CNS backbone oxygen, and the deprotonated CNS functional group oxygen are attracted to $C_3S$. Because of this, the $C_3S$ oxygen atoms act as electron donors that accept $H^+$ protons from water and CNS functional groups, resulting in higher growth of hydration products.
- The experimental results support the key findings from the DFT-MD investigation. The experimental research shows that the addition of CNS increases the degree of hydration of the cement paste. As a result, the growth of the hydrate phases is amplified, leading to the formation of denser C-S-H and $Ca(OH)_2$ products in the cement paste.
- The experimental and DFT-MD simulation results confirm the dissolution of CNS layers that are in the vicinity of $C_3S$ as a result of their interaction with the OPC particles. The CNS layers that are in the distance to the OPC particles remained intact and embedded in the hydrate phases.
- Future work is needed to extend the DFT-MD simulations to the "as produced" CNS with multiple layers to better understand the interaction of these layers with $C_3S$ and predict the resulting degree of hydration. The DFT-MD simulations also need to be carried out over longer time scale to link to the interaction of $C_3S$ with CNS to the growth of C-S-H. Further experimental characterization is needed to characterize the effect of CNS on the hydration depth at multiple length scales using high-throughput analytical characterization tools.

- The research presented herein provides a road map for the development of high performance and low-carbon footprint construction materials through controlled hydration kinetics using green and renewable 2D nanomaterials derived from waste.

## Acknowledgement

This research work is financially supported by the European Commission Horizon 2020 Marie Sklodowska-Curie Research Grant (B-SMART 799658).

Reference


[1] J.W. Bullard, H.M. Jennings, R.A. Livingston, A. Nonat, G.W. Scherer, J.S. Schweitzer, K.L. Scrivener, J.J. Thomas, Mechanisms of cement hydration, Cem. Concr. Res. 41 (2011) 1208–1223. https://doi.org/10.1016/j.cemconres.2010.09.011.

[2] H.F.W. Taylor, Cement chemistry, Thomas Telford, 1997.

[3] K. Scrivener, A. Ouzia, P. Juilland, A.K. Mohamed, Advances in understanding cement hydration mechanisms, Cem. Concr. Res. 124 (2019) 105823.

[4] P.J.M. Monteiro, S.A. Miller, A. Horvath, Towards sustainable concrete, Nat. Mater. 16 (2017) 698–699.

[5] F. Lavergne, R. Belhadi, J. Carriat, A. Ben Fraj, Effect of nano-silica particles on the hydration, the rheology and the strength development of a blended cement paste, Cem. Concr. Compos. 95 (2019) 42–55.

[6] J. Zhou, K. Zheng, Z. Liu, F. He, Chemical effect of nano-alumina on early-age hydration of Portland cement, Cem. Concr. Res. 116 (2019) 159–167.

[7] J. Chen, S. Kou, C. Poon, Hydration and properties of nano-TiO2 blended cement composites, Cem. Concr. Compos. 34 (2012) 642–649.

[8] R. Kalpokaitė-Dičkuvienė, A. Baltušnikas, R. Levinskas, J. Čėsnienė, Incinerator residual ash–metakaolin blended cements: effect on cement hydration and properties, Constr. Build. Mater. 206 (2019) 297–306.

[9] M. Heikal, N.S. Ibrahim, Hydration, microstructure and phase composition of composite cements containing nano-clay, Constr. Build. Mater. 112 (2016) 19–27.

[10] T. Matschei, B. Lothenbach, F.P. Glasser, The role of calcium carbonate in cement hydration, Cem. Concr. Res. 37 (2007) 551–558.

[11] M.S.M. Norhasri, M.S. Hamidah, A.M. Fadzil, Applications of using nano material in concrete: A review, Constr. Build. Mater. 133 (2017) 91–97.

[12] M. Schneider, The cement industry on the way to a low-carbon future, Cem. Concr. Res. 124 (2019) 105792. https://doi.org/10.1016/j.cemconres.2019.105792.

[13] J. Skibsted, R. Snellings, Reactivity of supplementary cementitious materials (SCMs) in cement blends, Cem. Concr. Res. 124 (2019) 105799.

[14] M. Eftekhari, S. Mohammadi, Molecular dynamics simulation of the nonlinear behavior of the CNT-reinforced calcium silicate hydrate (C–S–H) composite, Compos. Part A Appl. Sci. Manuf. 82 (2016) 78–87.

[15] X. Zhu, Y. Gao, Z. Dai, D.J. Corr, S.P. Shah, Effect of interfacial transition zone on the Young's modulus of carbon nanofiber reinforced cement concrete, Cem. Concr. Res. 107 (2018) 49–63.

[16] H. Yang, H. Cui, W. Tang, Z. Li, N. Han, F. Xing, A critical review on research progress of graphene/cement based composites, Compos. Part A Appl. Sci. Manuf. 102 (2017) 273–296.

[17] D. Hou, Z. Lu, X. Li, H. Ma, Z. Li, Reactive molecular dynamics and experimental study of graphene-cement composites: Structure, dynamics and reinforcement mechanisms, Carbon N. Y. 115 (2017) 188–208.

[18] C. Zhou, F. Li, J. Hu, M. Ren, J. Wei, Q. Yu, Enhanced mechanical properties of cement paste by hybrid graphene oxide/carbon nanotubes, Constr. Build. Mater. 134 (2017) 336–345.

[19] D. Fan, L. Lue, S. Yang, Molecular dynamics study of interfacial stress transfer in graphene-oxide cementitious composites, Comput. Mater. Sci. 139 (2017) 56–64.

[20] L. Zhao, X. Guo, L. Song, Y. Song, G. Dai, J. Liu, An intensive review on the role of graphene oxide in cement-based materials, Constr. Build. Mater. 241 (2020) 117939.

[21] M. Birenboim, R. Nadiv, A. Alatawna, M. Buzaglo, G. Schahar, J. Lee, G. Kim, A. Peled, O. Regev, Reinforcement and workability aspects of graphene-oxide-reinforced cement nanocomposites, Compos. Part B Eng. 161 (2019) 68–76.

[22] Y. Chi, B. Huang, M. Saafi, J. Ye, C. Lambert, Carrot-based covalently bonded saccharides as a new 2D material for healing defective calcium-silicate-hydrate in cement: Integrating atomistic computational simulation with experimental studies, Compos. Part B Eng. 199 (2020) 108235.

[23] D. Hepworth, E. Whale, Cellulose platelet compositions, methods of preparing cellulose platelet compositions and products comprising same, US 9,834,664 B2, 2017.

[24] D. Ru, C. Zhu, S. Dong, J. Zhao, Wrinkling behavior of graphene on substrates with different surface morphologies, Mech. Mater. 137 (2019) 103144.

[25] Y. Cao, N. Tian, D. Bahr, P.D. Zavattieri, J. Youngblood, R.J. Moon, J. Weiss, The influence of cellulose nanocrystals on the microstructure of cement paste, Cem. Concr. Compos. 74 (2016) 164–173.

[26] D. Lau, W. Jian, Z. Yu, D. Hui, Nano-engineering of construction materials using molecular dynamics simulations: Prospects and challenges, Compos. Part B Eng. 143 (2018) 282–291. https://doi.org/10.1016/j.compositesb.2018.01.014.

[27] P. Juilland, E. Gallucci, R. Flatt, K. Scrivener, Dissolution theory applied to the induction period in alite hydration, Cem. Concr. Res. 40 (2010) 831–844.

[28] M.-N. De Noirfontaine, F. Dunstetter, M. Courtial, G. Gasecki, M. Signes-Frehel, Polymorphism of tricalcium silicate, the major compound of Portland cement clinker: 2. Modelling alite for Rietveld analysis, an industrial challenge, Cem. Concr. Res. 36 (2006) 54–64.

[29] W.G. Mumme, Crystal structure of tricalcium silicate from a Portland cement clinker and its application to quantitative XRD analysis, Neues Jahrb. Für Mineral. 1995 (1995) 146–160.

[30] R.J. Moon, A. Martini, J. Nairn, J. Simonsen, J. Youngblood, Cellulose nanomaterials review: structure, properties and nanocomposites, Chem. Soc. Rev. 40 (2011) 3941–3994.

[31] Y. Horikawa, J. Sugiyama, Localization of crystalline allomorphs in cellulose microfibril, Biomacromolecules. 10 (2009) 2235–2239.

[32] Y. Nishiyama, P. Langan, H. Chanzy, Crystal structure and hydrogen-bonding system in cellulose Iβ from synchrotron X-ray and neutron fiber diffraction, J. Am. Chem. Soc. 124 (2002) 9074–9082.

[33] Y. Nishiyama, J. Sugiyama, H. Chanzy, P. Langan, Crystal Structure and Hydrogen Bonding System in Cellulose Iα from Synchrotron X-ray and Neutron Fiber Diffraction, J. Am. Chem. Soc. 125 (2003) 14300–14306. https://doi.org/10.1021/ja037055w.

[34] H. Heinz, T.-J. Lin, R. Kishore Mishra, F.S. Emami, Thermodynamically consistent force fields for the assembly of inorganic, organic, and biological nanostructures: the INTERFACE force field, Langmuir. 29 (2013) 1754–1765.

[35] B. Delley, From molecules to solids with the DMol 3 approach, J. Chem. Phys. 113 (2000) 7756–7764.

[36] J.P. Perdew, K. Burke, M. Ernzerhof, Generalized gradient approximation made simple, Phys. Rev. Lett. 77 (1996) 3865.

[37] A.C.T. Van Duin, A. Strachan, S. Stewman, Q. Zhang, X. Xu, W.A. Goddard, ReaxFFSiO reactive force field for silicon and silicon oxide systems, J. Phys. Chem. A. 107 (2003) 3803–3811.

[38] A.C.T. Van Duin, S. Dasgupta, F. Lorant, W.A. Goddard, ReaxFF: a reactive force field for hydrocarbons, J. Phys. Chem. A. 105 (2001) 9396–9409.
[39] S. Plimpton, Fast parallel algorithms for short-range molecular dynamics, J. Comput. Phys. 117 (1995) 1–19.
[40] M.R. Sadat, K. Muralidharan, L. Zhang, Reactive molecular dynamics simulation of the mechanical behavior of sodium aluminosilicate geopolymer and calcium silicate hydrate composites, Comput. Mater. Sci. 150 (2018) 500–509.
[41] D. Fan, S. Yang, Mechanical properties of CSH globules and interfaces by molecular dynamics simulation, Constr. Build. Mater. 176 (2018) 573–582.
[42] J. Jiang, Y. Yan, D. Hou, J. Yu, Understanding the deformation mechanism and mechanical characteristics of cementitious mineral analogues from first principles and reactive force field molecular dynamics, Phys. Chem. Chem. Phys. 20 (2018) 13920–13933.
[43] D. Hou, J. Yu, Z. Jin, A. Hanif, Molecular dynamics study on calcium silicate hydrate subjected to tension loading and water attack: Structural evolution, dynamics degradation and reactivity mechanism, Phys. Chem. Chem. Phys. 20 (2018) 11130–11144. https://doi.org/10.1039/c7cp08634b.
[44] Y. Zhou, D. Hou, G. Geng, P. Feng, J. Yu, J. Jiang, Insights into the interfacial strengthening mechanisms of calcium-silicate-hydrate/polymer nanocomposites, Phys. Chem. Chem. Phys. 20 (2018) 8247–8266.
[45] Y. Zhou, C.A. Orozco, E. Duque-Redondo, H. Manzano, G. Geng, P. Feng, P.J.M. Monteiro, C. Miao, Modification of poly (ethylene glycol) on the microstructure and mechanical properties of calcium silicate hydrates, Cem. Concr. Res. 115 (2019) 20–30.
[46] J. Yang, D. Hou, Q. Ding, Structure, dynamics, and mechanical properties of cross-linked calcium aluminosilicate hydrate: A molecular dynamics study, ACS Sustain. Chem. Eng. 6 (2018) 9403–9417.
[47] D. Hou, J. Yu, P. Wang, Molecular dynamics modeling of the structure, dynamics, energetics and mechanical properties of cement-polymer nanocomposite, Compos. Part B Eng. 162 (2019) 433–444.
[48] Y. Zhang, X. Lu, D. Song, S. Liu, The adsorption behavior of a single and multi- water molecules on tricalcium silicate (111) surface from DFT calculations, J. Am. Ceram. Soc. 102 (2019) 2075–2083.
[49] H. Manzano, E. Durgun, I. López-Arbeloa, J.C. Grossman, Insight on tricalcium silicate hydration and dissolution mechanism from molecular simulations, ACS Appl. Mater. Interfaces. 7 (2015) 14726–14733.
[50] Q. Wang, H. Manzano, Y. Guo, I. Lopez-Arbeloa, X. Shen, Hydration mechanism of reactive and passive dicalcium silicate polymorphs from molecular simulations, J. Phys. Chem. C. 119 (2015) 19869–19875.
[51] H. Manzano, R.J.M. Pellenq, F.-J. Ulm, M.J. Buehler, A.C.T. Van Duin, Hydration of calcium oxide surface predicted by reactive force field molecular dynamics, Langmuir. 28 (2012) 4187–4197.
[52] H. Kono, T. Erata, M. Takai, Complete assignment of the CP/MAS 13C NMR spectrum of cellulose IIII, Macromolecules. 36 (2003) 3589–3592.
[53] H. Kono, S. Yunoki, T. Shikano, M. Fujiwara, T. Erata, M. Takai, CP/MAS 13C NMR study of cellulose and cellulose derivatives. 1. Complete assignment of the CP/MAS 13C NMR spectrum of the native cellulose, J. Am. Chem. Soc. 124 (2002) 7506–7511.

[54] T. Bucko, D. Tunega, J.G. Ángyán, J. Hafner, Ab initio study of structure and interconversion of native cellulose phases, J. Phys. Chem. A. 115 (2011) 10097–10105.
[55] Y. Li, M. Lin, J.W. Davenport, Ab initio studies of cellulose I: crystal structure, intermolecular forces, and interactions with water, J. Phys. Chem. C. 115 (2011) 11533–11539.
[56] K. Saritas, C. Ataca, J.C. Grossman, Predicting electronic structure in tricalcium silicate phases with impurities using first-principles, J. Phys. Chem. C. 119 (2015) 5074–5079.
[57] E. Durgun, H. Manzano, R.J.M. Pellenq, J.C. Grossman, Understanding and controlling the reactivity of the calcium silicate phases from first principles, Chem. Mater. 24 (2012) 1262–1267.
[58] R.G. Parr, W. Yang, Density functional approach to the frontier-electron theory of chemical reactivity, J. Am. Chem. Soc. 106 (1984) 4049–4050.
[59] H. Manzano, E. Durgun, M.J. Abdolhosseine Qomi, F.-J. Ulm, R.J.M. Pellenq, J.C. Grossman, Impact of chemical impurities on the crystalline cement clinker phases determined by atomistic simulations, Cryst. Growth Des. 11 (2011) 2964–2972.
[60] H. Manzano, J.S. Dolado, A. Ayuela, Structural, mechanical, and reactivity properties of tricalcium aluminate using first- principles calculations, J. Am. Ceram. Soc. 92 (2009) 897–902.
[61] Q. Wang, X. Gu, H. Zhou, X. Chen, X. Shen, Cation substitution induced reactivity variation on the tricalcium silicate polymorphs determined from first-principles calculations, Constr. Build. Mater. 216 (2019) 239–248.
[62] Q. Wang, F. Li, X. Shen, W. Shi, X. Li, Y. Guo, S. Xiong, Q. Zhu, Relation between reactivity and electronic structure for α′ L-, β-and γ-dicalcium silicate: A first-principles study, Cem. Concr. Res. 57 (2014) 28–32.
[63] C.M. Lee, J.D. Kubicki, B. Fan, L. Zhong, M.C. Jarvis, S.H. Kim, Hydrogen-bonding network and OH stretch vibration of cellulose: comparison of computational modeling with polarized IR and SFG spectra, J. Phys. Chem. B. 119 (2015) 15138–15149.
[64] X. Qian, S.-Y. Ding, M.R. Nimlos, D.K. Johnson, M.E. Himmel, Atomic and electronic structures of molecular crystalline cellulose Iβ: A first-principles investigation, Macromolecules. 38 (2005) 10580–10589.
[65] J. Huang, B. Wang, Y. Yu, L. Valenzano, M. Bauchy, G. Sant, Electronic origin of doping-induced enhancements of reactivity: case study of tricalcium silicate, J. Phys. Chem. C. 119 (2015) 25991–25999.
[66] J. Claverie, F. Bernard, J.M.M. Cordeiro, S. Kamali-Bernard, Water's behaviour on Ca-rich tricalcium silicate surfaces for various degrees of hydration: A molecular dynamics investigation, J. Phys. Chem. Solids. 132 (2019) 48–55.
[67] J. Yang, W. Zhang, D. Hou, G. Zhang, Q. Ding, Structure, dynamics and mechanical properties evolution of calcium silicate hydrate induced by dehydration and dehydroxylation, Constr. Build. Mater. 291 (2021) 123327.
[68] J. Sun, W. Zhang, J. Zhang, D. Hou, Molecular dynamics study the structure, bonding, dynamic and mechanical properties of calcium silicate hydrate with ultra-confined water: Effects of nanopore size, Constr. Build. Mater. 280 (2021) 122477.
[69] F. Bellmann, D. Damidot, B. Möser, J. Skibsted, Improved evidence for the existence of an intermediate phase during hydration of tricalcium silicate, Cem. Concr. Res. 40 (2010) 875–884.
[70] S.A. Rodger, G.W. Groves, N.J. Clayden, C.M. DOBSON, Hydration of tricalcium silicate

followed by 29Si NMR with cross- polarization, J. Am. Ceram. Soc. 71 (1988) 91–96.
[71] J.W. Bullard, A determination of hydration mechanisms for tricalcium silicate using a kinetic cellular automaton model, J. Am. Ceram. Soc. 91 (2008) 2088–2097.
[72] T. Sowoidnich, F. Bellmann, D. Damidot, H. Ludwig, New insights into tricalcium silicate hydration in paste, J. Am. Ceram. Soc. 102 (2019) 2965–2976.
[73] B.A. Fleming, D.A. Crerar, Silicic acid ionization and calculation of silica solubility at elevated temperature and pH application to geothermal fluid processing and reinjection, Geothermics. 11 (1982) 15–29.
[74] J.W. Bullard, J. Hagedorn, M.T. Ley, Q. Hu, W. Griffin, J.E. Terrill, A critical comparison of 3D experiments and simulations of tricalcium silicate hydration, J. Am. Ceram. Soc. 101 (2018) 1453–1470.
[75] E. Gartner, I. Maruyama, J. Chen, A new model for the CSH phase formed during the hydration of Portland cements, Cem. Concr. Res. 97 (2017) 95–106.
[76] L. Zhang, X. Cheng, D. Hou, S. Guo, Hydration for the Alite mineral: Morphology evolution, reaction mechanism and the compositional influences, Constr. Build. Mater. 155 (2017) 413–426.
[77] J.S. Dolado, M. Griebel, J. Hamaekers, F. Heber, The nano-branched structure of cementitious calcium–silicate–hydrate gel, J. Mater. Chem. 21 (2011) 4445–4449.
[78] I. Pane, W. Hansen, Investigation of blended cement hydration by isothermal calorimetry and thermal analysis, Cem. Concr. Res. 35 (2005) 1155–1164.
[79] H. Hasan, B. Huang, M. Saafi, J. Sun, Y. Chi, E. Whale, D. Hepworth, J. Ye, Novel engineered high performance sugar beetroot 2D nanoplatelet-cementitious composites, Constr. Build. Mater. 202 (2019) 546–562.

Manuscript (For revision, upload clean version of revised paper) Click here to view linked References

# 2D bio-based nanomaterial as a green route to amplify the formation of hydrate phases of cement composites: Atomistic simulations and analytical characterization

*Yin Chi,*[a,b*] *Bo Huang,*[b] *Mohamed Saafi,*[b*], *Nigel Fullwood*[c], *Colin Lambert,*[d] *Eric Whale,*[e] *David Hepworth,*[e] *Jianqiao Ye* [b]

[a] School of Civil Engineering, Wuhan University, Wuhan 430072, China
[b] Department of Engineering, Lancaster University, Lancashire, LA1 4YW, UK
[c] Biomedical and Life Sciences, Lancaster University, Lancashire, LA1 4YW, UK
[d] Department of Physics, Lancaster University, Lancashire, LA1 4YB, UK
[e] CelluComp Ltd, Fife, KY3 9DW, UK

**Abstract**

Ordinary Portland cement (OPC) is the binding element in concrete materials and, $CO_2$ emissions associated with its manufacturing and use is about 8% of the world's $CO_2$ emissions. The engineering properties of hardened concrete depend on the amount of the hydrate phases in OPC. If the growth of the hydrate phases could be increased, the performance of concrete would be significantly improved, and the consumption of OPC will be decreased, and its environmental footprint will be reduced. In this paper, we present a new green approach for controlling the growth of the hydrate phases in OPC using bio flakes composed of staked carrot-based two-dimensional (2D) nanosheets (CNSs) synthesized from carrot waste. Density-functional theory and reactive molecular dynamics (DFT-MD) simulations were carried out in conjunction with analytical characterization to examine the interfacial interaction between CNS with tricalcium silicate $Ca_3SiO_5$ ($C_3S$), the main constituent of OPC and understand how they influence the growth of the hydrate phases in OPC. The DFT-MD simulations results show the 2D CNS dissolves due to its interfacial interaction with the highly reactive $C_3S$, leading to a series of fast proton exchange in $C_3S$. This in return accelerates the dissolution rate of $C_3S$ thereby amplifying the growth of the hydrate phases. The DFT-MD simulations also show that the dissolution of the 2D CNS creates new several organic compounds that enhance the mobility and dynamics of protons that further amplify the dissolution rate of $C_3S$. The analytical results from scanning electron microscope (SEM), X-ray diffraction (XRD), transmission electron microscopy (TEM), and thermography analysis (TGA) and differential scanning calorimetry (DSC) show a significant growth of the hydrate products in OPC due to interfacial dissolution of $C_3S$ and some CNS thus, confirming the DFT-MD results. This work demonstrates that the growth of the hydrate products in OPC can be amplified by the addition of green and renewable 2D bio-based nanomaterials. This green approach provides a base for the design and development of low-carbon cementitious materials.

**Keywords:** Density Function Theory (DFT); Reactive Molecular Dynamics Simulation; Cement Hydration; Tricalcium Silicate; Carrot Nanosheet.

*Corresponding authors.
Email addresses: yin.chi@whu.edu.cn (Y. Chi), m.saafi@lancaster.ac.uk (M. Saafi)

## 1. Introduction

Concrete is the most consumed man-made material on the planet. It is used to construct and repair the built environment including buildings, transportation systems and energy infrastructure. Concrete is a heterogeneous composite material, consisting of a mixture of mineral aggregates, water and ordinary Portland cement (OPC), and its performance strongly depends on the amount the products of OPC particles[1]. The amount of the hydrate products of OPC is generally expressed as the amount of cement particles that have hydrated compared to the initial amount of unhydrated cement particles[2], this is usually called the degree of hydration (DOH). The more hydrated cement particles, the higher the amount of the hydrate phases, thus better engineering properties and durability of concrete due to the increased amount of calcium silicate hydration phases (C-S-H), which are the main binding material of concrete.

However, current concrete manufacturing techniques can only achieve the production of concretes with small quantities of hydrate products due to lack of control of the hydration mechanism of OPC which takes place at the nanoscale[3]. As a result, large amounts of OPC are routinely used to produce high performance structural concretes in order to offset the deficiency in the hydration of the cement particles. If the amount of the hydrate products of OPC could be improved, the volume of OPC needed for a given structure would be reduced and the release of $CO_2$ resulting from its production into the atmosphere would be decreased. Cement production accounts for about 8% of global $CO_2$ emissions, a main cause of climate change [4].

One popular approach to improve the engineering properties of concrete is the use of a wide range of nanoparticles including nano silica[5], nano alumina[6], nano titanium oxide[7], nano kaolin[8], nano clay[9] and nano calcium carbonate[10] to increase the amount of the hydrate phases through interfacial chemical reactions in the cement environment[11]. An alternative solution to the production of low carbon-foot print cement is to replace the Portland clinker with supplementary

cementitious materials (SCMs) [12]. Studies have shown that replacement of Portland clinker with SCM can reduce $CO_2$ emissions of up to 40% without significant changes in mechanical properties and durability [13]. Another way to enhance the engineering properties of concrete of is strengthening the hydrate products of OPC with non-reactive carbonaceous nano particles such as carbon nanotubes[14], carbon nanofibers[15], graphene[16,17] and graphene oxide[18–20]. Unfortunately, the large-scale applications of these nanoparticles in building materials have been hampered by the intrinsic difficulty to disperse them in concrete, costs, and potential health and safety effects[21]. As such, there is a need to develop a new generation of high-performance, renewable and sustainable nanomaterials as an alternative to the environmentally harmful existing nanoparticles for creating high performance cementitious composites with lower carbon-foot print.

Recently, we successfully synthesized highly hydrophilic flakes composed of stacked carrot-based two-dimensional (2D) nanosheets (CNSs) produced from carrot waste streams for the development of low-carbon footprint high-performance cementitious composites. Through our preliminary study of the effect of CNS on the performance of cementitious composites, we discovered that: 1) the growth of the hydrate phases of OPC was significantly increased, 2) the CNS layers of bio-flakes in the vicinity of the OPC particles were dissolved and 3) the CNS layers of the bio-flakes distant from the OPC particles were remained intact and were embedded in the highly defective C-S-H gel, forming C-S-H/CNS hybrid composites. Our atomistic simulations showed that one single CNS layer effectively healed this highly defective C-S-H, resulting in high strength and stiffness cementitious composites[22]. The one single layer CNS showed high affinity to C-S-H due to the interfacial Ca-O coordination and H-bond interaction. The functional groups on the surface of the CNS layer cross-linked the neighboring silicate calcium layers and inhibited the water dynamics at the silicate nanochannel, thereby significantly improved the interfacial properties of the C-S-H/CNS hybrid structure[22].

However, the origin of the enhanced growth of the hydrate phases and the dissolution of the CNS layers in the vicinity of the OPC particles during hydration are still not clear. We hypothesize that these two phenomena are the result of the interaction of the CNSs with the OPC particles during hydration. Understanding how the molecular interactions between the CNS and the main calcium silicate phase (tricalcium silicate, $C_3S$) of OPC affect the growth hydration mechanisms of hydrate phases is critical to the design and the development of these novel low-carbon and high-performance

cementitious composites.

Therefore, the aim of this paper is to study the interfacial interaction between CNS and $C_3S$ during hydration using density functional-theory calculations and reactive force field molecular dynamics simulations to gain fundamental understanding of their effects on the growth of the hydrate phases of OPC and uncover the origin of the CNS dissolution. Analytical characterization was also carried out to further ascertain the mechanisms underpinning the growth of the crystal hydrates of OPC and support the key findings of the simulations.

## 2. Material and methods

### 2.1 Preparation of carrot-based cellulose nanosheets (CNSs)

Figure 1 shows the step-by step process employed to produce the CNS material. The CNS material was fabricated by our industrial partner Cellucomp Ltd. The CNS suspension was derived from carrot pulp waste stream according to the USA Patent[23]. In this manufacturing process (see Fig.1), the carrot pulp waste was first diluted with water to form a mixture with 0.1% to 10% solid content by weight. A sodium hydroxide solution (0.5M) was then added into the mixture to raise its pH to 14. This is to extract a considerable portion of hemicellulose and pectin. Subsequently, the mixture was heated to 90°C for 5 hours followed by 1 hour stirring with a speed of 11 m/s. After heating, the mixture went through a homogenization process for 5 minutes with an agitator blade rotating at a speed of 30 m/s to separate the cells from the mixture along the line of the middle lamella. The separated cells were then broken into nano platelets with dimensions of 50 $\mu m$ in width, 50 $\mu m$ in length and 25 *nm* in thickness. A commercially available dispersant Span 20 (Croda International PLC, UK) was then added into the solution to reduce the aggregation of CNS particles. The final product is a stable suspension contains 4% CNS solids and 96% water with a chemical stoichiometry of $C_{12}H_{24}O_{10}$ for a disaccharide unit. As shown, the CNS exhibits morphology somewhat similar to graphene in terms wrinkles and folding[24]. The CNSs are highly hydrophilic making them dispersible in cement pastes and have a crystallinity index of 70%[23]. Based the centrifugation method for the cellulose nanocrystals with cement paste introduced by Cao et al.(2016)[25], the CNS cementitious composites showed that less than 5% of the CNSs used in the centrifugation experiments are present in the centrifuge solution. And over 95% of the CNSs are adsorbed onto the cement particles surface, indicating that great electrostatic interaction exists between the CNSs and the cement particles.

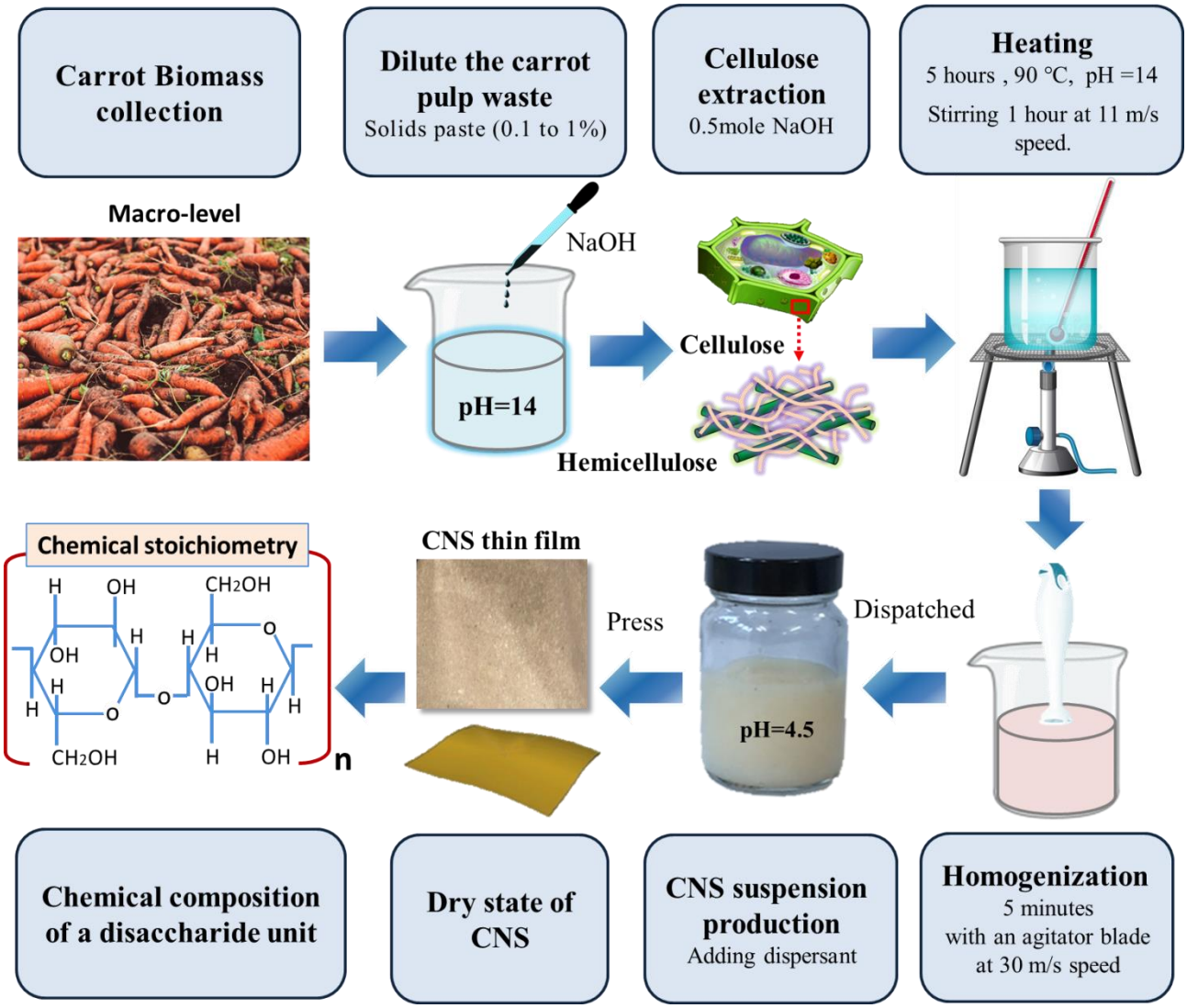


**Fig.1** Fabrication process and microstructure images of CNS

## 2.2. Computational details

*2.2.1 Tricalcium silicate ($C_3S$) and CNS crystal structures*

Alite, the impure form of tricalcium silicate Ca3SiO5 ($C_3S$), is the main phase in OPC and is responsible for setting and strength development of cementitious composites[26,27]. Thus, we examine the chemical interfacial interaction between $C_3S$ and CNS. A monoclinic superstructure of M3 polymorph (MIII-$Ca_3SiO_5$) or (MIII-$C_3S$) is used in this study, which is considered to be the most abundant form in industrial clinkers [28]. The unit cell of MIII-$C_3S$ proposed by Mumme [29] was used as the starting input for the geometry optimization using DFT. As shown in Fig. 2a, the lattice parameters of the $C_3S$ unite cell are: $a$ = 12.235 Å, $b$ = 7.073 Å, $c$ = 9.298 Å, and $\beta$ = 116.931° (space group *Cm*).

The crystalline structure of CNS is composed of four basic allomorphs, including cellulose I, II, III

and IV, where the native cellulose I is the mostly observed allomorph[30]. In addition, two polymorphic cellulose Iα and Iβ structures coexist in the cellulose I with various proportions derived from different sources. The Iα phase is metastable and can be converted into Iβ by hydrothermal treatment or high-temperature treatment in organic solvents[31]. In this paper, the initial structures of Iα and Iβ crystals of CNS are taken from X-ray and neutron diffraction experiments (XRD)[32,33]. The cellulose Iα phase has a triclinic crystallographic structure containing 1 repeatable disaccharide unit that is composed of two anhydroglucose rings. Each saccharide monomer has a stoichiometry of $C_6H_{10}O_5$ and is connected with each other by a so-called 1-4-glucosidic linkage (C1-O4-C4).

Figure 2b shows the measured unit-cell parameters of the Iα polymorph. The unit-cell parameters of Iα polymorph are $a$=6.717 Å, $b$=5.962 Å, $c$=10.400 Å, $\alpha$=118.08º, $\beta$=114.80 º, and $\gamma$=80.375 º (space group $P_1$). The cellulose Iβ phase has a monoclinic crystallographic structure containing two parallel disaccharide units its measured unit-cell parameters are $a$=7.784 Å, $b$=8.201 Å, $c$=10.38 Å, and $\gamma$=96.55 º (space group $P2_1$) (see Fig.2c). The above crystal structures are used to perform the DFT calculations.

It is worth mentioning that the CNSs could contact the cement particles on multiple sides. However, this multi-surface interaction between the CNSs and the cement particles is generally observed at a larger scale (micro/meso scale). The MD simulation for multi-surface interaction could be very challenging and can be achieved by using a coarse-grain based method. In the present study, the CNS was placed on one side of the nanopore in the silicate tetrahedral model with the objective of revealing the hydration mechanism in the cementitious composites.

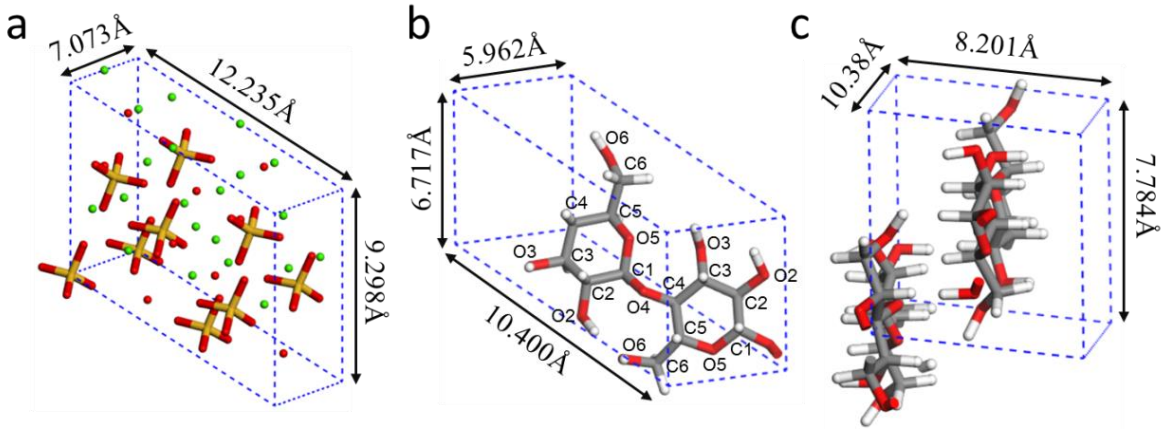


**Fig.2** Crystal primitive cell: (a) MIII-$Ca_3SiO_5$. (b) CNS Iα phase. (c) CNS Iβ phase.

*2.2.2 $C_3S$/CNS molecular model for interfacial interaction analysis during hydration*

In order to understand the effect of CNS chains on the surface hydration of $C_3S$ and probe the molecular interaction at the $C_3S$/CNS interface through molecular dynamics simulations (MD), the original monoclinic crystal structure of $C_3S$ is converted to an orthorhombic structure, developed by Heinz[34] (see Fig. 3a). As shown in Fig.3b, a $C_3S$ supercell containing 2×4×1 crystallographic unit cell is created with lattice dimensions $a$ =24.369 Å, $b$ =28.139 Å, $c$ =25.275 Å, $\alpha=\beta=\gamma=90^o$. The cleavage of the supercell structure is then made in the [0 4 0] direction to generate the $C_3S$ substrate surface. In addition, a vacuum space with a thickness of 5*nm* is built along the $b$ direction to host the water molecules needed for hydration (see Fig.3b). The water molecules are packed and randomly distributed within the vacuum space (see Fig.3c). The number of water molecules satisfies the density of bulk aqueous solution of ≈1g/cm$^3$ under ambient conditions. Since simulating multiple layered CNS needs to build a much larger MD system to achieve computational convergence, which can be very time-consuming. Therefore, we use a single layered CNS in the model. A monolayer CNS containing two chains with a degree of polymerization (DOP) of 4 is placed 5Å above the cleaved $C_3S$ slab surface. The constructed $C_3S$/CNS nanocomposite molecular model is shown in Fig.3d. The final lattice dimensions are $a$ =24.369 Å, $b$ =71.00 Å, $c$ =25.275 Å, $\alpha=\beta=\gamma=90^o$, containing 1030 water molecules and 4320 atoms in total.

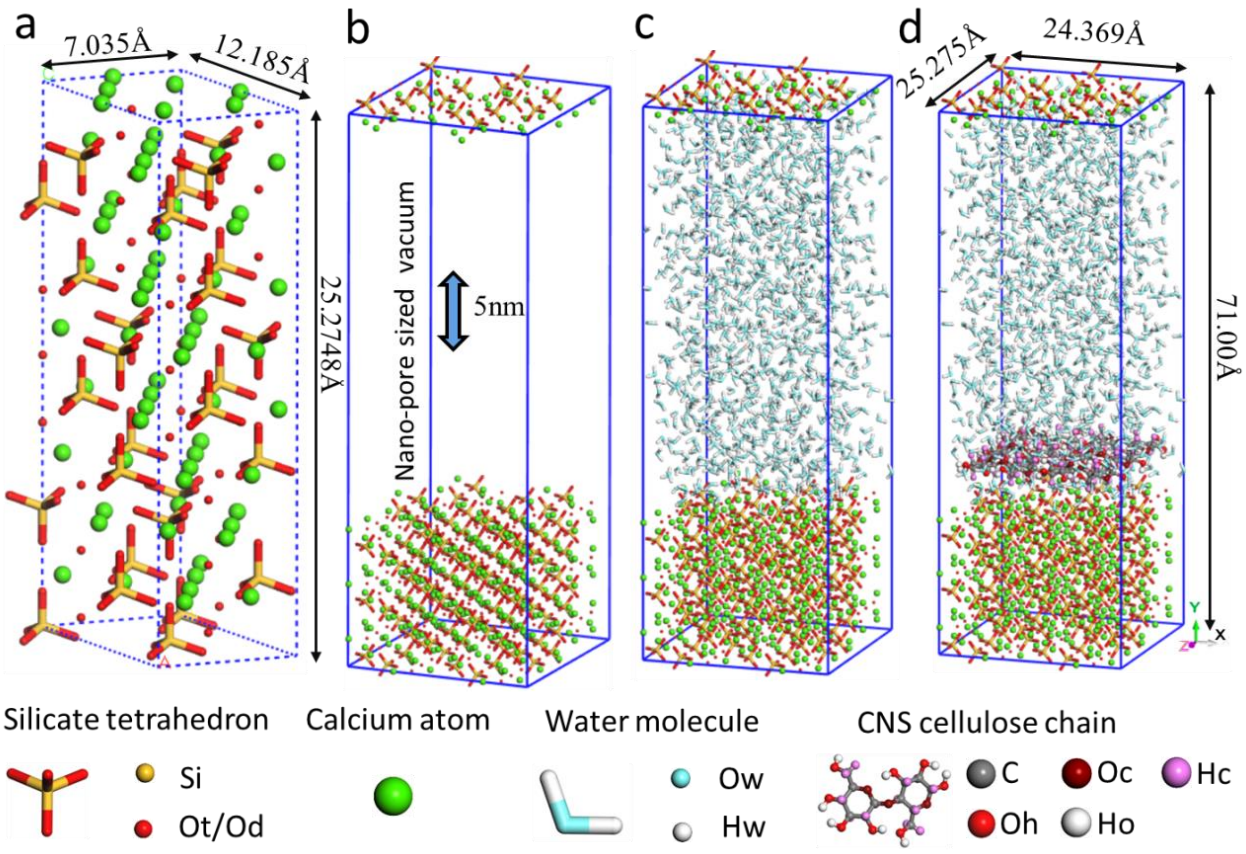

**Fig.3** Construction of interfacial hydration molecular system： (a) transformed orthorhombic $C_3S$ crystal. (b) $C_3S$ supercell with cleaved vacuum space. (c) $C_3S$ water system with randomly packed water molecules. (d) $C_3S$/CNS nanocomposite system with CNS chains.

*2.2.3 DFT calculations*

The density functional theory (DFT) calculations are performed to obtain the geometry-optimized crystal structure and the electronic properties of both the CNS and the $C_3S$ unit cells using the DMol$^3$ package[35]. The exchange and the correlation potential is treated by the generalized gradient approximation (GGA) with the Perdew-Burke-Ernzerhof (PBE) functional[36]. The Van del Waals force for the CNS cellulose hydrogen bonded system is described by the Grimme's DFT dispersion correction approach. The all-electrons method is used for the core electrons treatment. The Brillouin zone of the primitive cell models are sampled with Monkhorst-Pack *k*-point grids of 6×7×4 for the cellulose Iα phase, 6×5×4 for the cellulose Iβ phase and 3×5×4 for the $C_3S$. A double numerical plus polarization (DNP) basis with a global orbital of 5.5 Å is set as a cut-off. This orbital cut-off is found to be enough to achieve convergence with low total energy. The threshold for the self-consistent field (SCF) density tolerance is specified as $10^{-6}$ eV, and direct inversion in an iterative subspace (DIIS) is adopted to speed up the convergence. According to the Aufbau principle, the valence electron configurations include Ca $3s^2 3p^6 4s^2$, Si $3s^2 3p^2$, O $2s^2 2p^4$, C $2s^2 2p^2$, H $1s^1$. Geometric optimization convergence threshold for energy change, maximum force and maximum displacement between optimization cycles are set as $10^{-5}$ Hartree, $10^{-3}$ Hartree Å$^{-1}$ and $10^{-3}$ Å respectively.

*2.2.4 Reactive force field MD simulations*

The DFT quantum chemical computational approach is extremely expensive and is not practical to study phenomena in large and complex systems such as the chemical reactivity at the cleaved $C_3S$/CNS interface with bulk water solution. Therefore, the semi-classical potential based MD simulation is adopted as a less intensive computational alternative to cope with these complex nanocomposite systems. This allows better understanding of the long-term chemical reactivity of the silicate phases while remaining far more computationally efficient than the ab initio simulation. The MD simulations were carried out using the reactive force field (ReaxFF)[37,38] which is implemented in the LAMMPS simulation package[39]. The ReaxFF employs a bond-order formalism in conjunction with the polarizable charge descriptions to describe the interaction between different atoms. The potential energy function is summed by the following partial energy contributions:

$$E_{system} = E_{bond} + E_{over} + E_{under} + E_{angle} + E_{torsion} + E_{Vdw} + E_{Coul} \quad (1)$$

where $E_{bond}$ is the energy associated with forming bonds between atoms, $E_{over}$ and $E_{under}$ are the energies preventing the over coordination and under coordination of atoms, respectively based on the atomic valence rules, $E_{angle}$ and $E_{torsion}$ are the three-body valence angle energy and the four-body torsional angle energy. $E_{Vdw}$ and $E_{Coul}$ are the Van der Waals and Coulomb interaction, respectively, associated with the dispersive and the electrostatic contributions between all atoms.

The ReaxFF has been extensively employed to study the structural and mechanical properties of C-S-H of OPC[40–43] as well as the interfacial strengthening mechanism in C-S-H/polymer nanocomposites[44–47]. It has also been used successfully to examine dissociation of water molecules in C-S-H crystals[48–50]. In addition, the ReaxFF has the ability to capture the bond breakage/formation during the hydration process of OPC by updating bond orders, and elucidate phenomena that take place during chemical reaction of $C_3S$ with water such as dissociation of water, formation of hydroxyl groups ($OH^-$) and the diffusion of hydrogen atoms ($H^+$).

In this study, ReaxFF parameters consisting of a combination of Ca/Si-O-H and C-O-H sets from literature[17,51] were employed to examine the reactivity of $C_3S$ with the CNS chain in the presence of bulk water using the relatively large molecular system shown in Fig.3d. The simulation process is implemented in the following sequence: first, the $C_3S$ substrate and the CNS chain are frozen with fixed zero forces, the bulk water solution is then relaxed with NVT ensemble for 25 picoseconds at an ambient temperature of 300 Kelvin to allow a random diffusion of the water molecules in the nano-pore. Second, after the aqueous solution equilibrium is reached, the rigid $C_3S$ substrate and the CNS chain are unfixed and all atoms in the simulation system are then relaxed to allow the molecular structure to evolve. During relaxation, the energy minimizations are performed using a conjugate gradient method for the $C_3S$/CNS composite molecular system. This is to achieve an overall stable configuration with an energy convergence threshold of $10^{-6}$ Kcal/mole and a force tolerance cutoff of $10^{-6}$ Kcal/mole-Angstrom. The MD simulations are performed within the isothermal-isobaric (NPT) ensemble for 3 nanoseconds at 300 Kelvin temperature. The length of each time step is fixed at 0.25 femtosecond, and a built-in Noose-Hoover style themo/barostatting with a Verlet time-integration scheme is applied throughout the MD simulations. The pressure, temperature, energy and other thermodynamic information are monitored during simulation to ensure stability of the system.

The structural and dynamics information such as the atomic intensity, radial distribution function (RDF), mean squared displacement (MSD) and $OH^-$ number are analyzed to characterize the effect of CNS on the hydration of $C_3S$ resulting from the chemical interaction at the $C_3S$/CNS interface during the hydration over a timescale of a few nano seconds. The MD simulation of the hydration over much longer time scales to study the oligomerization of silicate "Dreierketten" chain and the deposition of C-S-H nanoscale colloidal cluster is time consuming and thus is omitted from this study.

By combining density functional theory and molecular dynamics simulation using a reactive potential, we aim to ambiguously elucidate the influences of CNSs on the reactivity and hydration mechanism of $C_3S$, the most reactive phase in anhydrous ordinary Portland cement. First, a detailed electronic analysis can reveal the reactivities of both CNS and $C_3S$ phases and detect the dominating active sites for potential reactions. The bond formation mechanism among different atom species based on the PDOS analysis from DFT can set up a base for analysis of reaction kinetics and hydration product nucleation process in MD simulation. Such DFT calculations can consolidate our understanding and shed light on the fundamentals of chemical interactions between the CNS and $C_3S$ surfaces. This enables us to uncover kinetics responsible for the increase in the hydration of cement.

The outcomes of DFT (including the geometry-optimized crystal structure, and the subsequent cleaved $C_3S$ surface) were used as inputs to directly observe the hydration of $C_3S$ surfaces in contact with the bulk water containing CNS via reactive MD simulations. The reactivity and hydration mechanism employed in our DFT can be further confirmed by examining the sol-gel interaction process using MD simulations. This combined DFT and MD approach allows us to study both the initial and the longer-term hydration behaviors, and establish correlations between the electronic property and the chemical reactivity of both CNS and $C_3S$ phases, which is critical to understanding the relevant physiochemical processes during hydration and dissolution of the $C_3S$/CNS hybrid composite.

### 2.3. Experimental characterization of the hydrate phases growth

Experimental tests were conducted to quantify the change in the hydrate phases of OPC as a result of CNS and support the findings of the MD simulations. Cement matrices were prepared by mixing OPC CEM I 52.5N (Table 1) and water with a water-to-cement ratio of 0.35**.** To realistically quantify the effect of CNS on the DOH of cement for practical applications, the CEM I 52.5N was used in this experiment. The CEM I consists of tricalcium silicate, dicalcium silicate, tricalcium aluminate and

calcium alumino-ferrite. Its mix proportion was determined as $C_3S$: $C_2S$: $C_3A$: $C_4AF$=57.1:17.4:6.2:6.9. The cement used in the present study was not a pure form of Alite, and because of this the authors are fully aware that deviations between the experimental test results and the MD predictions are expected. In order to eliminate and minimize the test errors, we have repeated the experiments for one mix proportion with a fixed CNS dosage and the results were then averaged to probe the effect of CNS on the DOH from a statistic approach.

The commercially available high-efficiency water reducer (Glenium 51) of 1.0 wt% was used to enhance the workability of the cement pastes. The cement pastes were prepared at CNS concentrations of 0, 0.1, 0.2 and 0.4 wt%. The water-to-cement ratio was adjusted to account for the water in the CNS suspension. During the paste preparation process, the CNS suspensions were first mixed with the required amount of superplasticizer and water. Then the resulting aqueous solutions were treated with mild sonication in an ice bath environment for 30 minutes. Subsequently, the obtained solutions were blended with the cement powder and mixed for 8 minutes. The obtained pastes were then poured into (50 mm×50 mm×50 mm) molds and shaken for 1 minute with a vibrator in order to remove air bubbles. After casting, the molds surface was sealed with a plastic film to minimize water evaporation during hydration. The samples were demolded after curing 24 hours and cured in water at a temperature of 21$^{o}$C for 28 days. Three samples per CNS concentration were prepared and used to quantify the effect of CNS on the hydration of OPC matrices after 28 days of curing.

Table 1 Chemical composition of CEM I 52.5N cement

| $SiO_2$(%) | $Al_2O_3$(%) | $Fe_2O_3$(%) | CaO(%) | MgO(%) | $SO_3$(%) | $K_2O$(%) | $Na_2O$(%) | Cl(%) |
|---|---|---|---|---|---|---|---|---|
| 21.46 | 4.79 | 2.29 | 64.98 | 2.25 | 3.33 | 0.56 | 0.29 | 0.05 |

A combined Thermography Analysis (TGA) and Differential Scanning Calorimetry (DSC) tests were carried out on the 28-d cured cementitious nanocomposite samples to quantify the effect of CNS on the growth of their hydrate products based on their thermal behavior. The TGA was used to evaluate the mass change of the heated samples under controlled conditions whereas the DSC was used to measure the amount of heat difference during elevation of temperature. The previously prepared cubic samples were ground into powder using a planetary ball mill (Planetary Ball Mill PM 100). Sieved powder samples (fineness less than 1 mm) of weight of 30 mg were then transferred to the TGA-DSC (STA 449 F3 Jupiter) crucibles for thermal analysis and the temperature of the samples was raised

from 20 °C to a critical temperature of 140 °C at a rate of 10 °C /min. The heating temperature of 140 °C was maintained for 30 minutes to remove the free water and the residual mass of the sample under this temperature was set as the benchmark. Subsequently, the samples were heated from 140 °C to 1100 °C at a rate of 10 °C/min. The entire TGA/DSC experiment was performed in a nitrogen environment with an inert atmosphere nitrogen flow rate of 25.00ml/min. The change in the mass of the samples along with the samples heat capacity difference were analyzed to study the influence of CNS on the thermal and kinetic reactions of OPC hydration and quantify the change in the degree of hydration due to the synergistic effects between the $C_3S$ and the CNS.

Scanning Electron Microscope (SEM, JEOL, JSM-7800F) was used to examine the effect of CNS on the morphology of the microstructure of the cementitious nanocomposites at a working voltage between 5 and 15 kV. Cementitious fragments were first dried in a vacuum oven at 80 ° C for 24 hours then their surface was coated with gold in order to provide a homogeneous surface for analysis and imaging. Transmission electron microscope (TEM) (JEM -1010) was employed to characterize the CNS on the growth of the hydrate phases. The cementitious composites in the form of powder samples were mixed with acetone solution and were then sonicated for 15 minutes using an ultrasonic oscillator. The solutions were dropped on carbon-coated copper grids (300 mesh) and left to dry at room temperature. Upon drying, TEM images were generated at 80 kV accelerating voltage. X-ray diffraction (XRD) (Agilent SuperNova) was also employed to further examine the degree of hydration and determine the crystallinity of the hydrate phases. The cementitious composites in the form of powder samples were dried in a vacuum oven for 24 hours at 80° C and coated with gold before analysis. The working voltage of the XRD ranged from 5kV to 15kV. XRD patterns were recorded at a scanning rate of 2°/min from $2\theta = 5°$ to 90° with Cu Kα radiation ($\lambda = 1.5418$ Å).

## 3. Results and discussions

### 3.1 Morphology of CNS

The molecular structure and SEM/TEM micrographs showing the morphology of the CNS are depicted in Fig.4. The CNS crystalline molecules are formed from repeating saccharide units that are covalently linked by a β-1-4 glycosidic(C-O-C) bond. Different functional groups including the hydroxymethyl group(-$CH_2OH$), hydroxyl group(-OH) and hydrocarbon methine group(-H) are grafted on the backbone tetrahydropyran ring (Fig. 4a). The saccharide units are then polymerized to form a single chain. As can be seen from the SEM images of the dry state CNS (Figs.4b-c), the CNS

microfibrils are stacked tightly during the biosynthesis process, resulting in the formation of semi-crystalline CNS sheets. As shown in the TEM images in Fig. 4(d-e), the CNS microfibrils are further composed of randomly oriented nanofibrils, as result of the stacking of CNS molecular chains. These CNS nanofibrils and cellulose chains in dry state still relatively uniformly dispersed throughout the cement matrix and interact with the cement particles during hydration.

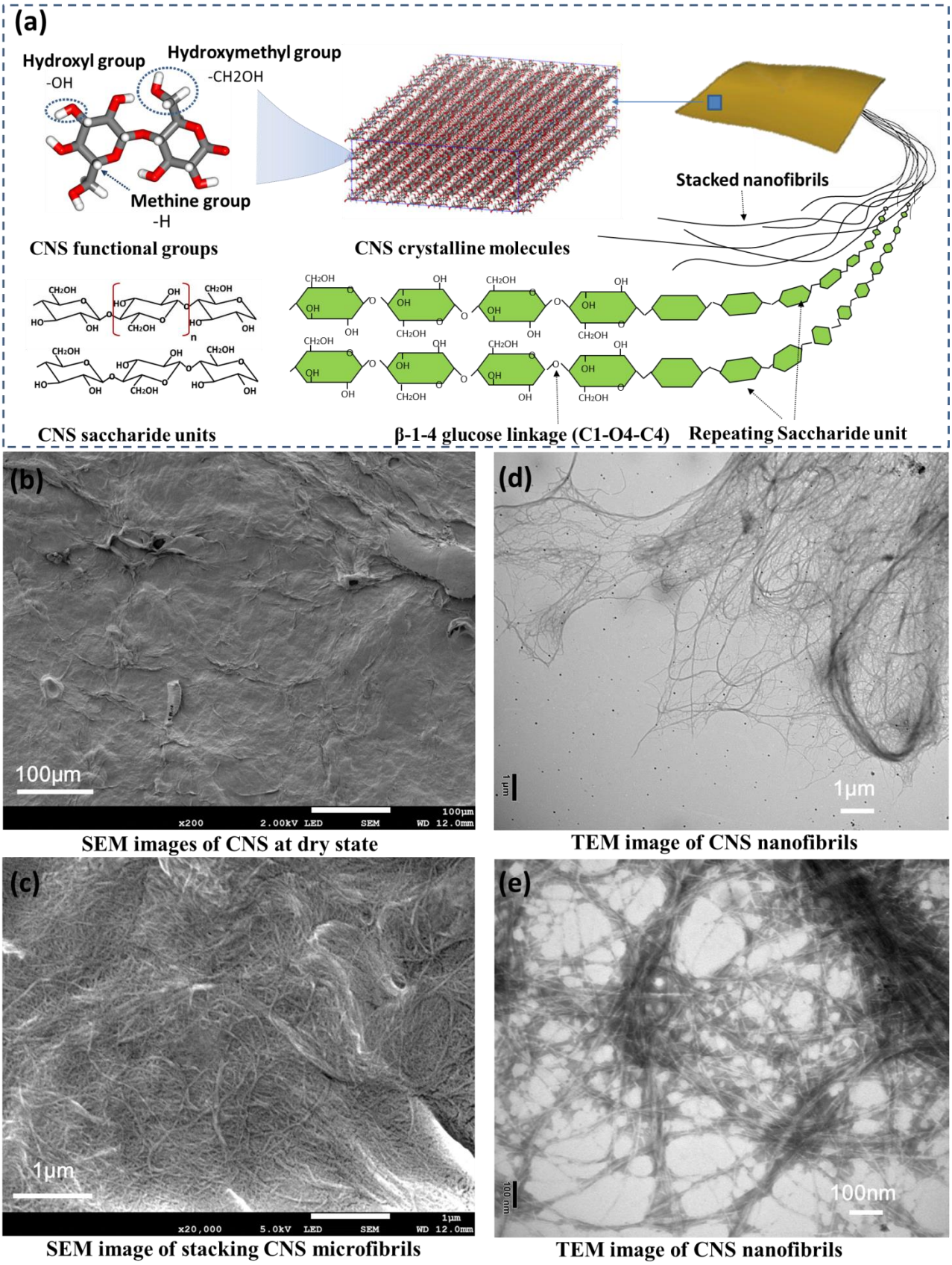


Fig.4 Chemical structure and morphology of CNS

### 3.2 DFT simulation results

DFT simulations are performed to calculate the electronic properties and uncover the atomic mechanism of interactions at $C_3S$/CNS interface. First, the relaxed lattice parameters of CNS Iα and Iβ crystals, and the $C_3S$ crystalline primitive cell are calculated and validated using previous experimental data [29,32,33]. Table 2 indicates that the DFT predicted lattice parameters are in a good agreement with the reported experimental lattice parameters with an estimated error less than 1.5 % for all the 3D cell parameters of $C_3S$ and CNS crystals.

Table 2 Lattice parameters obtained from DFT calculations

| | $C_3S$ | | | Cellulose Iα | | | Cellulose Iβ | | |
|---|---|---|---|---|---|---|---|---|---|
| | DFT | Expt | Error(%) | DFT | Expt | Error(%) | DFT | Expt | Error(%) |
| *a*(Å) | 12.142 | 12.235 | 0.76 | 6.671 | 6.717 | 0.69 | 7.776 | 7.784 | 0.10 |
| *b*(Å) | 7.107 | 7.073 | 0.48 | 6.027 | 5.962 | 1.08 | 8.196 | 8.201 | 0.06 |
| *c*(Å) | 9.349 | 9.298 | 0.55 | 10.371 | 10.400 | 0.28 | 10.385 | 10.380 | 0.47 |
| *α*(°) | 89.963 | 90.000 | 0.04 | 119.733 | 118.080 | 1.38 | 90.003 | 90.000 | 0.00 |
| *β*(°) | 115.844 | 116.310 | 0.40 | 111.423 | 114.800 | 3.03 | 90.012 | 90.000 | 0.01 |
| *γ*(°) | 89.997 | 90.000 | 0.00 | 82.439 | 80.370 | 2.51 | 96.526 | 96.550 | 0.02 |

As shown in Table 3, the key structural inter-chain parameters of CNS crystalline obtained from DFT are also validated using experimental results [52,53] in terms of glycosidic dihedral angles Φ (O5-C1-O4-C4) and Ψ(C1-O4-C4-C5), glycosidic bond angle $\tau$ (C1-O4-C4) and hydroxymethyl dihedral angles including $\chi$ (O5-C5-C6-O6) and $\chi'$ (C4-C5-C6-O6).

Table 3 Comparisons of structural intra-chain parameters for crystalline cellulose Iα and I β

| | Iα | | | | I β | | | |
|---|---|---|---|---|---|---|---|---|
| | DFT | | EXPT | | DFT | | EXPT | |
| | Residue1 | Residue2 | Residue1 | Residue2 | Chain1 | Chain2 | Chain1 | Chain2 |
| Φ (°) | 90.4 | 96.7 | 98 | 99 | 94.8 | 88.6 | 99 | 89 |
| Ψ (°) | 146.3 | 148.3 | 138 | 140 | 142.7 | 147.9 | 142 | 147 |
| $\tau$ (°) | 117.2 | 116.5 | 116 | 116 | 116.9 | 116.9 | 115 | 116 |
| $\chi$ (°) | 165.7 | 150.0 | 167 | 166 | 165.7 | 161.6 | 170 | 158 |
| $\chi'$ (°) | 77.7 | 75.8 | 75 | 74 | 76.9 | 78.4 | 70 | 83 |

These angles are pertaining to the independent glycosylic residues for cellulose Iα unit cell, and to the two nonequivalent chains for the cellulose Iβ unit cell [54]. For the Iα phase, the two glucopyranosyl residues are nonequivalent within one repeating cellobiose, whereas for the Iβ phase, the glucopyranose units within one cellobiose are equivalent but slightly different between the two D-glucose chains[55]. This phenomenon is successfully reproduced by our DFT simulations.

As shown in Table 3, the agreement between the DFT results and the experimental results for the

dihedral and the bond angles are within 10%. The DFT results for both $C_3S$ and CNS are within the range observed from the available experimental data [29,52,53,56,57]. Based on the above comparisons, the validity of the DFT calculations is thus confirmed, which sets a clear benchmark for the following electronic description of the $C_3S$ and the CNS crystals.

The Fukui function[58]is employed to study the interaction of the $C_3S$ with the CNS during hydration. This function is widely utilized to determine the chemical reactivity of molecules towards other molecules for bulk systems or specific surfaces. The Fukui function f(r) is defined as the differential change in the electron density (ρ(r)) of a molecular system with respect to the differential change in the total number of electrons (N): $f(r) = (\partial\rho(r)/\partial N)$[59,60]. Its field distribution provides useful information on the reactivity localization in bulk systems, where the regions that are marked by electronic clouds are likely to undergo higher chemical reactivity. Like the Frontier Orbital Theory (FOT), the Fukui function is particularly useful for understanding how nucleophiles attack the highest occupied molecular orbital (HOMO) while at the same time placing their surplus of electrons into the lowest unoccupied molecular orbital (LUMO). The electrophilic attack (defined as: $f^-(r) \sim \rho_{HOMO}(r)$) is associated with the charge donation that induces an electron decrease in the system. The nucleophilic attack (governed by $f^+(r) \sim \rho_{LUMO}(r)$) indicates that the system accepts an electron charge thus causing an electron increase. For bulk systems, the HOMO and LUMO are described by the valence band maximum (VBM) and conduction band minimum (CBM), respectively[56,57].

*3.2.1 Electronic properties of $C_3S$*

Figs.5a-c show the optimized geometry of the MIII-$C_3S$ crystal structure together with the obtained HOMO, total electron density and LUMO orbital distributions. There are two types of oxygen in the $C_3S$ primitive cell: the first type is the tetrahedral oxygen (Ot) covalently bonded to silicon atoms forming silicate tetrahedron groups with Si-O bond lengths between 1.61−1.68 Å. The second type is the dangling oxygen (Od) having an ionic character and coordinated with 5 or 6 calcium atoms with a Ca-O ionic bonding distance within 2.38−2.46 Å. As expected, the HOMO orbital density for the $C_3S$ unit is mainly concentrated around the dangling ionic oxygen Od atoms, implying that the Od atoms serve as nucleophiles and are more susceptible to react with the environmental electrophiles (e.g $H^+$) to form oxides or hydroxyls. The tetrahedral oxygen Ot atoms also show potential to react with the proximate $H^+$ protons leading to the hydration of orthosilicate $[SiO_4]^{4-}$ and the formation of silicic acid such as dihydrogen orthosilicate ions $H_2SiO_4$ and trihydrogen orthosilicate ions $H_3SiO_4$.

Figures 5a-c show that the LUMO orbital density of $C_3S$ has a more delocalized electron distribution with its partial charge density exists at interstitial sites among the silicon tetrahedra and accumulates in the vicinity to the calcium atoms. This suggests that these particular sites are more prone to experience nucleophilic attack by $OH^-$ groups from water dissolution and hydroxyl functional groups from the CNS. These findings are consistent with the reported feature of $C_3S$ obtained from DFT calculations[56,57,61].

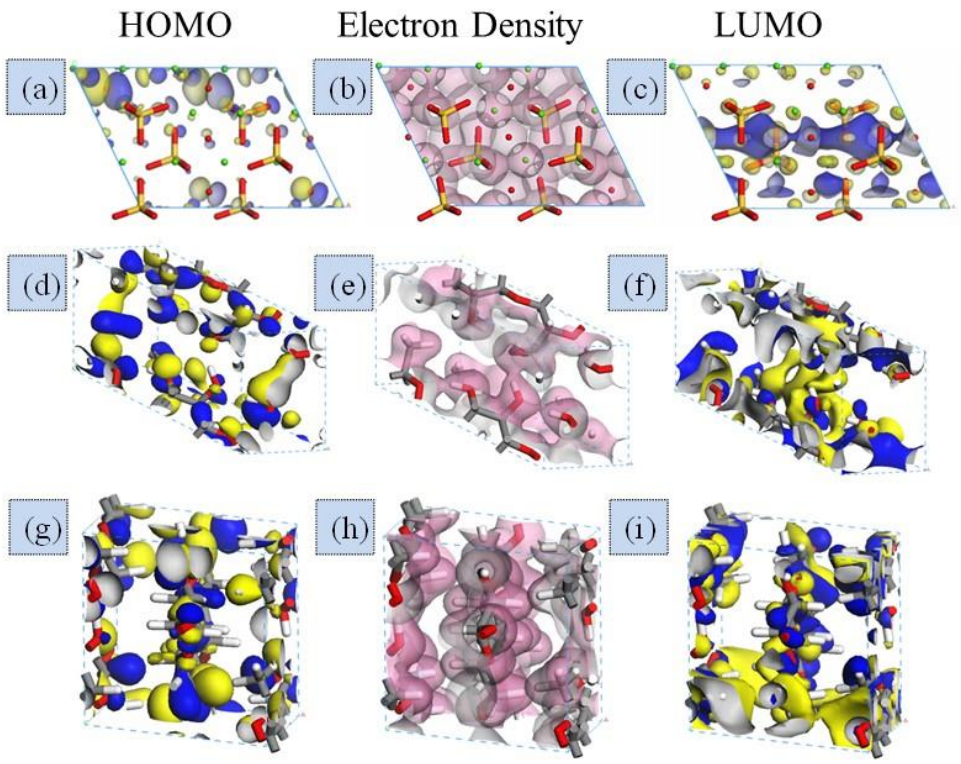


**Fig.5** HOMO, Electron density and LUMO density of crystals with field isosurface level of ±0.02e $Å^{-3}$. (a-c) $C_3S$ primitive cell. (d-f) CNS Iα phase primitive cell. (g-i) CNS Iβ phase primitive cell.

*3.2.2 Electronic properties of CNS crystals*

Figure 5d-f and 5g-i show the HOMO, electron density and LUMO density of CNS Iα and Iβ crystals, respectively. As shown, the HOMO orbital distributions of the CNS Iα and Iβ units are mainly localized around the oxygen atoms of the functional groups and the glycosidic linkage. According to the FOT, these oxygen atoms are likely to lose electrons compared to the rest of the system. Therefore, the oxygen atoms are the reaction sites that will undergo electrophilic attack and interact with the environmental cations, such as $Ca^{2+}$ from the $C_3S$, or $H^+$ proton from the bulk water. The LUMO orbitals of the CNS units show much denser electronic clouds capping over the whole backbone carbon and hydrogen atoms from the functional groups of CNS. This implies that the electrophilic

sites (C and H) on the surface of CNS react with the surrounding anions such as the dissociated water groups $OH^-$.

*3.2.3 Partial density of states of $C_3S$*

In addition to examining the electron localization in the $C_3S$ structures and the CNS unit cells, the spin-unrestricted partial density of states (PDOS) are also calculated to 1) understand the origin of the electronic structure, 2) unravel the nature of orbital hybridization and bonding mechanism in the bulk system, and 3) clarify both the contribution of respective orbitals to the total density of states (DOS) near band edges and the trend to donate or withdraw electrons. The location of Fermi energy level ($E_F$) is assigned as zero energy scale[62] and is marked by a dashed line. All energies are relative to the Fermi level.

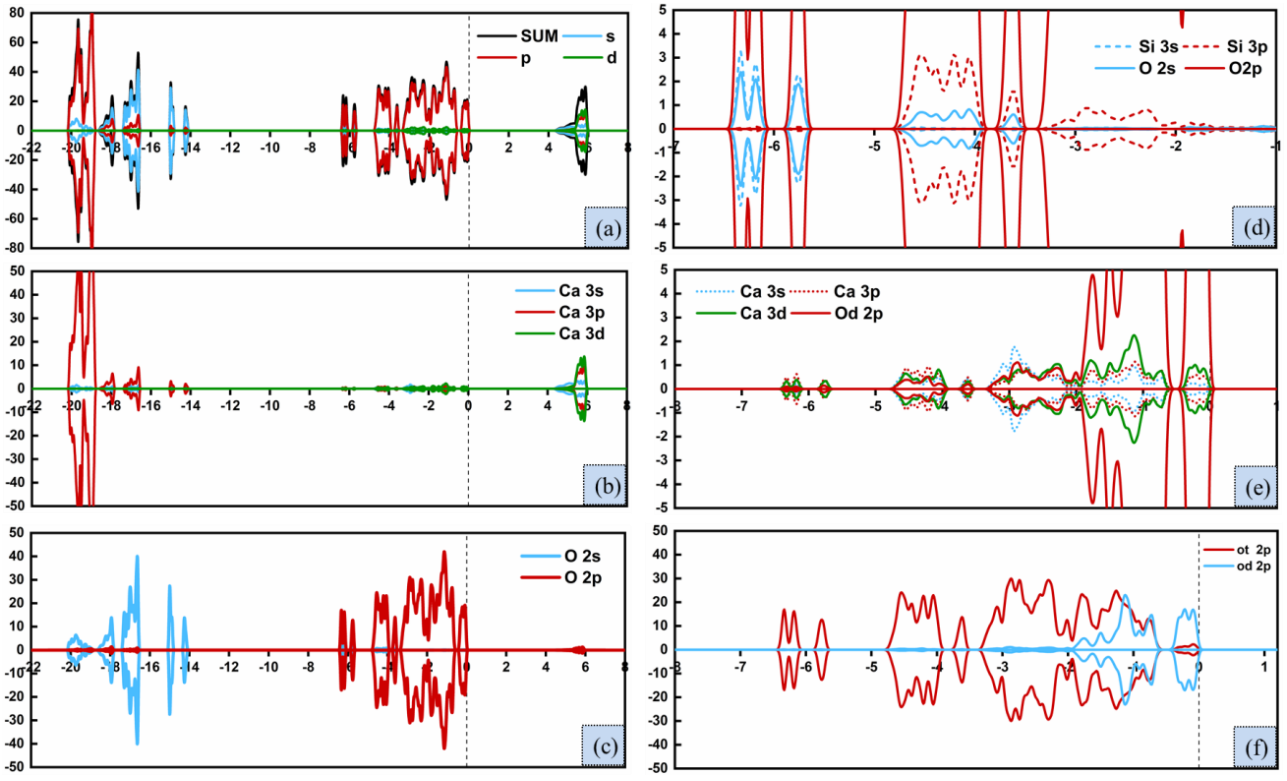


**Fig.6** Spin polarized PDOS of $C_3S$ crystal. a) total density state of s, p, d orbitals. b) PDOS of Ca-3s, Ca-3p, Ca-3d orbitals. c)PDOS of O-2s, O-2p orbitals. d)hybridization of Si-3s, Si-3p orbitals with O-2s and O-2p orbitals at medium energy level. e) resonance of Ca-3d and O-2p orbitals. f) LDOS of Od and Ot atoms

Fig.6 shows the total and orbital projected PDOS of $C_3S$. The smearing method with a level broadening of 0.03eV is used to integrate the PDOS. Three main quantum chemical parameters of $C_3S$ are obtained as $E_{HOMO}$=-7.518eV, $E_{LUMO}$=-2.917eV, and band gap energy $\Delta E = E_{LUMO} - E_{HOMO}$=

4.241eV, which are very close to the previous ab initio calculated values for pure $C_3S$[57]. As can be seen from Figs.6a-c, the valence band (VB) PDOS near the $E_F$ is the result of the O-2p orbitals. The Si-3s and the Si-3p orbitals have slight contributions to the VB at medium range i.e., -2eV to -6.47 eV) but have remarkable orbital $sp^3$ hybridization with O-sp orbitals (see Fig.6d). This indicates the relative stability of the covalent Si-O bonding characteristics. At short range of VB near the $E_F$ (from Fermi level to -2eV), the Ca-3d orbital has the strongest resonance with the Od-2p orbital, implying ionic Ca-O bond connection (see Fig.6e). As depicted in Figs.6b-c, the PDOS valence bands congregate at very low energy levels between -14 eV to -20 eV which corresponds to O-2s and Ca-3p orbitals. These two states are far away from $E_F$ and are known to be relatively stable with energetically unfavorable to electron exchange with the surrounding environment in comparison to the O-2p states. On the other hand, the conduction band (CB) PDOS above the $E_F$ is dominated by all s, p, d states from calcium cations. This further confirms that the chemical reactivity of $C_3S$ is primarily attributed to the O and Ca atoms, which is in line with the observations obtained from the HOMO and LUMO orbital electron clouds.

Figure 6f compares the local density of states (LDOS) for different oxygen species in the $C_3S$ cell. As can be seen, the density of Od atom in the VB is significantly higher than the Ot near the Fermi energy. This is partially attributed to their different charge transfer properties. According to the reported Bader charge analysis of the pure MIII-$C_3S$ structure[56], the net charge of each dangling ionic oxygen Od is -1.54 e and the net charge of each tetrahedral oxygen Ot is -1.45e. This means the Od withdraws an additional 0.09e charge from the system, indicating that when more charge is localized in the HOMO, the Od-2p orbitals around the maximum valence band is enhanced. This indicates that the Od site is more chemically reactive and is more susceptible to adsorption of electrophilic species than the Ot site.

*3.2.4 Partial density of states of CNS crystals*

For the CNS unit cell, the spin polarized PDOS of Iα and Iβ crystals are plotted in Fig.7. As shown, the Iα and Iβ cellulose primitive cells exhibit similar PDOSs, and the predicted band energy gaps is 5.349eV for the Iα crystal and 5.653 eV for the Iβ crystal (see Figs.7a,b). The relatively large band gaps with almost matching spin-up and spin down orbital states indicate that the native cellulose is a nonmagnetic semiconductor. The slightly lower value of the band gap energy of Iα polymorph with more DOS in the higher energy level of conduction band further confirms its meta-stable state in

comparison to Iβ polymorph.

As clearly indicated in Fig.7, the top of the valence bands (TVB) near the $E_F$ for both Iα and Iβ cellulose crystals are mainly provided by the 2p orbitals of oxygen atoms (see Figs.7c, d). As expected, the oxygen atoms exhibit a clear electron donating trend. Slight contributions of the 2p orbitals of carbon atoms are also observed in Figs.7e, f. The bottom of the conduction bands (BCB) are mainly the contribution of the C-2p and H-1s orbitals in both Iα and Iβ crystals as shown in Figs.7e-h.

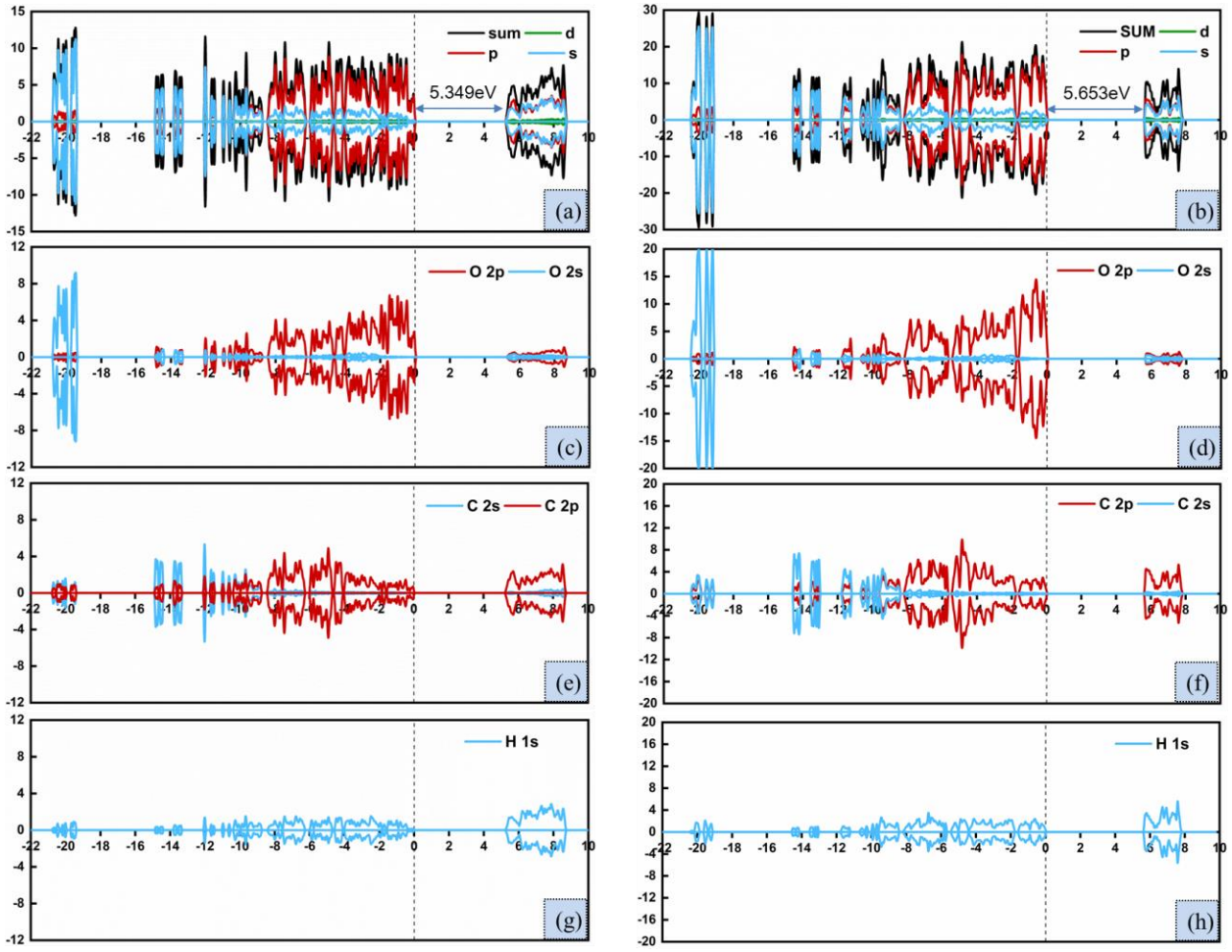


**Fig.7** Spin polarized PDOS of Iα and Iβ crystal. a) total density state of s,p,d orbitals for Iα phase. b) total density state of s,p,d orbitals for Iβ phase. c) PDOS of O-2s, O-2p orbitals for Iα phase. d) PDOS of O-2s, O-2p orbitals for Iβ phase. e) PDOS of C-2s, C-2p orbitals for Iα phase. f) PDOS of C-2s, C-2p orbitals for Iβ phase. g) PDOS of H-1s orbitals for Iα phase. h) PDOS of H-1s orbitals for Iβ phase.

Figure 8a presents the VB LDOS of 2p orbitals for different oxygen atom species for the Iα structure This figure indicates that the largest contribution to the TVB around the $E_F$ is attributed to the O6 sites resulting from the hydroxymethyl conformation of Iα phase (the atom numbering is given in

Fig.2). Figure 8b shows that for the Iβ phase, the most occupied energy level for the O6 site in the hydroxymethyl group is distinct from the other oxygen sites. The peak position of VB PDOS near the Fermi level for O6 site lies at higher energy by about 0.114 eV than those for the other oxygen sites (marked as dash arrow in Fig.8b). This implies that the O6 atoms with smaller energy gap between the highest occupied energy level and the Fermi level is expected to exhibit higher chemical reactivity during hydration. The methyl oxygen atoms pointing out from the glucopyranose ring are more vulnerable to electrophilic attack. The other oxygen sites (O2, O3, O4 and O5) are showing similar reactivity as they possess the same peak position in the VB PDOS.

With respect to the bottom of the conduction bands (BCB), the carbon atoms C4, C5 and C1 that are directly connected to the backbone oxygen (O5, O4) dominate the contributions to the BCB, followed by the C6, C2 and C3 sites as shown in Figs.8c,d for Iα and Iβ phases, respectively. These carbon sites possess nearly identical peak positions at the BCB nearest to the $E_F$, implying a similar energy barrier for electrons gain. This suggests that all carbon sites play almost an equal role in the chemical reaction with the environmental nucleophiles such as Ow from water.

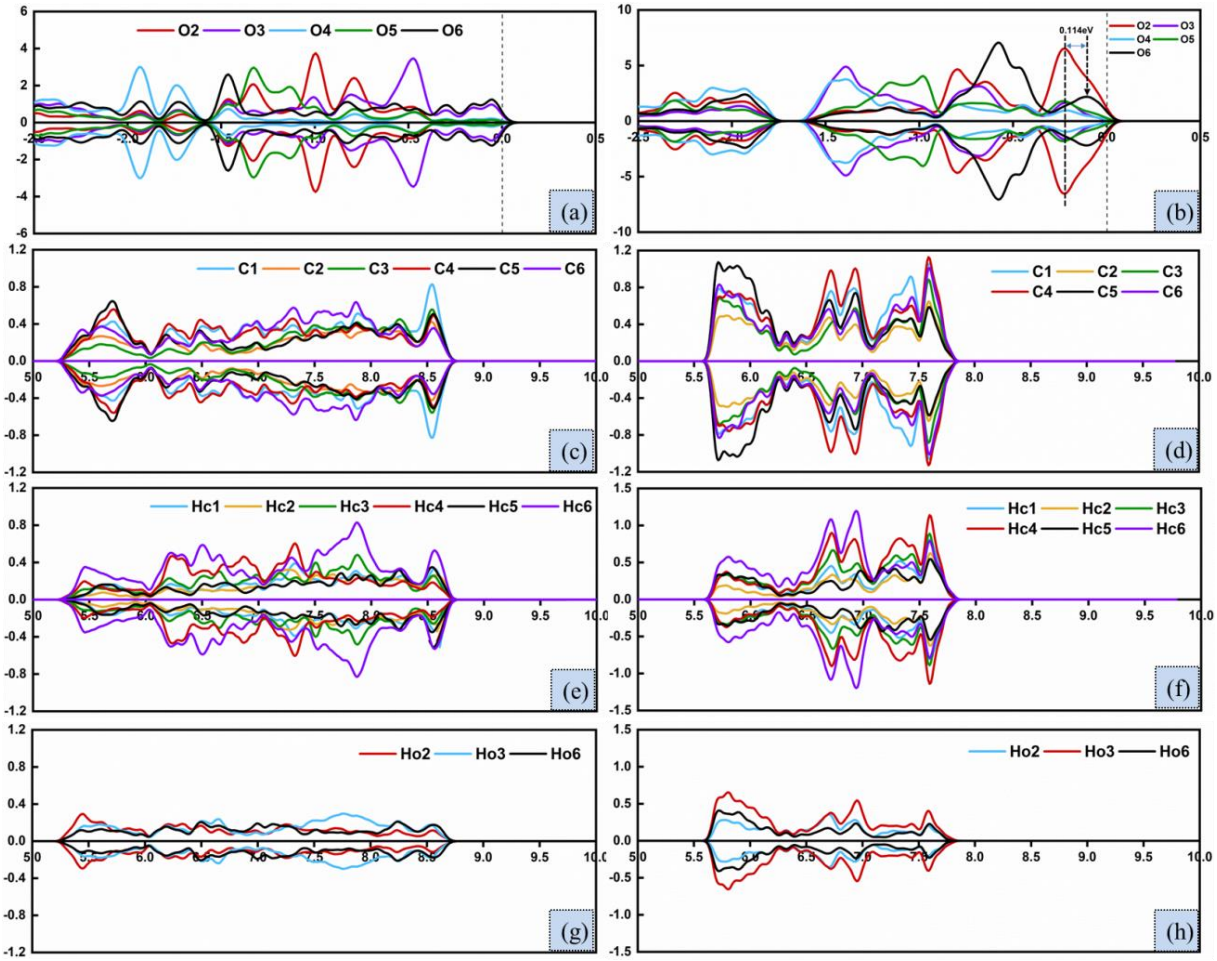


**Fig.8** Spin polarized LDOS of for different atom species in CNS Iα and Iβ crystals. a) LDOS of

oxygen atoms for Iα phase. b) LDOS of oxygen atoms for Iβ phase. c) LDOS of carbon atoms for Iα phase. d) LDOS of carbon atoms for Iβ phase. e) LDOS of hydrogen atoms from methine group for Iα phase. f) LDOS of hydrogen atoms from methine group for Iβ phase. g) LDOS of hydrogen atoms from hydroxyl/hydroxymethyl group for Iα phase. h) LDOS of hydrogen atoms from hydroxyl/hydroxymethyl group for Iβ phase.

The hydrogen atoms on the surface of the CNS, are categorized herein as: hydrophobic methine hydrogens (Hc1-Hc6) atoms associated with the carbon atoms from the hydrocarbon moieties (C-H), hydroxyl hydrogens (Ho2 and Ho3) atoms linked to the oxygen in the hydroxyl radical (-OH) and methylene hydrogen (Ho6) atoms connected to the oxygen in the hydroxymethyl functional group (-$CH_2OH$). Among the methine hydrogens atoms illustrated in Figs.8e-f, the contribution of CB PDOS is mainly attributed to the Hc6 site from the hydroxymethyl group. The others Hc1-Hc5 sites also contribute to the formation of the conduction band. It is interesting to note that the LDOS of hydrogen atoms from the functional groups only offer moderate contributions to the whole conduction band (see Figs.8g-h). These contributions, however, are slightly less than those of the methine hydrogens atoms.

The hydrogen atoms from the functional groups in CNS provide relatively higher charge from the Hirshfeld-based population analysis (see Table 4). This could be attributed to intra-chain hydrogen bonds between the neighboring oxygen such as O2-Ho2…O6, O3-Ho3…O5 and O6-Ho6…O3 bonds as observed in reported experiments[63,64]. As a result, their capacity to attract environmental electron is weakened. However, the reactivity sequence for these different atom sites is generally a correlated trend of the atomic Hirshfeld charge obtained from the population analysis. This confirms the reactivity of different atom species on the surface of CNS. In this case, the atoms carrying higher positive charge are more likely to attract electrons from their neighbors whereas the atoms with lower electronegativity are prone to donate electrons to their neighbors. Because of this, the CB PDOS results show that the C and H atoms are the main active atoms of CNS that are susceptible to nucleophilic attack such as Ow anion from water hydrolysis and Od anion and $[SiO_4]^{4-}$ group as a result of $C_3S$ dissolution. Moreover, the O atoms on the surface of CNS are prone to electrophilic attack by the electrophiles such as $Ca^2$ cations in the $C_3S$ surface.

Table 4 Hirshfeld population for different atom species in CNS

| Atoms species | Hirshfeld charge of Iα phase | | | Hirshfeld charge of Iβ phase | | |
|---|---|---|---|---|---|---|
| | Residue 1 | Residue 2 | SUM | Chain 1 | Chain 2 | SUM |
| O2 | -0.186 | -0.170 | -0.356 | -0.196 | -0.192 | -0.388 |
| O3 | -0.200 | -0.196 | -0.396 | -0.157 | -0.169 | -0.326 |
| O4 | -0.096 | -0.086 | -0.182 | -0.093 | -0.095 | -0.188 |
| O5 | -0.096 | -0.100 | -0.196 | -0.099 | -0.095 | -0.194 |
| O6 | -0.196 | -0.150 | -0.346 | -0.168 | -0.163 | -0.331 |
| C1 | 0.093 | 0.096 | 0.189 | 0.094 | 0.093 | 0.187 |
| C2 | 0.017 | 0.018 | 0.035 | 0.017 | 0.015 | 0.032 |
| C3 | 0.018 | 0.018 | 0.036 | 0.021 | 0.024 | 0.045 |
| C4 | 0.030 | 0.026 | 0.056 | 0.027 | 0.027 | 0.054 |
| C5 | 0.027 | 0.028 | 0.055 | 0.033 | 0.032 | 0.065 |
| C6 | 0.011 | 0.001 | 0.012 | -0.008 | -0.013 | -0.021 |
| Hc1 | 0.038 | 0.040 | 0.078 | 0.034 | 0.036 | 0.070 |
| Hc2 | 0.025 | 0.024 | 0.049 | 0.029 | 0.023 | 0.052 |
| Hc3 | 0.028 | 0.031 | 0.059 | 0.030 | 0.034 | 0.064 |
| Hc4 | 0.044 | 0.042 | 0.086 | 0.039 | 0.039 | 0.078 |
| Hc5 | 0.030 | 0.030 | 0.060 | 0.033 | 0.031 | 0.064 |
| Hc6 | 0.025,0.031 | 0.034,0.041 | 0.131 | 0.03,0.023 | 0.025,0.019 | 0.097 |
| Ho2 | 0.122 | 0.107 | 0.229 | 0.100 | 0.097 | 0.197 |
| Ho3 | 0.105 | 0.103 | 0.208 | 0.110 | 0.108 | 0.218 |
| Ho6 | 0.101 | 0.115 | 0.216 | 0.107 | 0.110 | 0.217 |

Based on the above analysis, it can be postulated that the HOMO and the LUMO in $C_3S$ and CNS unit cells are very likely to overlap and form $C_3S$/CNS complex hydration products, where formation of new Ca-O and O-H chemical bonds between different atom species can be induced by the molecule dissociation and the atom diffusion. The $C_3S$ suffers simultaneously nucleophilic and electrophilic attacks from CNS and water molecules during the hydration process. This is because the Ca atom is an electron acceptor for the water oxygen (Ow), CNS backbone oxygen (Oc) and the functional group oxygen (Oh). In addition, the Ot and Od atoms act as electron donors that accept H+ proton from water (Hw), as well as hydrogen from CNS methine groups (Hc) and hydroxyl/hydroxymethyl functional groups (Ho). This also leads to the formation of complex hydration products.

### 3.3 Molecular dynamics simulation

Determining the solute and solvent-mediated reaction kinetics at the $C_3S$/CNS interface from the first principles DFT calculations at quantum mechanics levels is difficult[65,66]. Therefore, we perform larger scale reactive MD simulations to understand the effect of CNS on the chemical reactivity of $C_3S$ and unravel the molecular interaction at the interface between $C_3S$ and CNS during hydration[67]. Figures 9a-g shows the molecular structure evolution processes for the $C_3S$/water system (shown in

Fig.3c) and Figs. 9h-n shows the molecular structure evolution processes for the $C_3S$/water/CNS chains system (shown in Fig.3d). The snapshots of the microstructure configurations are illustrated at simulation time of 0ps, 1ps, 10ps, 100ps, 1ns, 2ns and 3ns, respectively. The hydration progress of $C_3S$ in the presence of CNS/water solution can be described by the following four processes taking place at the $C_3S$/CNS interface: water dissociation → CNS chain dissolution → proton hopping → silicate oligomerization. These interfacial chemical reactions may occur in sequence, in parallel, or in complex combination during the early hydration period. These processes are discussed in detail in the following sections.

***Interaction of $C_3S$ with water.*** For the $C_3S$/water system without the CNS chains, the water hydrolysis is observed at the solid-liquid interface immediately after the onset of the nanocomposite system relaxation. Some water molecules are dissociated into hydroxyl group ($OH^-$) and hydrogen proton ($H^+$) without the formation of hydronium ion($H_3O^+$). This leads to instant surface hydration due to the high reactivity of the dry state of the $C_3S$ crystal (Figs.9o-p). This rapid water dissociation further demonstrates the strong hydrophilic nature of the $C_3S$ surface and its susceptibility to attacks by the protons and OH groups to form hydration products. There is a large amount of ionic oxygen anions and under-coordinated calcium cations congregated at the bare surface of $C_3S$, which can interact with the OH group and $H^+$ proton resulting from water dissociation. This results in $C_3S$ surface hydroxylation[68]. However, after the occurrence of initial rapid hydration of the exposed surface, the further hydration of the $C_3S$ crystal seemingly enters a dormant period (or induction period) at a medium time scale, in which the reaction drastically decelerates and reaches a steady state regime. The reactive surface transformed into a stable ice-like monolayer and further hydration is retarded with barely nucleated calcium hydroxides at the $C_3S$/water interface, shown as the green layer in Figs.9a-g. No silicate oligomerization can be observed within the current simulation time. This is in good agreement with previous findings, which pinpoint a water tessellation/patterning effect for the well-organized surface configuration[49].

***Interaction of $C_3S$/CNS chains with water.*** The initial rapid $C_3S$ surface hydroxylation also happens for the nanocomposite systems at the $C_3S$/CNS interface. However, different from the phenomenon observed during the reaction of $C_3S$ with water, the initial regular steric arrangement of $C_3S$ is highly disturbed at the $C_3S$/CNS interface. The basal structure of $C_3S$ gradually loses its crystalline order with nucleation of a disordered intermediate calcium hydro silicates at the surface. The calcium hydro

silicate is an intermediate phase (termed as product B defined by Taylor in literature[69]). It includes a combination of the calcium hydroxide and hydrated silicate monomers (Q0 species) that are the main component for nucleation of C-S-H. The Formation of the final C-S-H product requires the condensation of silicate tetrahedra forming dimers or longer chains at later hydration stage. The calcium atoms are desorbing from the bulk crystal and diffusing toward the aqueous solution due to the affinity of the CNS chains, which yields a larger amount of calcium hydro silicates at the $C_3S$/CNS interface, shown as the green layer in Figs.9h-n. In the meantime, the hydroxylated silicate tetrahedra are subjected to position rearrangement leading to a more amorphous surface. During the continuous interaction, it is intriguingly found that the highly reactive $C_3S$ surface can disrupt the original stability of the proximate CNS chain when is lying closely to the $C_3S$ substrate surface (<5Å), which results in the bond-breakage and dissolution of the CNS material. Furthermore, the surficial alkaline $Ca^{2+}$ ions with divalent charge diffusing away from the $C_3S$ bulk can strongly attract the Oc, Oh atoms from CNS, which facilitates the formation of Ca-O pairs with a final coordination shell at 2.45Å as shown in the RDF pattern in Fig.10a. This strong Ca attraction also causes the CNS ring opening and the C-O-C glycosidic bond stretching until breakage. Together with the Ow from water, a spatial 3-D Ca-O coordination network is gradually produced at the solid-liquid interface. Subsequently, the bonds in the CNS chain are frequently broken and the carbon atoms from the broken CNS backbone are concurrently reacting, and reassembling with the surrounding oxygen and hydrogen atoms. This results in generation of many C-OH, C-H fragments and creates suspension of mixed organic chemical compounds spreading over the aqueous solution such as Methanol $CH_3OH$, ethanol $CH_2CHOH$ as well as their derivatives Methanediol $CH_2(OH)_2$, ethynediol $C_2H_2O_2$, etc. (See Figs.9q-t). Furthermore, the CNS functional group deprotonation is prevailing during the CNS chain dissolution.

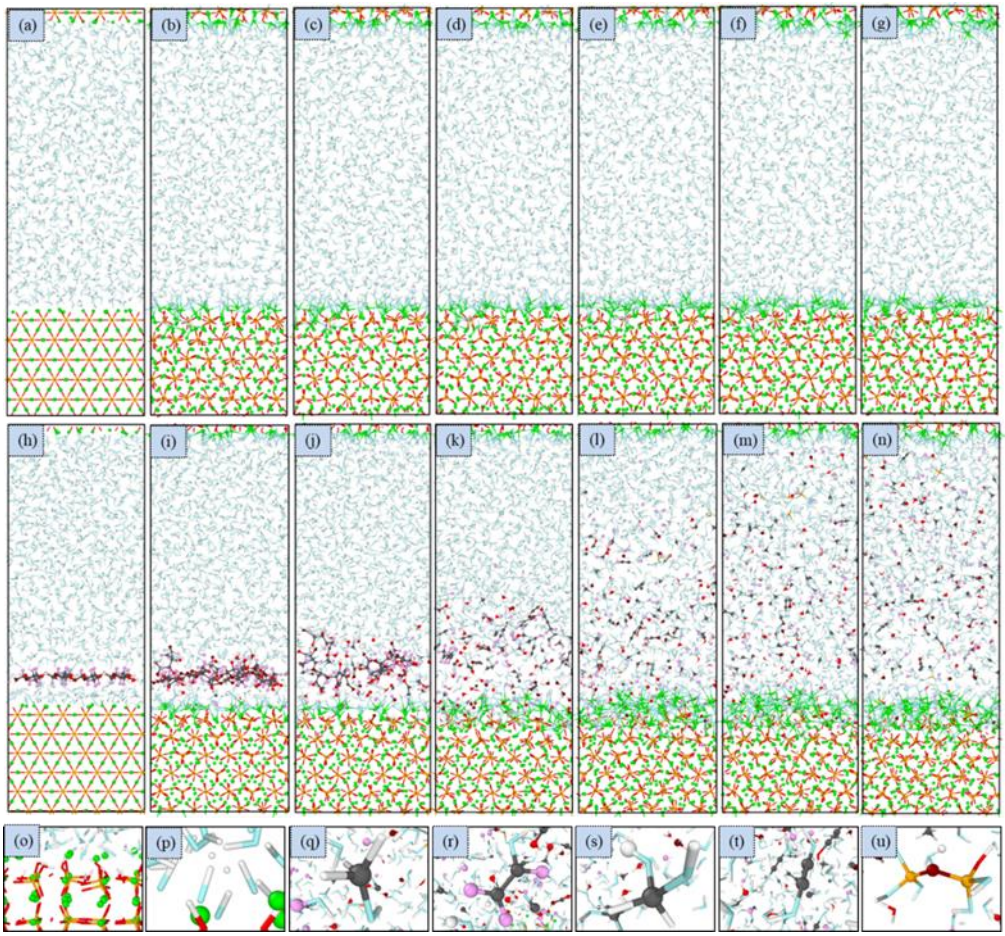


Figure 9 Comparison of microstructure evolution of the composite (a-g) $C_3S$/water system and (h-n) $C_3S$/water/CNS chains system. (o-p) Snapshots representing the water dissociation and fast surface hydroxilation. (q-t) CNS dissolution and functional group deprotonation accompanied by production of organic chemical compounds. (u) Oligomerization of orthosilicate originated from the diffused silicon atoms in the aqueous solution.

The H protons from CNS can be transferred to the dissociated water hydroxyl group ($OH^-$) leading to the composition of new water molecules or connected to the Ot or Od oxygen atoms to further hydroxylate the $C_3S$ substrate surface. The corresponding RDF patterns between the $H_{CNS}$ - $O_{C3S}$ as well as $H_{CNS}$ - $O_{water}$ are given in Figs.10b-c. As shown, distinct RDF peaks of O-H around 1Å demonstrate the protonation of $C_3S$ oxygen and the formation of recombined water molecules seeded from the CNS. Figures 10b-c indicate that the $H_{CNS}$ protons are mostly connecting to the $O_d$ atoms in the $C_3S$. This is in line with the DFT observation that the $O_d$ atoms having higher HOMO orbital intensity are more susceptible to react with the environmental electrophiles. In addition, some silicate tetrahedra start to dissolve with the silicon and oxygen atoms escaping from the $C_3S$ substrate surface and diffuse into the solution. The diffused silicon atoms covalently rebond with the environmental oxygen atoms that produce silicate monomer or dimer (Fig.9u).

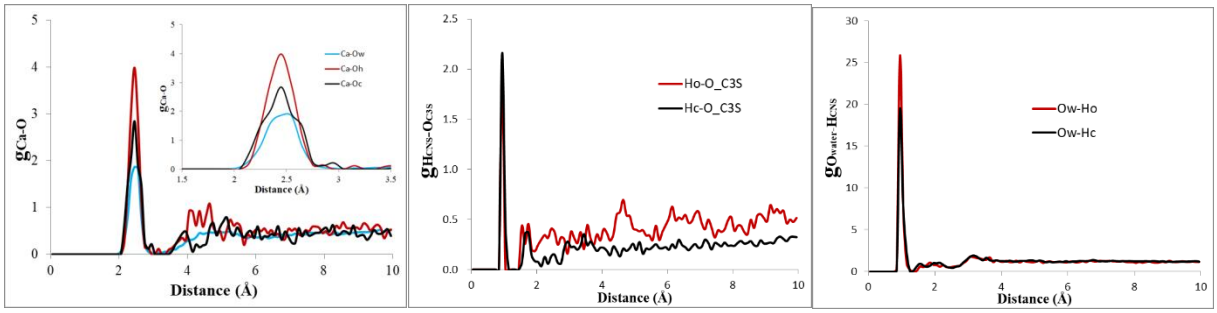


(a) Ca-O (b) $O_{C3S}$- $H_{CNS}$ (c) $O_{water}$-$H_{CNS}$

Fig.10 RDF patterns within $C_3S$/water/CNS chains molecular systems

As discussed above, the $C_3S$ will be hydroxylated and dissolved upon contacting with water, the intermediate calcium hydro silicate phase containing hydrated silicate monomers is forming following the reaction formulation below, which is consistent with the available experimental evidences probed by the $^{29}Si$ NMR test[70,71]:

$$Ca_3SiO_5 + 3H_2O \rightarrow 3Ca^{2+} + H_2SiO_4^{2-} + 4OH^- \quad (2)$$

The oxygen of $C_3S$ can simultaneously connect with the H atoms from the CNS functional groups' deprotonation (H can be Hw, Ho and Hc) and the resulting hydrolysis and hydration equilibriums with respect to the silicic acid species are coexisting during the reaction process described by the following equations[72,73]:

$$O^{2-} + H^+ \Leftrightarrow OH^- \quad (3)$$

$$H_2SiO_4^{2-} + H_2O \Leftrightarrow H_3SiO_4^- + OH^- \quad (4)$$

After initial reaction, the solution is then quickly becoming supersaturated with calcium hydro silicate that has less solubility than $C_3S$. The C-S-H will then precipitate when the supersaturation degree reaches the threshold, which usually occur at longer time scale (from few seconds to hours) [69,74]:

$$nCa^{2+} + 2(n\text{-}1)OH^- + H_2SiO_4^{2-} \rightarrow CaO_n \cdot SiO_2 \cdot H_2O \quad (5)$$

Since not all the calcium ions are consumed during the precipitation of C-S-H, increasing concentration of calcium and hydroxide ions in solution would lead to the maximum supersaturation of the liquid phase which precipitates portlandite, according to the reaction equation：

$$Ca^{2+} + 2OH^- \rightarrow Ca(OH)_2 \quad (6)$$

where the OH group can be sourced from water dissociation or CNS hydroxyl functional group. As the above reactions proceed, substantial H protons continuously penetrate into the crystal further beneath the surface, protonating free oxygen atoms inside the $C_3S$ structure and break the calcium bonds within the crystal framework. The steady-state reactions of CNS/$C_3S$ system is primarily governed by the Grotthuss-type proton hopping mechanism. The H proton jumps from the CNS hydroxyl groups in the hydrated surface towards the inner oxygen atoms, leaving the deprotonated

oxygen atoms free for posterior proton transportation, as shown in Fig.11. Another possible penetration pathway is the H proton exchange between the upper layer orthosilicate t the and deeper layer silicate tetrahedra.

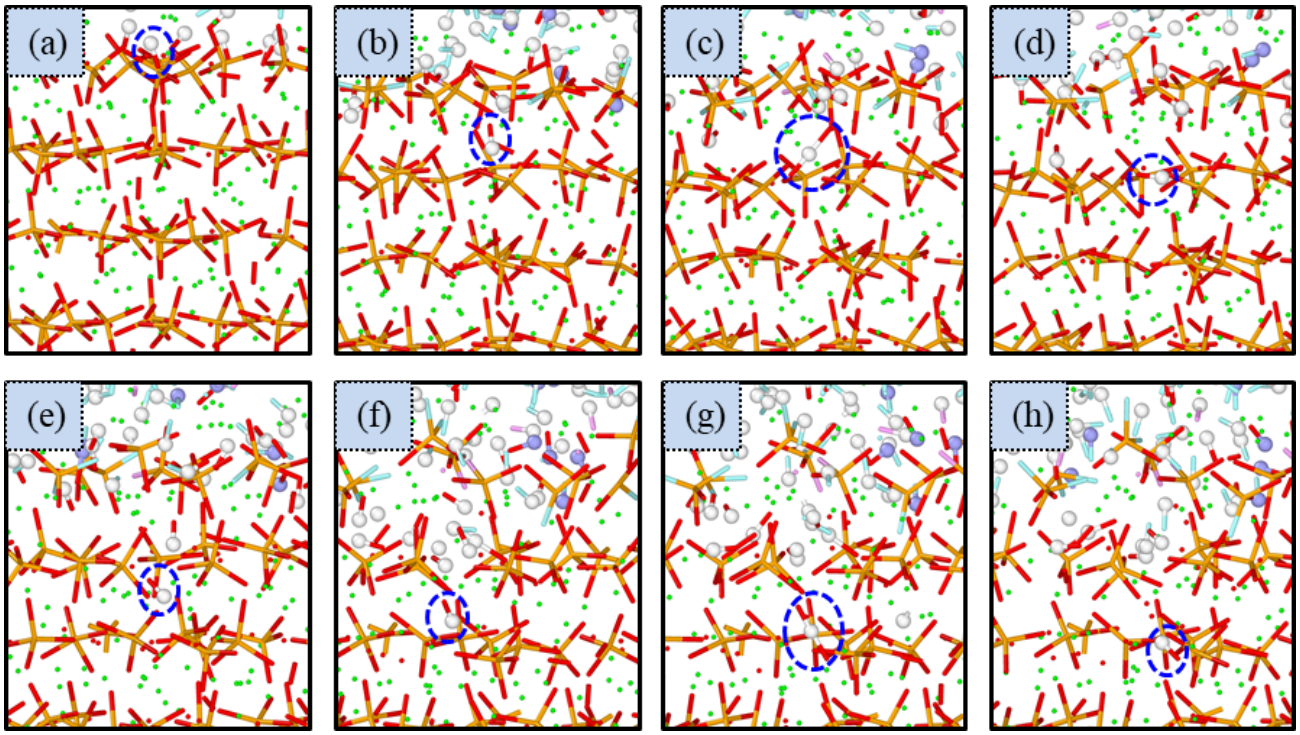


**Fig.11** Snapshots of the proton hopping process. (a) Hydroxylation of $C_3S$ surface after water dissociation. (b) Rotation of hydroxyl group that is pointing towards the second layer silicate tetrahedron. (c) Hydrogen bond formed between the $OH^-$ group and neighboring ionic oxygen. (d) Grotthuss-type proton hopping from the $OH^-$ group towards the inner oxygen with formation of new hydroxyl pair. (e) Rotation of the new hydroxyl pair. (f) Vibration of the new hydroxyl pair pointing towards the third silicate tetrahedral layer with saturation of $OH^-$ groups at the second layer. (g) Dissociation of the $OH^-$ group and protonation of deeper oxygen atom. (h) Proton jumping once again leading to third layer hydroxylation. The proton from water dissociation is depicted using a white ball for clear illustration.

Due to the presence CNS in the aqueous environment, the H protons from the deprotonated functional groups (Hc,Ho) also contribute to the hydroxylation of the $C_3S$. As a result, a noticeable increase in the hydration depth is noticed as compared to the $C_3S$/water system. One reason for the improved hydration rate is the enhanced water dynamics after the inclusion of CNS. As shown in Fig.12a, the mean squared displacement (MSD) of Hw atoms from water is remarkably increased due to both the "water repelling effect" from the chemical solvent byproducts and the released fracture energy from the CNS chains breaking. The high increase in water dynamics implies that the CNS material can accelerate the diffusion capacity of the water molecules and their deep penetration into the interior core structure of $C_3S$. This further contributes to the hydration degree of $C_3S$. Another reason for the

enhanced hydration rate is the enriched H protons and hydroxide ions decomposed from CNS. These protons enable the ionic exchange to take place during hydration. As a result, substantial increase in the calcium hydro silicate precipitates can be observed at the end of the simulation (Fig.9n).

Figure 12b shows the amount of penetrated H protons associated with Od and Ot species in the $C_3S$ crystal for the $C_3S$/water system. The OH density evolution is mainly due to the hydroxylation associated with the dangling Od atoms. The OH density is steadily increased over time reaching about 7 $OH^-/nm^2$ when initial instant hydroxylation occurred at the first couple of picoseconds. However, a plateau is observed for the OH density evolution associated with the tetrahedral Ot atoms that contribute a hydroxyl density of ≈2 $OH^-/nm^2$.

For the $C_3S$/water/CNS chains system, the effect of CNS on the hydration kinetics is evident as shown in Fig.12c. Here, we see that the inclusion of CNS chains can significantly improve the Od-Hw density within the same simulation time. In addition, the H atoms from the CNS also make discernable contribution to the hydroxylation, where the OH density increases at the beginning, followed by a notable curve oscillation, particularly in the case of Od-Hc density evolution. This implies that significant proton exchange phenomenon takes place during the hydration process. Figure12d compares the total OH density for $C_3S$/water and $C_3S$/water/CNS chains molecular systems. The total OH density of the $C_3S$/water/CNS chains system reaches ≈12 $OH^-/nm^2$ at the end of simulation which is significantly larger than that of $C_3S$/water (≈9 $OH^-/nm^2$), confirming that the inclusion of CNS chains can urge the proton exchange reaction.

The $C_3S$ hydration depth evolution is computed by the time-resolved atomic density profiles (TRDP) with the ultimate atom density distribution along the direction perpendicular to [0 1 0] surface for given Ca, O, H species shown in Fig.13. The evolution of H density is much more evident for the $C_3S$/water/CNS chains system where the hydration depth reaches up to ≈15 Å which higher that than of the $C_3S$/water (≈12 Å). It is also noteworthy that some oxygen atoms from the CNS dissolution can migrate into the interstitial site beneath the $C_3S$ surface, evidenced by the black dash line in Fig.13b. As discussed above, the VB PDOS in pure $C_3S$ is mostly from the O-2p orbitals with the HOMO density mainly accumulated around the dangling ionic oxygen atoms. Those "oxygen migrants" are ionic in nature can contribute to the TVB which could enhance the hydration reactivity of $C_3S$ and therefore facilitate the proton hopping.

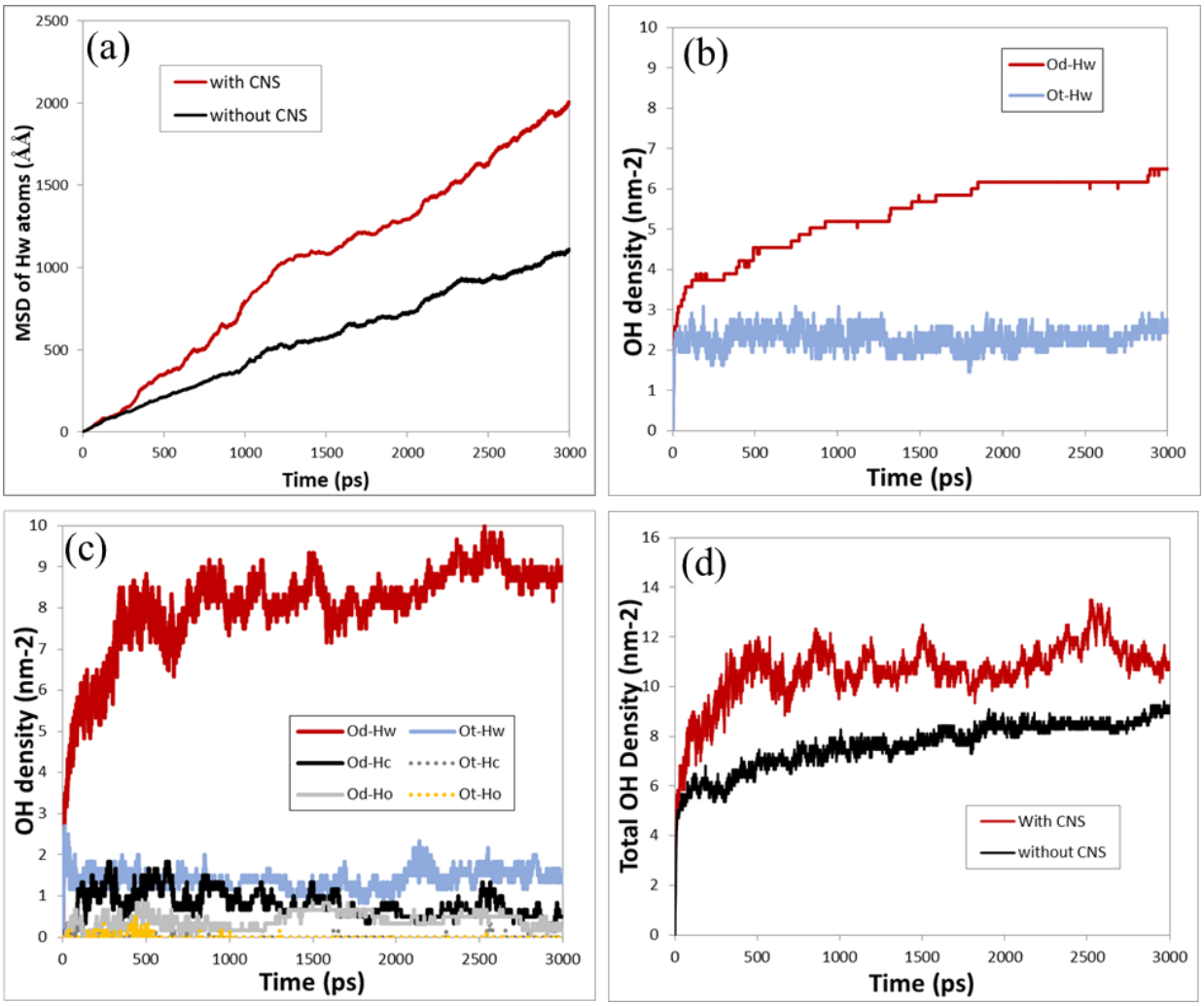


**Fig.12** Features of H proton during microstructural evolution. (a) Comparison of MSD evolutions of water hydrogen atoms between systems with and without CNS. (b) Number evolution of hydroxyl groups per unit of exposed surface with respect to time for $C_3S$ contacting with bulk water. (c) Contribution of different H proton types associated with different oxygen species for nanocomposite system. (d) Comparison of OH density for systems with and without CNS

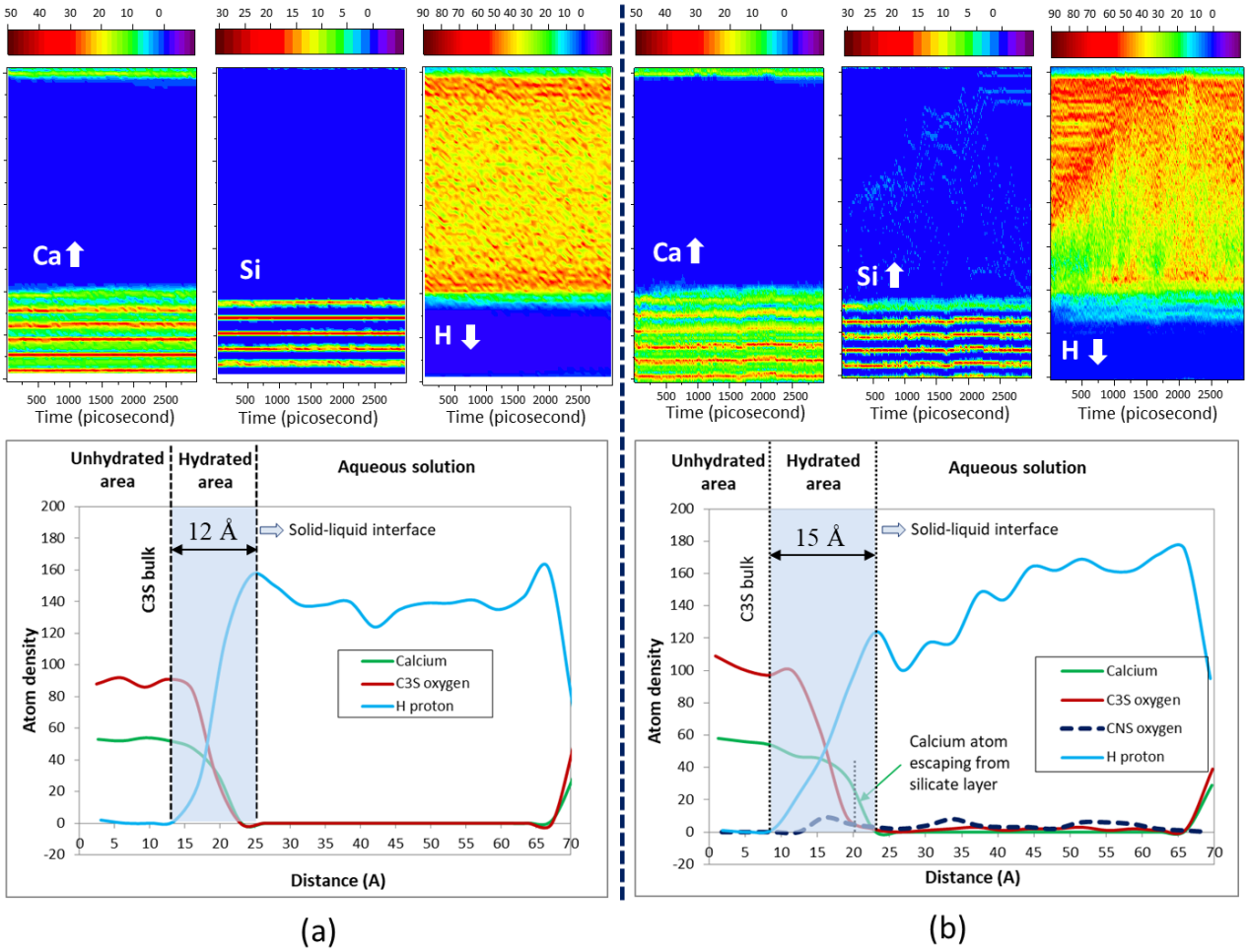


**Fig.13** TRDP and eventual atom intensity profile by the end of simulation for given Ca, O, H species for molecular systems (a) without CNS, and (b) with CNS inclusion.

With further reaction, the evolved molecular structure of the $C_3S$/water/CNS chains system shows that some silicon and oxygen atoms are released from the $C_3S$ bulk matrix and diffused into the solution, causing a more defective surface with an etch pit activation mechanism[27]. The silicate monomers start to polymerize in the $C_3S$/water/CNS chains system, resulting in formation of paired silicate tetrahedral (dimer) (see Fig.9u) or silicate trimer anions around the etch pit area near the surface, following the reaction below[75]:

$$SiO_4^{4-} + HSiO_4^{3-} \Leftrightarrow [\equiv O_3Si\text{-}O\text{-}SiO_3 \equiv]^{6-} + HO^- \tag{7}$$

$$[\equiv O_3Si\text{-}O\text{-}SiO_3 \equiv]^{6-} + HSiO_4^{3-} + H_2O + 2H^+ \Leftrightarrow \left[\equiv O_3Si\text{-}O\text{-}\underset{\displaystyle O}{\overset{\displaystyle O}{\overset{|}{\underset{|}{Si}}}}\text{-}O\text{-}Si(OH)_3\right]^{5-} + 2OH^- \tag{8}$$

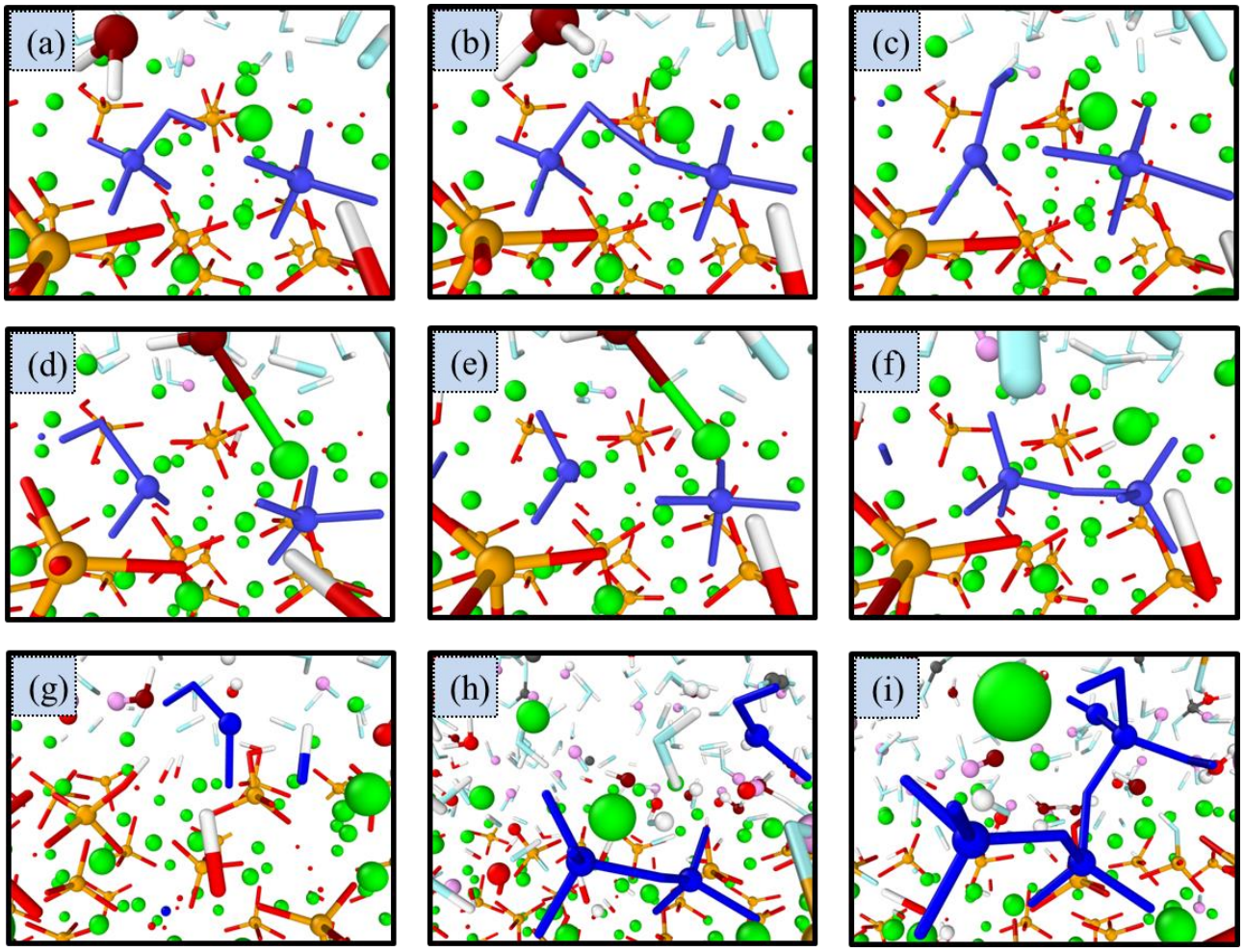


**Fig.14** Snapshot of silicate oligomerization pathway: It starts with two independent silicate tetrahedral monomers(a), the hydrogen atom may be connected by the neighboring oxygen atoms during relaxation(b), the electronegativity is reduced for the hydrogen orthosilicate ion ($HO_4Si^{3-}$), leading to the dissolution of this unstable silicic acid to metasilicate ion($HO_3Si^{-}$), where the tetrahedral oxygen atoms are strongly attracted by the adjacent calcium cation and migrated into the interstitial site at the defective region(c), the hydrogen is then pointing towards the diffused dangling oxygen due to the higher reactivity nature of Od site(d), followed by proton jumping in formation of hydroxyl group (e), with eventual oligomerization into paired silicate tetrahedra(f). Dissolution of hydrogen orthosilicate ion ($HO_4Si^{3-}$) again with the tetrahedral oxygen diffused into the interstitial site and form hydroxyl group with penetrated proton (g). Diffusion of the Si(OH)O cation to the adjacent silicate dimer(h). Oligomerization of silicate trimer (i). The silicate tetrahedral is marked as blue.

Figure14 shows one possible mechanism for the silicate oligomerization during hydration as obtained from the MD simulations. The atoms and bonds are highlighted in blue for better illustration. As previously mentioned, some silicate tetrahedra at the $C_3S$ substrate surface will dissolve and diffuse into the aqueous solution due to the attraction from the CNS material. The diffused silicate atoms in the aqueous solution are also linked to the hydroxide ions to form orthosilicate $Si(OH)_4$. It is noticed that the reaction is reversible for the oligomerization of silicate monomers, i.e.

$$Si(OH)_4 + Si(OH)_4 \Leftrightarrow (HO)_3SiOSi(OH)_3 + H_2O \quad (9)$$

The condensed water molecules can be dissociated once again for further proton hopping and hydration. The polymerization of $Q^1$ and $Q^2$ species ($Q^n$ refers to silicon atoms that are covalently bonded via bridging oxygen atoms to other n silicon atoms with $0<n<4$) of silicates with formation of short chains is an explicit signal of C-S-H precipitation in the vicinity of surface. However, we have to omit the simulation of the growth of C-S-H that is usually occurring at a much longer time scales, as it can be very challenging to simulate the growth of C-S-H using the reactive force field due to high computational cost. It is worth noting that silicic polymerization and nucleation of C-S-H ellipsoid particle has been successfully achieved by a sol-gel MD simulation via an empirical Feuston–Garofalini (FG) potential[76,77]. Based on the current study, we believe that further hydration events (such as deposition of oligomeric C-S-H nanoscale colloidal cluster) for $C_3S$ interacting with CNS at longer time scales can be described by using a more efficient empirical force field or a coarse-grained model.

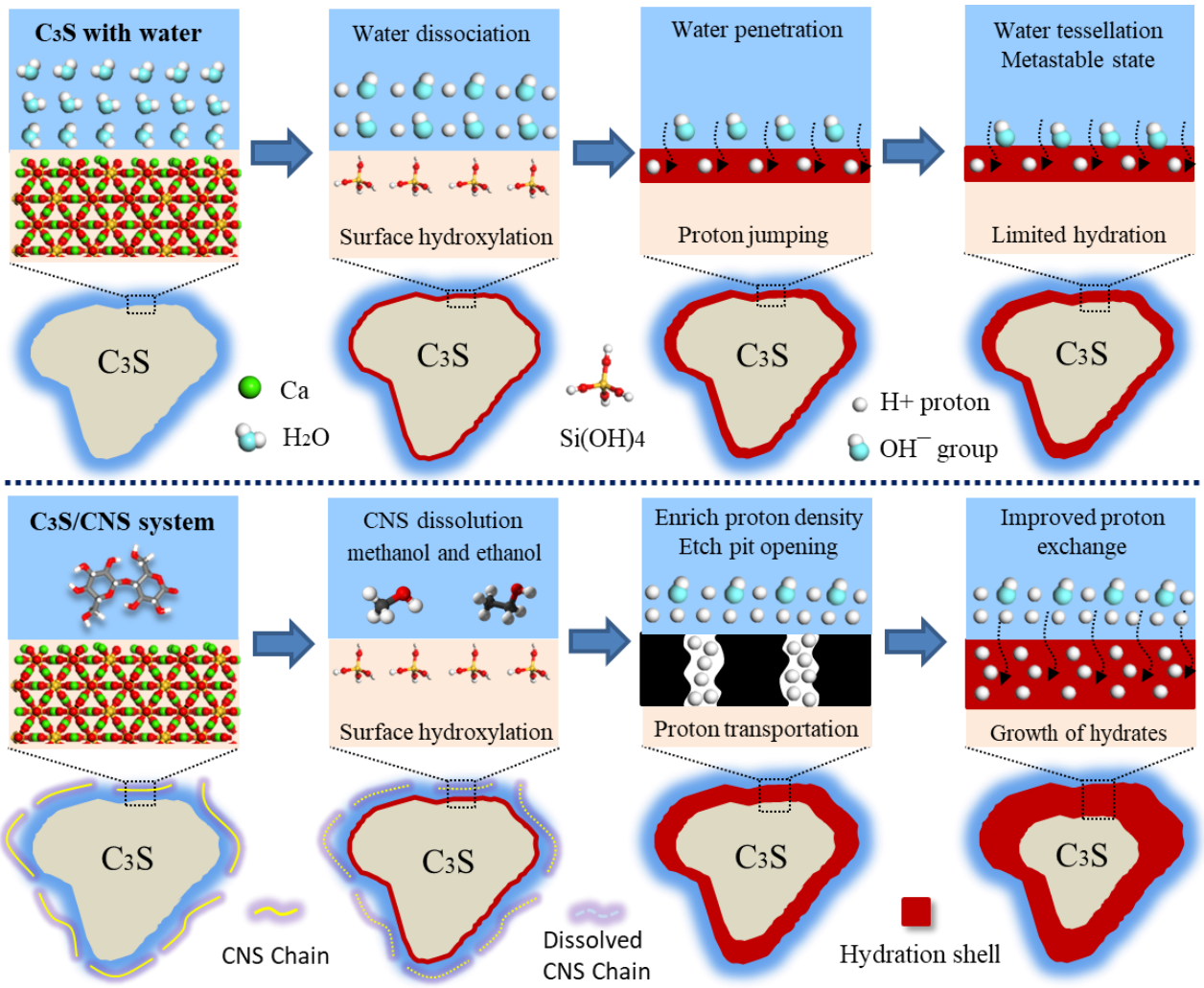

Fig.15 Schematic diagram the improved hydration after inclusion of CNS chain

The MD-DFT simulations conducted in this study uncovered new mechanisms underpinning the improved hydration of $C_3S$, the main phase of OPC. In summary that the presence of CNS chains in the vicinity of the cement particle tend to dissolve and promote the water dynamics. This bursts the energetic barrier for further $C_3S$ hydration, as schematically shown in Fig.15. As such, the CNS is acting like a reservoir transporting the water molecules from the aqueous solution to the inside of substrate species, which increases the thickness of the hydration shell of cement particles.

### 3.4 Experimental results

*3.4.1 TGA/DTG/DSC results*

The following experimental characterizations were carried out to further understand the effect of various CNS concentrations on the hydration of cement pastes. Fig.16a shows the TGA results for the cementitious composites containing different CNSs with weight percentage ranging from 0.1 wt% to 0.4 wt%. The results indicate that the C-S-H and aluminate phase (e.g. ettringite) gradually lose bound water in the temperature range between 140 and 300 °C. The dehydroxylation of $Ca(OH)_2$ happens between 420 and 480 °C and the calcium carbonate ($CaCO_3$) decarbonation process occurs between 600 and 780 °C. The amount of mass loss increases with an increase in the concentration of CNSs. The final weight of the controlled specimen is fixed at 85.85%, while the cementitious nanocomposites with 0.1, 0.2 and 0.4 wt% CNSs are burned 0.16, 0.44 and 0.76% more, respectively in comparison to the controlled specimen.

The abovementioned thermogravimetric mass loss is directly related to the degree of hydration (DOH). According to the hydration empirical formula of T.C Powers[2], the content of bound water can be calculated from the weight difference before and after the cement thermogravimetric experiment. DOH is then calculated by dividing the mass of chemically bound water (CBW) to the remaining weight of the experiment and 0.23, given as[78]:

$$\mathrm{DOH(TGA)} = \frac{m(\mathrm{CBW})}{m(\mathrm{remain})} / 0.23 \tag{10}$$

Fig.16b shows the 28-d DOH and the percentage of portlandite for the cementitious nanocomposite with increasing CNS concentrations. It can be seen from the blue line that the DOH increases as the amount of CNS concentration increases. In comparison to the plain specimen, the DOH for the nanocomposite containing 0.1, 0.2 and 0.4wt% CNS is increased by 1.35%, 3.71% and 6.30%,

respectively. The phenomenon of the improved DOH is consisting with the finding from the MD simulations that the CNS enables the water molecules to penetrate deeper into the interior microstructure of the clinker.

Fig.16c illustrates the Derivative Thermogravimetry (DTG) curves after 28 days of curing. The curves show that the nanocomposites with or without CNSs decompose and degrade in the same temperature range. The peaks in the DTG chart shows that the specific C-S-H, $Ca(OH)_2$ and $CaCO_3$ phases decompose quickly in the temperature ranges 140-300℃, 420-480℃ and 600-780℃. In comparison to the controlled specimen, the addition of CNSs increases the peaks, implying that there are more hydration products decomposed at the same temperature.

Figures16d-e show the DSC thermogram of CNS reinforced cementitious nanocomposite along with the enthalpy of fusion of portlandite crystals in the temperature range 20 - 900 °C. By calculating the relationship between heat flow and time, the heat absorbed/released by the crystal decomposition of the cementitious composite can be obtained within a temperature range (see Fig.16d). As shown in Fig.16d, the first endothermic progress occurs between 140 and 400 °C. This process occurs due to the loss of chemically bound water in the C-S-H crystal and aluminate phase (e.g. ettringite) during their heat absorption. The second endothermic peak occurs between 420 to 480 °C, corresponding to the phenomenon of the microcrystalline $Ca(OH)_2$ containing the embedded CNSs decomposition [79]. As a result, $Ca(OH)_2$ is thermally decomposed together with the pyrolysis of the attached CNS cellulose body. The following endothermic peak is located between 600 and 800 °C, where the decomposition of $CaCO_3$ is dominant.

The DSC endothermic peak position in Fig.16d matches the DTG degradation position in Fig.16c. Taking the pyrolysis process of Portlandite as an example, the thermogravimetric loss in the temperature range 420-480°C is considered as the dihydroxylation of $Ca(OH)_2$. Once again, it is noted from the black line in Fig.16b that the content of Portlandite is increased by 4.16%， 9.49% and 19.73% at CNS concentrations between 0 and 0.4wt%. These results are similar to the enthalpy of fusion for the cementitious composite with CNSs which are increased by 3.73%， 8.52% and 16.54% respectively as shown in Fig.16e. The experiment result again confirm that CNS accelerates the DOH, thus generating denser hydration products.

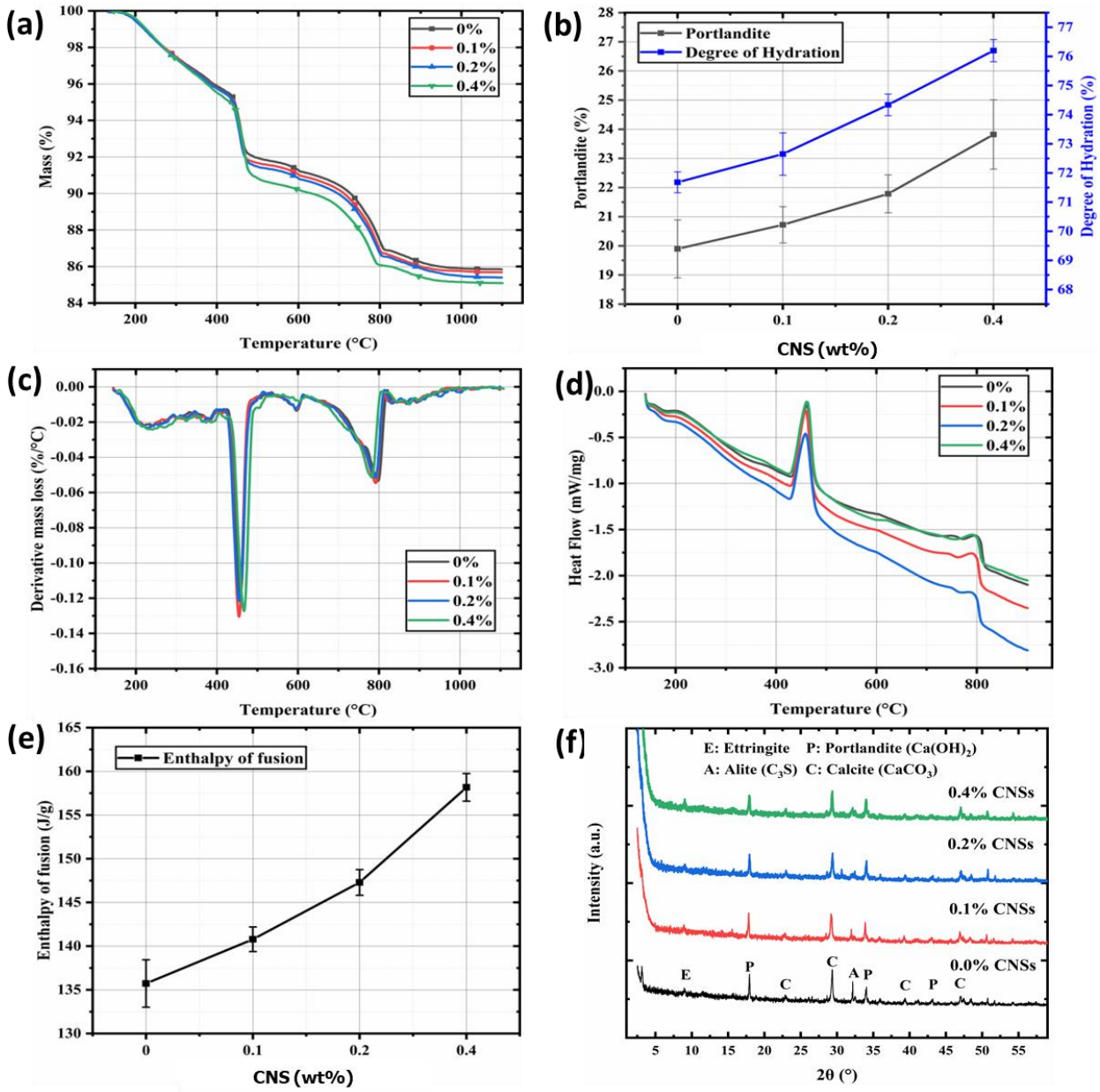


**Fig.16** experimental results of hydration reactivity of the cementitious nanocomposite with CNS concentrations from 0 to 0.4wt%.(a) 28-d TGA results of the cementitious nanocomposite.(b) 28-d DOH and percentage of portlandite.(c) 28-d DTG results.(d) 28-days DSC results.(e) 28-d Portlandite enthalpy of fusion. (f) XRD patterns.

*3.4.2 XRD/SEM/TEM results*

Fig.16f shows the 28-d XRD patterns of the cementitious composites with CNSs concentrations of 0.00, 0.10, 0.20 and 0.40wt%. Through the analysis of CrysAlisPro software phase fitting and Rietveld refinement techniques, all the samples show similar hydration phases including ettringite (AFt), calcium hydroxide ($Ca(OH)_2$), unhydrated tricalcium silicate ($C_3S$) and calcium carbonate ($CaCO_3$). The results clearly indicate that the incorporation of CNS does not change the type and structure of the hydration product. From fig.16f we can see that the Ettringite intensity peaks at 9°

and 15° are stronger in the CNS cement composite than those in the plain cement composite. Furthermore, intensity of $Ca(OH)_2$ at 17.5° in the CSN cement composite is similar to that in the plain cement composite. However, the CNS cement specimen shows a significant increase in $Ca(OH)_2$ at 34°. We quantitatively identified that as the CNS concentration increases, ettringite, $Ca(OH)_2$ and other crystals intensity continue to increase, whereas the intensity of unhydrated phases tricalcium silicate and calcium carbonate decrease (e.g. the intensity peak of $C_3S$ phase decreases). However, due to the nature of C-S-H gel semi-crystalline, it is difficult to analyze its crystallization by XRD. But from the combined XRD, TGA, DTG and DSC results, it is reasonable to state that the addition of CNSs amplify the growth of C-S-H. The characteristic peaks of CNS are not detected by XRD, because some of CNSs are dissolved during their interaction with the cement particles and some are embedded in the hydrate phases. This support the findings of the MD simulations. The MD simulations show that the acidic hydroxyl (-OH) / hydroxymethyl ($-CH_2$-OH) functional groups on the surface of CNS are partially weakened/dissolved in the cement alkaline environment (pH = 11.7) at the CNS/cement interface and react with the surface calcium and oxygen atoms. This series of interaction facilitate the Ca $(OH)_2$ precipitation and the C-S-H formation.

Figures 17a-b shows typical 28-day SEM images of the cementitious composites. Figure 17b indicates that the addition of 0.40 wt% NCS can tolerate the crystallization and the morphology of hydration products of the cement paste at 28 days. The microstructure of the cement paste without CNS (Fig.17a) mainly contains partially unhydrated cement particles, $Ca(OH)_2$, a small amount of C-S-H and microcracks. This could be attributed to lower DOH. In contrast, the microstructure of the nanocomposite containing 0.40-wt% CNS (Fig.17b) mainly includes CNSs that are embedded into the C-S-H gel and the calcium hydroxide needles. The microstructure of the nanocomposite containing CNS showed a compact microstructure with condensed hydration products and without micro-cracks. This can be attributed to the fact that the CNS sheets are encapsulated by the dense C-S-H gels during the hydration, resulting in intercalated nanocomposites.

Figures 17c-d show the 28-day microstructure TEM micrographs of the cementitious composites. Figure.17c shows that the microstructure of the plain paste is composed of lower contents of C-S-H and Ca $(OH)_2$ crystals. Fig.17d shows the microstructure of the cement paste with 0.40% wt CNS where fabric-like CNSs crystals are highly transparent. The combination of CNSs and hydration products enhances the aggregation of matrix C-S-H and $Ca(OH)_2$ crystals to form a denser

microstructure. The Fig.17e-f show the 28-day EDS of plain and CSNs reinforced cement pastes. The EDS results indicate that the oxygen spectroscopy of CNS reinforced cementitious composite is denser than that of the plain cement paste. A small amount of partial agglomeration can be observed based on the oxygen spectrum for the CNS specimen, which further confirms the generation of hydration products. The incorporation of CNS contributed to the formation and agglomeration of cementitious composites C-S-H and $Ca(OH)_2$ hydration products. The TEM and EDS images confirm the findings from TGA, XRD and SEM results that the CNSs facilitate the hydration of the cement thereby increasing the content of C-S-H and $Ca(OH)_2$ in the cementitious composite. It is north noting that the CNS cannot be seen in the SEM and TEM images. Again, the stacked CNSs can be partially dissolved as a result of interaction with $C_3S$. This again supports the dissolution mechanism of CNS uncovered by the MD simulations. Furthermore, the remaining stacked CNSs are fully embedded in the hydrate phases thus cannot be detected by SEM and TEM.

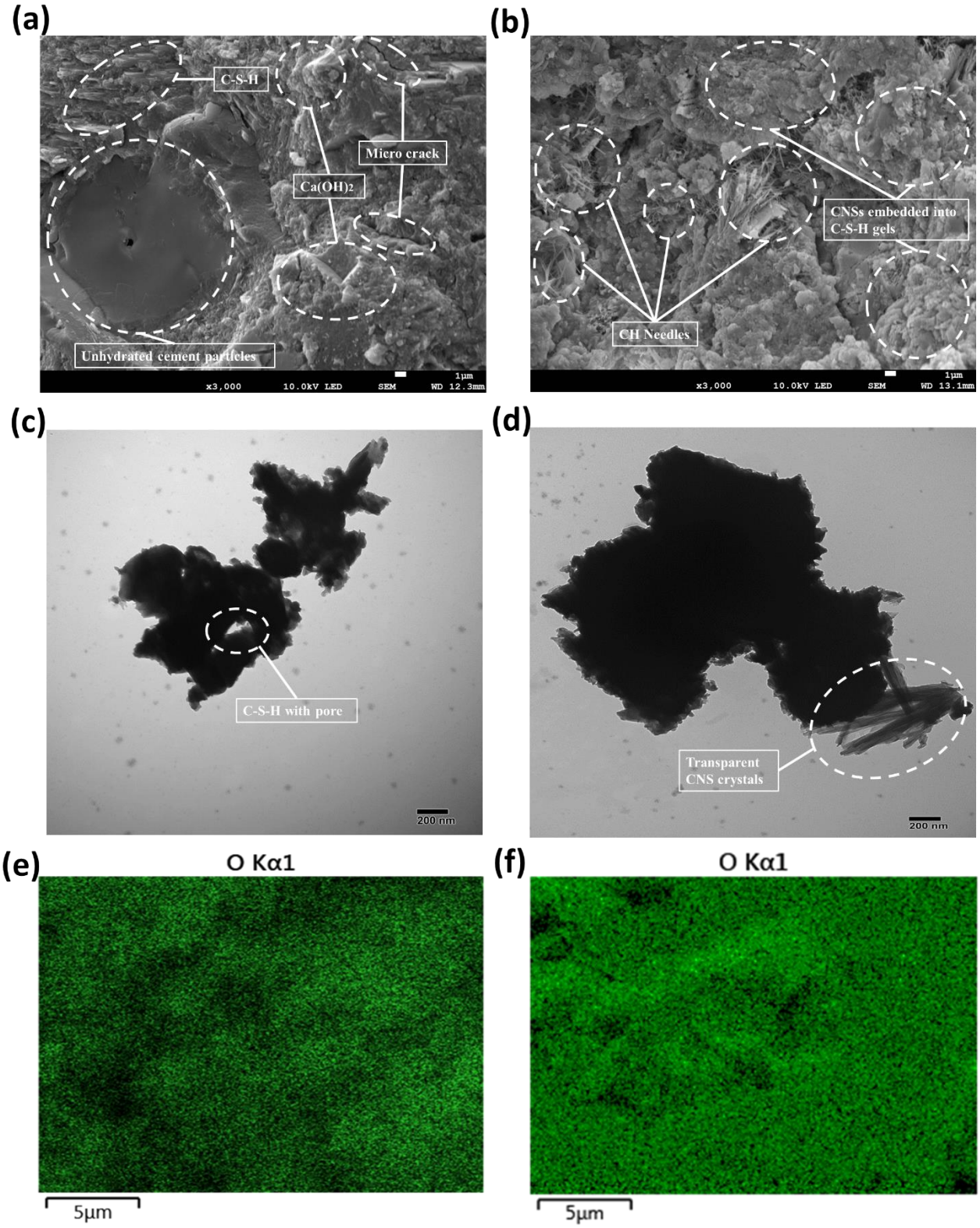


**Fig.17** SEM and (TEM) images of CNSs cementitious composite: (a) SEM of cement paste without CNS, (b) SEM of nanocomposite with 0.4wt% CNS (c) TEM of cement paste without CNS, (d) TEM of nanocomposite with 0.4wt% CNS, (e) EDS of cement paste without CNS, (f) EDS of nanocomposite with 0.4wt% CNS.

## 4 Conclusions and Future Work

Using a combination of DFT-MD simulations and experimental characterization, we have demonstrated that the addition of 2D CNS material can remarkably improve the growth of the hydrate products of OPC. The following conclusions can be drawn from this study:

- The DFT-MD simulations show that during the hydration process, the CNS chains in contact with the $C_3S$ surface dissolve, leading to the formation of many organic chemical compounds. These chemical compounds mitigate the water tessellation effect at the CNS/$C_3S$ interface. This increases the dynamics of water molecules in the aqueous solution and promote higher OPC hydration depth, thus more hydrate products are developed. The increased hydration depth is also due to the enriched H protons and hydroxide ions decomposed from CNS that is seeding for the proton exchange during hydration.
- During hydration, the $C_3S$ suffers simultaneously nucleophilic and electrophilic attacks from both the CNS and the water molecules. Since the $C_3S$ calcium atom is an electron acceptor, the anions from the water oxygen, CNS backbone oxygen, and the deprotonated CNS functional group oxygen are attracted to $C_3S$. Because of this, the $C_3S$ oxygen atoms act as electron donors that accept $H^+$ protons from water and CNS functional groups, resulting in higher growth of hydration products.
- The experimental results support the key findings from the DFT-MD investigation. The experimental research shows that the addition of CNS increases the degree of hydration of the cement paste. As a result, the growth of the hydrate phases is amplified, leading to the formation of denser C-S-H and $Ca(OH)_2$ products in the cement paste.
- The experimental and DFT-MD simulation results confirm the dissolution of CNS layers that are in the vicinity of $C_3S$ as a result of their interaction with the OPC particles. The CNS layers that are in the distance to the OPC particles remained intact and embedded in the hydrate phases.
- Future work is needed to extend the DFT-MD simulations to the "as produced" CNS with multiple layers to better understand the interaction of these layers with $C_3S$ and predict the resulting degree of hydration. The DFT-MD simulations also need to be carried out over longer time scale to link to the interaction of $C_3S$ with CNS to the growth of C-S-H. Further experimental characterization is needed to characterize the effect of CNS on the hydration depth at multiple length scales using high-throughput analytical characterization tools.

- The research presented herein provides a road map for the development of high performance and low-carbon footprint construction materials through controlled hydration kinetics using green and renewable 2D nanomaterials derived from waste.

## Acknowledgement

This research work is financially supported by the European Commission Horizon 2020 Marie Sklodowska-Curie Research Grant (B-SMART 799658).

Reference


[1] J.W. Bullard, H.M. Jennings, R.A. Livingston, A. Nonat, G.W. Scherer, J.S. Schweitzer, K.L. Scrivener, J.J. Thomas, Mechanisms of cement hydration, Cem. Concr. Res. 41 (2011) 1208–1223. https://doi.org/10.1016/j.cemconres.2010.09.011.

[2] H.F.W. Taylor, Cement chemistry, Thomas Telford, 1997.

[3] K. Scrivener, A. Ouzia, P. Juilland, A.K. Mohamed, Advances in understanding cement hydration mechanisms, Cem. Concr. Res. 124 (2019) 105823.

[4] P.J.M. Monteiro, S.A. Miller, A. Horvath, Towards sustainable concrete, Nat. Mater. 16 (2017) 698–699.

[5] F. Lavergne, R. Belhadi, J. Carriat, A. Ben Fraj, Effect of nano-silica particles on the hydration, the rheology and the strength development of a blended cement paste, Cem. Concr. Compos. 95 (2019) 42–55.

[6] J. Zhou, K. Zheng, Z. Liu, F. He, Chemical effect of nano-alumina on early-age hydration of Portland cement, Cem. Concr. Res. 116 (2019) 159–167.

[7] J. Chen, S. Kou, C. Poon, Hydration and properties of nano-TiO2 blended cement composites, Cem. Concr. Compos. 34 (2012) 642–649.

[8] R. Kalpokaitė-Dičkuvienė, A. Baltušnikas, R. Levinskas, J. Čėsnienė, Incinerator residual ash–metakaolin blended cements: effect on cement hydration and properties, Constr. Build. Mater. 206 (2019) 297–306.

[9] M. Heikal, N.S. Ibrahim, Hydration, microstructure and phase composition of composite cements containing nano-clay, Constr. Build. Mater. 112 (2016) 19–27.

[10] T. Matschei, B. Lothenbach, F.P. Glasser, The role of calcium carbonate in cement hydration, Cem. Concr. Res. 37 (2007) 551–558.

[11] M.S.M. Norhasri, M.S. Hamidah, A.M. Fadzil, Applications of using nano material in concrete: A review, Constr. Build. Mater. 133 (2017) 91–97.

[12] M. Schneider, The cement industry on the way to a low-carbon future, Cem. Concr. Res. 124 (2019) 105792. https://doi.org/10.1016/j.cemconres.2019.105792.

[13] J. Skibsted, R. Snellings, Reactivity of supplementary cementitious materials (SCMs) in cement blends, Cem. Concr. Res. 124 (2019) 105799.

[14] M. Eftekhari, S. Mohammadi, Molecular dynamics simulation of the nonlinear behavior of the CNT-reinforced calcium silicate hydrate (C–S–H) composite, Compos. Part A Appl. Sci. Manuf. 82 (2016) 78–87.

[15] X. Zhu, Y. Gao, Z. Dai, D.J. Corr, S.P. Shah, Effect of interfacial transition zone on the Young's modulus of carbon nanofiber reinforced cement concrete, Cem. Concr. Res. 107 (2018) 49–63.

[16] H. Yang, H. Cui, W. Tang, Z. Li, N. Han, F. Xing, A critical review on research progress of graphene/cement based composites, Compos. Part A Appl. Sci. Manuf. 102 (2017) 273–296.

[17] D. Hou, Z. Lu, X. Li, H. Ma, Z. Li, Reactive molecular dynamics and experimental study of graphene-cement composites: Structure, dynamics and reinforcement mechanisms, Carbon N. Y. 115 (2017) 188–208.

[18] C. Zhou, F. Li, J. Hu, M. Ren, J. Wei, Q. Yu, Enhanced mechanical properties of cement paste by hybrid graphene oxide/carbon nanotubes, Constr. Build. Mater. 134 (2017) 336–345.

[19] D. Fan, L. Lue, S. Yang, Molecular dynamics study of interfacial stress transfer in graphene-oxide cementitious composites, Comput. Mater. Sci. 139 (2017) 56–64.

[20] L. Zhao, X. Guo, L. Song, Y. Song, G. Dai, J. Liu, An intensive review on the role of graphene oxide in cement-based materials, Constr. Build. Mater. 241 (2020) 117939.

[21] M. Birenboim, R. Nadiv, A. Alatawna, M. Buzaglo, G. Schahar, J. Lee, G. Kim, A. Peled, O. Regev, Reinforcement and workability aspects of graphene-oxide-reinforced cement nanocomposites, Compos. Part B Eng. 161 (2019) 68–76.

[22] Y. Chi, B. Huang, M. Saafi, J. Ye, C. Lambert, Carrot-based covalently bonded saccharides as a new 2D material for healing defective calcium-silicate-hydrate in cement: Integrating atomistic computational simulation with experimental studies, Compos. Part B Eng. 199 (2020) 108235.

[23] D. Hepworth, E. Whale, Cellulose platelet compositions, methods of preparing cellulose platelet compositions and products comprising same, US 9,834,664 B2, 2017.

[24] D. Ru, C. Zhu, S. Dong, J. Zhao, Wrinkling behavior of graphene on substrates with different surface morphologies, Mech. Mater. 137 (2019) 103144.

[25] Y. Cao, N. Tian, D. Bahr, P.D. Zavattieri, J. Youngblood, R.J. Moon, J. Weiss, The influence of cellulose nanocrystals on the microstructure of cement paste, Cem. Concr. Compos. 74 (2016) 164–173.

[26] D. Lau, W. Jian, Z. Yu, D. Hui, Nano-engineering of construction materials using molecular dynamics simulations: Prospects and challenges, Compos. Part B Eng. 143 (2018) 282–291. https://doi.org/10.1016/j.compositesb.2018.01.014.

[27] P. Juilland, E. Gallucci, R. Flatt, K. Scrivener, Dissolution theory applied to the induction period in alite hydration, Cem. Concr. Res. 40 (2010) 831–844.

[28] M.-N. De Noirfontaine, F. Dunstetter, M. Courtial, G. Gasecki, M. Signes-Frehel, Polymorphism of tricalcium silicate, the major compound of Portland cement clinker: 2. Modelling alite for Rietveld analysis, an industrial challenge, Cem. Concr. Res. 36 (2006) 54–64.

[29] W.G. Mumme, Crystal structure of tricalcium silicate from a Portland cement clinker and its application to quantitative XRD analysis, Neues Jahrb. Für Mineral. 1995 (1995) 146–160.

[30] R.J. Moon, A. Martini, J. Nairn, J. Simonsen, J. Youngblood, Cellulose nanomaterials review: structure, properties and nanocomposites, Chem. Soc. Rev. 40 (2011) 3941–3994.

[31] Y. Horikawa, J. Sugiyama, Localization of crystalline allomorphs in cellulose microfibril, Biomacromolecules. 10 (2009) 2235–2239.

[32] Y. Nishiyama, P. Langan, H. Chanzy, Crystal structure and hydrogen-bonding system in cellulose Iβ from synchrotron X-ray and neutron fiber diffraction, J. Am. Chem. Soc. 124 (2002) 9074–9082.

[33] Y. Nishiyama, J. Sugiyama, H. Chanzy, P. Langan, Crystal Structure and Hydrogen Bonding System in Cellulose Iα from Synchrotron X-ray and Neutron Fiber Diffraction, J. Am. Chem. Soc. 125 (2003) 14300–14306. https://doi.org/10.1021/ja037055w.

[34] H. Heinz, T.-J. Lin, R. Kishore Mishra, F.S. Emami, Thermodynamically consistent force fields for the assembly of inorganic, organic, and biological nanostructures: the INTERFACE force field, Langmuir. 29 (2013) 1754–1765.

[35] B. Delley, From molecules to solids with the DMol 3 approach, J. Chem. Phys. 113 (2000) 7756–7764.

[36] J.P. Perdew, K. Burke, M. Ernzerhof, Generalized gradient approximation made simple, Phys. Rev. Lett. 77 (1996) 3865.

[37] A.C.T. Van Duin, A. Strachan, S. Stewman, Q. Zhang, X. Xu, W.A. Goddard, ReaxFFSiO reactive force field for silicon and silicon oxide systems, J. Phys. Chem. A. 107 (2003) 3803–3811.

[38] A.C.T. Van Duin, S. Dasgupta, F. Lorant, W.A. Goddard, ReaxFF: a reactive force field for hydrocarbons, J. Phys. Chem. A. 105 (2001) 9396–9409.
[39] S. Plimpton, Fast parallel algorithms for short-range molecular dynamics, J. Comput. Phys. 117 (1995) 1–19.
[40] M.R. Sadat, K. Muralidharan, L. Zhang, Reactive molecular dynamics simulation of the mechanical behavior of sodium aluminosilicate geopolymer and calcium silicate hydrate composites, Comput. Mater. Sci. 150 (2018) 500–509.
[41] D. Fan, S. Yang, Mechanical properties of CSH globules and interfaces by molecular dynamics simulation, Constr. Build. Mater. 176 (2018) 573–582.
[42] J. Jiang, Y. Yan, D. Hou, J. Yu, Understanding the deformation mechanism and mechanical characteristics of cementitious mineral analogues from first principles and reactive force field molecular dynamics, Phys. Chem. Chem. Phys. 20 (2018) 13920–13933.
[43] D. Hou, J. Yu, Z. Jin, A. Hanif, Molecular dynamics study on calcium silicate hydrate subjected to tension loading and water attack: Structural evolution, dynamics degradation and reactivity mechanism, Phys. Chem. Chem. Phys. 20 (2018) 11130–11144. https://doi.org/10.1039/c7cp08634b.
[44] Y. Zhou, D. Hou, G. Geng, P. Feng, J. Yu, J. Jiang, Insights into the interfacial strengthening mechanisms of calcium-silicate-hydrate/polymer nanocomposites, Phys. Chem. Chem. Phys. 20 (2018) 8247–8266.
[45] Y. Zhou, C.A. Orozco, E. Duque-Redondo, H. Manzano, G. Geng, P. Feng, P.J.M. Monteiro, C. Miao, Modification of poly (ethylene glycol) on the microstructure and mechanical properties of calcium silicate hydrates, Cem. Concr. Res. 115 (2019) 20–30.
[46] J. Yang, D. Hou, Q. Ding, Structure, dynamics, and mechanical properties of cross-linked calcium aluminosilicate hydrate: A molecular dynamics study, ACS Sustain. Chem. Eng. 6 (2018) 9403–9417.
[47] D. Hou, J. Yu, P. Wang, Molecular dynamics modeling of the structure, dynamics, energetics and mechanical properties of cement-polymer nanocomposite, Compos. Part B Eng. 162 (2019) 433–444.
[48] Y. Zhang, X. Lu, D. Song, S. Liu, The adsorption behavior of a single and multi- water molecules on tricalcium silicate (111) surface from DFT calculations, J. Am. Ceram. Soc. 102 (2019) 2075–2083.
[49] H. Manzano, E. Durgun, I. López-Arbeloa, J.C. Grossman, Insight on tricalcium silicate hydration and dissolution mechanism from molecular simulations, ACS Appl. Mater. Interfaces. 7 (2015) 14726–14733.
[50] Q. Wang, H. Manzano, Y. Guo, I. Lopez-Arbeloa, X. Shen, Hydration mechanism of reactive and passive dicalcium silicate polymorphs from molecular simulations, J. Phys. Chem. C. 119 (2015) 19869–19875.
[51] H. Manzano, R.J.M. Pellenq, F.-J. Ulm, M.J. Buehler, A.C.T. Van Duin, Hydration of calcium oxide surface predicted by reactive force field molecular dynamics, Langmuir. 28 (2012) 4187–4197.
[52] H. Kono, T. Erata, M. Takai, Complete assignment of the CP/MAS 13C NMR spectrum of cellulose IIII, Macromolecules. 36 (2003) 3589–3592.
[53] H. Kono, S. Yunoki, T. Shikano, M. Fujiwara, T. Erata, M. Takai, CP/MAS 13C NMR study of cellulose and cellulose derivatives. 1. Complete assignment of the CP/MAS 13C NMR spectrum of the native cellulose, J. Am. Chem. Soc. 124 (2002) 7506–7511.

[54] T. Bucko, D. Tunega, J.G. Ángyán, J. Hafner, Ab initio study of structure and interconversion of native cellulose phases, J. Phys. Chem. A. 115 (2011) 10097–10105.
[55] Y. Li, M. Lin, J.W. Davenport, Ab initio studies of cellulose I: crystal structure, intermolecular forces, and interactions with water, J. Phys. Chem. C. 115 (2011) 11533–11539.
[56] K. Saritas, C. Ataca, J.C. Grossman, Predicting electronic structure in tricalcium silicate phases with impurities using first-principles, J. Phys. Chem. C. 119 (2015) 5074–5079.
[57] E. Durgun, H. Manzano, R.J.M. Pellenq, J.C. Grossman, Understanding and controlling the reactivity of the calcium silicate phases from first principles, Chem. Mater. 24 (2012) 1262–1267.
[58] R.G. Parr, W. Yang, Density functional approach to the frontier-electron theory of chemical reactivity, J. Am. Chem. Soc. 106 (1984) 4049–4050.
[59] H. Manzano, E. Durgun, M.J. Abdolhosseine Qomi, F.-J. Ulm, R.J.M. Pellenq, J.C. Grossman, Impact of chemical impurities on the crystalline cement clinker phases determined by atomistic simulations, Cryst. Growth Des. 11 (2011) 2964–2972.
[60] H. Manzano, J.S. Dolado, A. Ayuela, Structural, mechanical, and reactivity properties of tricalcium aluminate using first- principles calculations, J. Am. Ceram. Soc. 92 (2009) 897–902.
[61] Q. Wang, X. Gu, H. Zhou, X. Chen, X. Shen, Cation substitution induced reactivity variation on the tricalcium silicate polymorphs determined from first-principles calculations, Constr. Build. Mater. 216 (2019) 239–248.
[62] Q. Wang, F. Li, X. Shen, W. Shi, X. Li, Y. Guo, S. Xiong, Q. Zhu, Relation between reactivity and electronic structure for α′ L-, β-and γ-dicalcium silicate: A first-principles study, Cem. Concr. Res. 57 (2014) 28–32.
[63] C.M. Lee, J.D. Kubicki, B. Fan, L. Zhong, M.C. Jarvis, S.H. Kim, Hydrogen-bonding network and OH stretch vibration of cellulose: comparison of computational modeling with polarized IR and SFG spectra, J. Phys. Chem. B. 119 (2015) 15138–15149.
[64] X. Qian, S.-Y. Ding, M.R. Nimlos, D.K. Johnson, M.E. Himmel, Atomic and electronic structures of molecular crystalline cellulose Iβ: A first-principles investigation, Macromolecules. 38 (2005) 10580–10589.
[65] J. Huang, B. Wang, Y. Yu, L. Valenzano, M. Bauchy, G. Sant, Electronic origin of doping-induced enhancements of reactivity: case study of tricalcium silicate, J. Phys. Chem. C. 119 (2015) 25991–25999.
[66] J. Claverie, F. Bernard, J.M.M. Cordeiro, S. Kamali-Bernard, Water's behaviour on Ca-rich tricalcium silicate surfaces for various degrees of hydration: A molecular dynamics investigation, J. Phys. Chem. Solids. 132 (2019) 48–55.
[67] J. Yang, W. Zhang, D. Hou, G. Zhang, Q. Ding, Structure, dynamics and mechanical properties evolution of calcium silicate hydrate induced by dehydration and dehydroxylation, Constr. Build. Mater. 291 (2021) 123327.
[68] J. Sun, W. Zhang, J. Zhang, D. Hou, Molecular dynamics study the structure, bonding, dynamic and mechanical properties of calcium silicate hydrate with ultra-confined water: Effects of nanopore size, Constr. Build. Mater. 280 (2021) 122477.
[69] F. Bellmann, D. Damidot, B. Möser, J. Skibsted, Improved evidence for the existence of an intermediate phase during hydration of tricalcium silicate, Cem. Concr. Res. 40 (2010) 875–884.
[70] S.A. Rodger, G.W. Groves, N.J. Clayden, C.M. DOBSON, Hydration of tricalcium silicate

followed by 29Si NMR with cross- polarization, J. Am. Ceram. Soc. 71 (1988) 91–96.
[71] J.W. Bullard, A determination of hydration mechanisms for tricalcium silicate using a kinetic cellular automaton model, J. Am. Ceram. Soc. 91 (2008) 2088–2097.
[72] T. Sowoidnich, F. Bellmann, D. Damidot, H. Ludwig, New insights into tricalcium silicate hydration in paste, J. Am. Ceram. Soc. 102 (2019) 2965–2976.
[73] B.A. Fleming, D.A. Crerar, Silicic acid ionization and calculation of silica solubility at elevated temperature and pH application to geothermal fluid processing and reinjection, Geothermics. 11 (1982) 15–29.
[74] J.W. Bullard, J. Hagedorn, M.T. Ley, Q. Hu, W. Griffin, J.E. Terrill, A critical comparison of 3D experiments and simulations of tricalcium silicate hydration, J. Am. Ceram. Soc. 101 (2018) 1453–1470.
[75] E. Gartner, I. Maruyama, J. Chen, A new model for the CSH phase formed during the hydration of Portland cements, Cem. Concr. Res. 97 (2017) 95–106.
[76] L. Zhang, X. Cheng, D. Hou, S. Guo, Hydration for the Alite mineral: Morphology evolution, reaction mechanism and the compositional influences, Constr. Build. Mater. 155 (2017) 413–426.
[77] J.S. Dolado, M. Griebel, J. Hamaekers, F. Heber, The nano-branched structure of cementitious calcium–silicate–hydrate gel, J. Mater. Chem. 21 (2011) 4445–4449.
[78] I. Pane, W. Hansen, Investigation of blended cement hydration by isothermal calorimetry and thermal analysis, Cem. Concr. Res. 35 (2005) 1155–1164.
[79] H. Hasan, B. Huang, M. Saafi, J. Sun, Y. Chi, E. Whale, D. Hepworth, J. Ye, Novel engineered high performance sugar beetroot 2D nanoplatelet-cementitious composites, Constr. Build. Mater. 202 (2019) 546–562.